MAGNETIC TURBULENCE VERSUS SAFETY FACTOR IN THE TOKAPOLE II TOKAMAK

by

DALE EDWARD GRAESSLE

A thesis submitted in partial fulfillment of the
requirements for the degree of

Doctor of Philosophy
(Physics)

at the

UNIVERSITY OF WISCONSIN - MADISON

1989

Abstract

MAGNETIC TURBULENCE VERSUS SAFETY FACTOR IN THE TOKAPOLE II TOKAMAK

Dale Edward Graessle

Under the supervision of Professor Richard N. Dexter

Low-frequency ($\omega \ll \omega_{ci}$) radial magnetic turbulence has been measured over the full minor radius ($r = 0 - 18$ cm) for discharges in Tokapole II. It has also been scaled over the range of edge safety factor $0.6 \leq q_a \leq 5.0$. It was found that q_a served as a control parameter for both the magnetic fluctuation amplitude and the global confinement time. As q_a is reduced from 5 to 0.6 the turbulence level increases by a factor of fifty while the confinement time decreases by more than a factor of ten. Due to the lack of profile diagnostics, no detailed study of confinement could be done. The turbulent amplitude 1 cm inside the separatrix is nearly large enough for $q_a \leq 1$ to account for the global confinement by means of collisionless stochastic magnetic transport. Frequency spectra have been obtained reliably from 10 to 400 kHz. For all q_a most of the fluctuation power appears below 100 kHz. This low-frequency structure changes as the safety factor is varied. Although the spectra do not always have clearly-defined peaks in this range of f, radial coherence lengths at these frequencies are very long, indicating global modes with a broadband structure. For $f \geq 100$ kHz, the spectra become featureless, with a power-law frequency decay. For $q_a \leq 3$, the spectra decay as $f^{-1.4}$

in all cases. For higher q_a, a new power law decay of $f^{-2.3}$ appears. Radial, poloidal, and parallel correlation analysis has been done for the full range of q_a, but with a less detailed scan than was included in the amplitude studies. The parallel correlation length is estimated to be 150 ± 50 cm. Radial and poloidal coherence lengths are of the order of the machine dimensions for frequencies below 100 kHz for all q_a. For $f \geq 100$ kHz, radial coherence lengths are $.5 - 2.5$ cm for $q_a \leq 3$. Poloidal coherence lengths are independent of minor radius, and smaller for low q, indicating low q discharges have broader m-spectra. This might explain the increase in fluctuation amplitudes as q_a decreases. It is suggested that the turbulence for all discharges with $q_a \leq 3$ is due to the same underlying cause or set of causes, and that the differences result from geometric effects associated with the variation in q_a.

This work supported by U.S.D.O.E.

Acknowledgements

I must certainly thank my advisor, Dr. Richard N. Dexter, for his very patient and motivating support of this research. His suggestions and general positive attitude about my findings were essential in bringing the work to some degree of completion. I also greatly appreciate his prompt, incisive reviews of the manuscript, without which this paper would be of significantly lesser quality.

Thanks are due also to Dr. Stuart C. Prager, who has contributed much to my understanding of the possible implications of the data, and who, along with Dr. Dexter, was largely responsible for the text of the Physical Review Letter recently published about my work. Both men were very supportive and encouraging during the long years of effort consumed in collecting, analyzing, and interpreting this data. Their help will not soon be forgotten.

Another man whose help must not go unmentioned is Mr. Tom Lovell. His efforts in keeping a maintenance-intensive machine in operation are the reason I am not still in the lab trying to take the data. His advice concerning hardware and computer techniques were indispensable to my success as a graduate student. Also, his fine wit and endearing stories were a much-needed relief from the frustrations endemic to small tokamak research.

I am grateful to Jon Kranz for his help and suggestions in obtaining hardware necessary for my experiment. I would also like to

thank the plasma physics hourly staff, many of whom have come and gone since the start of my thesis work. I wish them all the best in their new careers.

I would also like to acknowledge the contribution of Saeed Assadi to this work. His finely-built 24-coil triaxial array provided the polarization measurements presented herein. Unfortunately, this very carefully-made probe was damaged in the experiment. An apology is due, but it is hopelessly insufficient for absolution.

On the personal level, I would like to thank my parents, Donald and Mary Graessle, who have been very helpful to me in attaining this goal that I have pursued since an early age. Their understanding and reassurance along the way is greatly appreciated.

Finally I must also acknowledge my wife, Carol Kinoshita. She is perhaps the most wonderful helper, despite having her own fine career, that anyone could ever have.

Table of Contents

CHAPTER 1:

Introduction

This thesis describes the results of low-frequency, broadband magnetic turbulence measurements made on the Tokapole II tokamak at the University of Wisconsin. They will be described in detail, in the hope that these findings will be of some interest and utility toward the success of the magnetic fusion effort.

Not the least important difficulty in obtaining fusion power in a tokamak[1] is that of identifying the plasma transport mechanisms therein, and determining the level of tranport associated with each mechanism. It is widely published that tokamaks exhibit levels of particle and thermal transport from ten to one hundred times that predicted by neoclassical diffusion.[2,3,4] Transport from large-scale (macroscopic) instabilities in these devices can be minimized via proper adjustment of machine parameters, and is not sufficient to account for the measured anomalous losses. It is also well known that small-scale turbulence in the plasma density, space potential, temperature, and magnetic field is omnipresent in these machines, and that it can, in theory, produce large transport levels across closed magnetic flux surfaces.

Theorists have constructed a number of microinstability models that cause turbulent spectra, as well as several mechanisms whereby

turbulent transport may be calculated. However, not only is the theory incomplete, but a lack of experimental turbulence measurements prevents the immediate evaluation of the relative importance of the developed models. It is not known, for example, which, if any, turbulent quantity induces the most important loss mechanism. Measurements of magnetic fluctuations in the interior of tokamaks are quite conspicuously absent. This results from the lack of non-intrusive diagnostics to measure $\tilde{B}$ in the tokamak interior. Non-intrusive diagnostics have been developed and used to measure density[5,6,7] and potential[7] fluctuations, albeit with some loss of spatial resolution. Fluctuations in magnetic field and temperature, however, are best measured with small local sensors. This requires using a cooler, lower density plasma which will permit insertion of material probes. In this vein, $\tilde{B}$ measurements have been made in Tokapole II, and are reported here.

In the course of the experiments, it was found that the RMS amplitude of the magnetic fluctuations ($\tilde{B}_r$) was a monotonically decreasing function of the edge safety factor q_a over the range $0.6 \leq q_a \leq 5$. The safety factor was thus a control parameter for the turbulent amplitude, and all measurements were scaled with q_a. Despite the amplitude variation, standard spectral analysis of the data reveals a commonality to the microturbulence, suggesting that a single underlying cause or set of causes is responsible for the microscopic $\tilde{B}_r$ at all q_a.

The attempt to use this information to clarify transport and test theoretical models has met with a number of presently unresolved difficulties. Experimentally, few of the radial profiles needed to determine the radial transport profile have been made in Tokapole II. Plasma confinement therein is only estimated as a global quantity. Also, the only measurements made with significant alteration of both $\tilde{B}_r$ and confinement were those involving variation in q_a; no other adjustment of parameters was found to vary either parameter in a controlled way without some degradation in the macroscopic stability of the discharges, which thus clouded the results. Hence, no causal relationship between $\tilde{B}_r$ and confinement has been definitively established in this work.

From the theoretical standpoint, no approaches have been developed which involve the safety factor as a determining variable either in turbulence amplitude or in energy confinement. The information reported here, then, will hopefully help provide a suitable ground work for future theoretical study, in the context of either currently developed models or new approaches.

This paper is organized as follows: Chapter 2 gives the theoretical and experimental background for this work, including some discussion of magnetic transport models. The hardware and analysis methods for this experiment are described in Chapter 3. The extensive measurements and calculations are included in Chapter 4, in considerable detail. Chapter 5 provides a list of final results, suggested continuations of the work, and a summary of main points.

REFERENCES

[1]L.A. Artsimovich, Nucl. Fusion **12**, 215 (1972).

[2]*Status of Tokamak Research*, J.M. Rawls, Ed., U.S. DOE, Washington, DC, DOE/ER-0034 (1979).

[3]J. Hugill, Nucl. Fusion **23**, 331 (1983).

[4]P.C. Liewer, Nucl. Fusion **25**, 543 (1985).

[5]C.M. Surko and R.E. Slusher, Phys. Fluids **23**, 2425 (1980).

[6]J. Sheffield, *Plasma Scattering of Electromagnetic Radiation*, Academic Press, New York and London (1975).

[7]K. Saadatmand, R.L. Hickok, and W.C. Jennings, Bull. Am. Phys. Soc. **28**, 1072 (1983).

CHAPTER 2:

Background and Motivation

Tokamak transport for work preceding 1983 was reviewed by Hugill.[1] P.C. Liewer reviewed anomalous transport, fluctuations measurements and turbulence theory preceding 1985.[2] The following discussion is motivated mainly by information given in these two reviews. The measured transport in tokamaks is one to two orders of magnitude higher than neoclassical collisional transport[3] (the largest-known irreducible transport mechanism) predicts. Turbulence in the plasma has been offered as an explanation because it is present in every tokamak, and transport can be theoretically derived from it. But the actual extent of the fluctuation-induced transport in tokamaks is not generally known, nor is it known what causes the turbulence itself. Turbulence is present in several local plasma quantities, and each has different transport effects associated with it. For this paper, only the magnetic fluctuations and their associated transport processes will be presented.

2.1. Transport properties of tokamaks

Many tokamaks have been operated and found to have similar confinement properties. Because it remains impossible to explain tokamak confinement properties from first principles, empirical scaling

relations have been developed and refined from the databases of various tokamak experiments in the hope that such relations would be useful in predicting the results of new tokamaks successfully.[4,5,6] In so doing, a fusion reactor design might eventually be reached. But no device built to date has ever achieved the performance level necessary for a fusion reactor and the transport processes contributing to this failure cannot be readily understood from the empirical scaling.

Some general observations have surfaced in the data:

(1) Both particle and thermal transport are anomalous in tokamaks. The anomalous particle diffusion coefficient (D) is typically estimated at $D \approx (0.1\text{–}0.25)\chi_e$, where χ_e is the anomalous electron thermal diffusivity.[7]

(2) Although there is no a priori reason to believe that small-scale effects are responsible for anomalous transport, several experiments have provided evidence that tokamak thermal transport is a small-scale, diffusive process. In these experiments, the energy flow is describable by a diffusion equation

$$\frac{\partial}{\partial t}\left(\frac{3}{2}\, n_e T_e\right) = \frac{1}{r}\frac{\partial}{\partial r}\left(r K_e \frac{\partial T_e}{\partial r}\right) \qquad (2-1)$$

with thermal conduction coefficient $K_e = n\chi_e$, where χ_e is the thermal diffusivity and n is the electron density.[8,9,10]

(3) Experimenters have found low frequency ($\omega \ll \omega_{ci}$) short-scale-length turbulence (microturbulence) in every tokamak in which they

have attempted to measure it.[2] This includes fluctuations in electron density, space potential, magnetic field, and temperature.

(4) For the low-density, ohmically-heated tokamaks the confinement is thought to be determined by losses from the electrons rather than the ions. This is because the electrons are the main species heated by the ohmic input, and the electron-ion heat exchange occurs at a significantly lower rate than the total energy loss from the system. The assumption here is that electron-ion heat exchange is *not* anomalous. In such machines, the measured confinement is typically 10 to 100 times worse than predicted by classical processes.[11]

(5) For higher-density tokamaks the loss mechanism is more complicated because electron-ion heat exchange increases and ion contributions can become important. Detailed profile information for electron and ion components is then necessary.

(6) The empirical scaling studies have had marginal success in improving tokamak performance, and the development of the tokamak has reached the point where only small improvements in confinement, such as enhancement by a factor of two, could lead to the success of the program.

The study of microturbulence is motivated by observations (2) and (3), and by theoretical predictions of transport due to turbulence (§ 2.2). Turbulence measurements are necessary to determine which microturbulent processes, if any, are important in determining tokamak confinement.

Because the energy is believed to be lost mainly via the electron channel for the low-density, ohmic tokamaks, much work has been done to evaluate mechanisms that can enhance electron diffusion and electron thermal diffusivity. Analysis of power flows in many tokamaks indicates that thermal diffusion transports more energy than particle loss, but fluctuations measurements are necessary to determine if this is actually the case. It turns out that either particle loss or conductive energy loss can result from magnetic fluctuations, as will be discussed next.

2.2. The possible importance of $\tilde{B}$

2.2.1. *Particle and energy transport from* $\tilde{B}_r$

Particle transport may result from fluctuations because of the fluctuating radial velocity of the plasma due to the local fluctuating fields. For the following derivation, adapted from the microturbulence review of Liewer[12], fluctuations of $\omega \ll \omega_{ci}$ are assumed. If $\tilde{v}_r$ is the fluctuating radial velocity of a particle due to fluctuating electric and magnetic fields, it may be expressed

$$\tilde{v}_r = c\,\tilde{E}_p/B - v_{\parallel}\,\tilde{B}_r/B \qquad (2-2)$$

where $\tilde{E}_p$ is the fluctuation in the poloidal electric field, $v_{\parallel}$ is the parallel velocity of the particle, and $\tilde{B}_r$ is the total fluctuation in the radial magnetic field. The particle transport is then calculated as the radial particle flux $\Gamma_r = nV_r$, where V is the fluid velocity and n is the density.

The transport due to turbulence is found by separating the steady-state, or average, values of the quantities n and V_r as follows: $n = \langle n \rangle + \tilde{n}$, where $\langle\ \rangle$ denotes a time-averaged value such that $\langle \tilde{n} \rangle = 0$. Then $nV_r = \langle(\langle n \rangle + \tilde{n})(\langle V_r \rangle + \tilde{V}_r)\rangle = \langle n \rangle\langle V_r \rangle + \langle \tilde{n}\tilde{V}_r \rangle$, and the fluctuating component of this is

$$\Gamma_r^t = \langle \tilde{n}\tilde{V}_r \rangle \approx \int_{-\infty}^{\infty} d\omega\, \tilde{n}^*(\omega)\, \tilde{V}_r(\omega) \qquad (2-3)$$

where the superscript "t" has been used to indicate that the particle transport is due to the turbulence. Applying this to Eq. (2–1) yields

$$\Gamma_r^t = \frac{c\langle \tilde{E}_p \tilde{n} \rangle}{B} - \frac{\langle \tilde{j}_{\parallel} \tilde{B}_r \rangle}{eB} \qquad (2-4)$$

where $\tilde{j}_{\parallel}$ is the fluctuating parallel electron current. It is then necessary to evaluate cross correlations in order to arrive at the turbulent transport from this particular model. (Other effects may be involved, and the radial transport due to this mechanism could actually be negative.)

Calculating thermal transport is more involved, partly because energy can be transported by both particle loss (convection) and enhanced thermal diffusion (conduction). A relatively complicated fluid analysis shows that the total heat flux due to low-frequency, electrostatic ($\tilde{B} = 0$) turbulence (convective and conductive) depends on the correlation between the radial fluid velocity fluctuations

($\tilde{V}_r = c\tilde{E}_p/B$) and plasma pressure fluctuations. For isotropic pressure fluctuations $\tilde{p}$, the total of the radial convective and conductive heat fluxes is [13]

$$Q_r^t = \frac{5c}{2B}\langle \tilde{E}_p \tilde{p} \rangle. \qquad (2-5)$$

Mannheimer and Cook extended this result to include the effects of magnetic turbulence.[14] The expression they derived for the total heat flux due to turbulence in pressure, magnetic field, and electric field is

$$Q_r^t = \frac{c}{B}\int d^3v \left\{ \frac{mv^2}{2}\left\langle \tilde{E}_p \tilde{f}_e \right\rangle + \left\langle mv_p \mathbf{v} \cdot \tilde{\mathbf{E}} \tilde{f}_e \right\rangle + \frac{mv^2}{2}\frac{v_{\parallel}}{c}\left\langle \tilde{B}_r \tilde{f}_e \right\rangle \right\} \qquad (2-6)$$

and so the inclusion of magnetic turbulence $\tilde{B}_r$ enhances the transport. As in Eq. (2–2) above, cross-correlations are important in evaluating the transport. Coupling their result with the drift-wave analysis of Callen,[15] they concluded that the magnetic turbulence contribution can be at least as high as that from electrostatic turbulence in a tokamak.

Radial magnetic fluctuations can have an additional, and perhaps more important, effect on electron thermal diffusion because of the large classical heat conductivity parallel to the field in a tokamak. The radial fluctuations cause some portion of this conductivity to be redirected radially. Using a fluid approach, one can derive this transport starting from the classical conductive heat flux,[16]

$$q_r = n\left(-\chi_{\parallel}\nabla_{\parallel}T - \chi_{\perp}\nabla_{\perp}T\right) \qquad (2-7)$$

where $\chi_{||}$ and $\chi_{\perp}$ are the classical heat conductivities parallel and perpendicular to the field. In order to involve the radial magnetic fluctuations, let $\hat{b}$ be a unit vector in the (instantaneous) local direction of the field. With turbulence present, $\hat{b} = \langle\hat{b}\rangle + \hat{r}(\tilde{B}_r/B)$, where $\langle\hat{b}\rangle$ is in the direction of the equilibrium field. Applying this to Eq. (2 – 7), the result for the radial conduction due to magnetic turbulence is

$$q_r = n\left(-\chi_{\parallel}\left\langle\left|\frac{\tilde{B}_r}{B}\right|^2\right\rangle\frac{dT}{dr} - \chi_{\parallel}\left\langle\left|\frac{\tilde{B}_r}{B}\right|\frac{d\tilde{T}}{dr}\right\rangle\right) \qquad (2-8)$$

The value of $\chi_{||}$ is so large that only a relatively small turbulence level ($\tilde{B}_r/B \approx 10^{-4}$) is needed to produce anomalous χ_e values comparable to experimental estimates. This fluid approach was investigated by Kadomtsev and Pogutse,[17] who made the assumption that the field lines were actually braided, and also by Haas, Thyagaraja, and Cook,[18] who made no assumptions as to field topology.

Electron thermal transport enhancement in a braided magnetic field may also be investigated using a test particle approach rather than a fluid model. This has been pursued in great detail by a number of researchers,[19 – 22] and is summarized by Krommes, Oberman, and Kleva.[23] Usually called electron thermal transport from stochastic magnetic fields, this development assumes the radial magnetic fluctuations are large enough that the resonant island structure that results on a particular flux surface overlaps the neighboring island structures. With large enough perturbations, the field lines wander

randomly throughout the entire radial region of the overlapping islands, and the result is limited destruction of the flux surfaces, and the energy confinement is short-circuited to the outer edge of the affected region. This is thought of as the most influential effect of magnetic turbulence on confinement, and when one evaluates magnetic turbulent transport, one ordinarily uses a formula for the correct collisionality regime as given in Ref. [23].

Stochastic magnetic transport models do not derive the turbulent magnetic spectrum self-consistently, but instead assume a turbulent spectrum, and in so doing they do not consider the effects of the particle or energy transport on the fluctuations. Since a complete theory must not only predict transport, but also derive the instability or set of instabilities, and produce the turbulent spectra therefrom, sources of magnetic turbulence must be investigated. Many instabilities can influence the magnetic field, and many possible models have been developed. It remains quite undetermined, however, which is actually the most important in the tokamak.

2.2.2. *Sources of magnetic turbulence*

Possible causes of magnetic turbulence in tokamaks include drift waves, microscopic MHD modes, and nonlinear interaction of MHD modes. Due to the experimental nature of this paper, and the availability of the review by Liewer,[2] only a brief description of some examples is appropriate here, with the inclusion of references if a more detailed description is desired.

Drift-wave turbulence (reviewed by Horton[24]) is ordinarily derived as an electrostatic instability, but it has a small magnetic component that becomes important as the plasma β increases. Callen[15] pressed the issue of drift-wave magnetic turbulence, which is caused by the fluctuating current resulting from the difference between the wave-induced perpendicular ion and electron drifts, and found that it could be a more important cause of thermal transport in a tokamak than the electrostatic drift-wave turbulence. Waltz[25] used a fluid model to simulate electromagnetic drift waves numerically, and found the scaling between magnetic and density fluctuations to be

$$\tilde{B}_\perp/B \approx (\beta/2)q\,\tilde{n}/n \qquad (2-9)$$

so that at modest β magnetic transport dominates. The issue is by no means resolved, as more work is needed to complete the development of electromagnetic drift-wave turbulence theory.

A number of MHD microturbulence (high poloidal mode number m) models are extensions of the large-scale resistive MHD instabilities. Most ideal MHD modes do not have microscopic analogs because the single-fluid model used to derive them breaks down for microturbulence, due to the increased importance of finite Larmor radius, electron compressibility, and resonant or trapped particles.[26] All MHD modes can be derived from two-fluid or kinetic equations, to determine whether these small-scale effects are important. Usually they are more important for higher m.

If a two-fluid or kinetic model is used, finite ion gyroradius, resonant and trapped particles, separate density and temperature gradients, and electron motion along the magnetic field lines may be included. These can alter the overall stability of the MHD modes depending on the m, resulting in new instabilities from new sources of free energy. However, the low-frequency modes ($\omega \ll \omega_{ci}$) are still considered to be the most important in tokamaks. Some microscopic analogs of MHD modes that can be so derived are the micro-tearing or drift-tearing mode, the high-m resistive ballooning mode, and the kinetic ballooning mode (ideal MHD). Microtearing modes[27] are driven by the expansion free energy rather than the magnetic energy which drives the macroscopic tearing modes. They may be driven by the electron temperature gradient[28] or by trapped particles.[29] Micro-tearing modes are expected to be unstable in many tokamaks.[28] Microscopic, high-m resistive ballooning modes are derived from the resistive MHD ballooning modes when diamagnetic effects are included.[30-32] The kinetic ballooning modes[30-32] may be unstable for $\beta > a/q^2R$, as for the ideal MHD ballooning mode.

Another model likely to explain some microinstabilities in tokamaks is resistivity-gradient-driven-turbulence.[33-35] This is also known as the rippling mode or current-convective mode. The parallel current and resistivity gradient are included in a resistive MHD derivation to obtain this mode. It is expected to become important in collisional plasmas with steep temperature gradients. Hahm *et al*[35]

have derived the magnetic fluctuations due to this primarily electrostatic mode, and found $(\tilde{B}_r/B_t)$ to be independent of temperature, but sensitive to the impurity profile, the temperature gradient and the shear length.

2.3. Other magnetic turbulence measurements

Magnetic fluctuations are found in every tokamak. In general, they are very similar for every tokamak in which they have been measured. It is reasonable, then, to assume that magnetic turbulence data taken from any tokamak will prove useful in understanding the issue of turbulence in confined plasmas, regardless of the parameters of the tokamak in question. It is under this assumption that the information related in this thesis was pursued. The evidence justifying this assumption is related in the following subsections about measurements in other tokamaks.

2.3.1. *Macrotor*

Perhaps the most frequently referenced work on magnetic turbulence was done by Zweben and Taylor in the Macrotor tokamak at UCLA.[36,37] The device parameters were: $T_e \approx 100$ eV, $a = .45$ m, $R = .9$ m, $B_t \leq 3$ kG, $\langle n_e \rangle \approx 10^{12}$-$10^{13}/\text{cm}^3$, $I_p \approx 50$ kA, and $\beta_t \approx 10^{-3}$ at $r = .67a$. The sensors were placed into the plasma as far as $r/a = .6$. Large-scale oscillations associated with MHD activity were found at low frequencies. The turbulent amplitude for frequencies $f \geq 30$ kHz was found to be 10^{-4}–10^{-5} B_t for both radial and poloidal field fluctuations. Toroidal field

fluctuations were no more than one-tenth of the radial field turbulence amplitude. Radial profiles of $\tilde{B}_r$ were found to increase with decreasing radius, resembling the equilibrium ion saturation current (J_{sat}) profiles. Further, the turbulence amplitude increased with increasing plasma current and with decreasing q_a, but was independent of equilibrium density. Coherence lengths were less than 5cm in the radial and poloidal directions for $f \sim 100$ kHz, but coherence was significant for probes separated 4cm. Toroidally separated sensors revealed much longer toroidal correlation lengths than radial.[37]

In another experiment, simultaneous magnetic and electrostatic turbulence measurements were made in Macrotor.[38] Though the magnetic and electrostatic turbulent spectra were similar, cross-correlations of density or potential fluctuations and magnetic fluctuations measured at nearly the same spatial location were small enough to be insignificant.

2.3.2. *Caltech*

Hedemann made an extensive series of magnetic turbulence measurements in the Caltech Research Tokamak ($R = .46$m, $a = .15$m, $B_t \leq 5$T, $I_p \leq 30$kA, $T_e \sim 100$–200eV).[38] Probes were placed directly into the plasma as far in as $r = (2/3)a$. Radial, toroidal, and poloidal field fluctuations were measured up to 2 MHz throughout the various stages of the discharge. The turbulence amplitude for the full frequency range is $\tilde{B}_r \approx \tilde{B}_p \approx 10^{-3}B_t$, and the toroidal field fluctuations are smaller by a factor of five, for the portion of the discharge with constant density. The

fluctuations below 100 kHz were large-scale coherent MHD effects. About ten percent of the total amplitude was short-scale turbulence at $f \geq 100$ kHz. The low-frequency and high-frequency components appeared to be independent phenomena. The radial profiles of $\tilde{B}_r$ increased with decreasing minor radius, by a factor of 4.6 from $r = (14/15)a$ to $r = (2/3)a$. (The J_{sat} profile was unavailable for comparison.) The microturbulence levels were found to be too small by about a factor of six to account for the global confinement. In contrast to the Macrotor results, $\tilde{B}_r$ was found to be independent of I_p and q_a as it was varied over $3 \leq q_a \leq 6$, but was found to increase with density. Microturbulent ($f \geq 100$ kHz) poloidal coherence lengths were about 1cm, and radial coherence lengths were somewhat longer.

2.3.3. ISX-B

Measurements of $\tilde{B}_p$ for $f \leq 250$ kHz behind the edge limiter were made in the ISX-B tokamak at the Oak Ridge National Laboratory.[39] MHD activity dominated the low-frequency spectrum, while the high-frequency spectrum was broadband and uniformly decaying with f. The broadband tail and MHD activity were independent. Correlation lengths were found to be about 5cm. Similar broadband turbulence was found using electrostatic probes, but the signals were uncorrelated to $\tilde{B}_p$, similar to the Macrotor result.[38]

The fluctuations were measured in both ohmic and beam-heated discharges, and $\tilde{B}_p$ was found to increase with increasing beam power and increasing β_p. The increase in β_p was correlated with a systematic

reduction in global confinement time. For $\beta_p \geq 1$, the turbulence and confinement results were modeled quite convincingly as resistive-MHD ballooning modes.[40] The causal relation between turbulence and transport could not be firmly established because the turbulence measurements were not made at the radius for which the theoretical instability and turbulent transport calculations were made.

2.3.4. PRETEXT

Levinson *et al* measured magnetic turbulence in the edge (1 cm inside the limiter) of the PRETEXT tokamak (R = 53.3 cm, a = 14 cm, $B_t = 0.75$ T, $I_p \approx 25$ kA, $V_L \approx 2$ volts, $q_{limiter} \approx 6.7$, $\langle n \rangle \approx 10^{13}$ cm^{-3}, $T_e \approx 100$ eV) at the University of Texas at Austin,[40] using a probe with four radial coils in a square array. The frequency range studied was 5 – 250 kHz. There it was found that $\tilde{B}_r/B \sim 10^{-5}$. The main thrust of their work was to calculate fixed-pair wavenumber spectra[41] of $\tilde{B}_r$ in the radial and poloidal directions. The spectra were dominated by coherent MHD activity at low frequency. The turbulence propagates in the electron diamagnetic drift direction for frequencies $f < 100$ kHz. For higher frequencies, the k_θ-spectra are very broad, with the turbulence propagating mainly in the ion diamagnetic drift direction. These magnetic wavenumber spectra are entirely different from those of the electrostatic turbulence in PRETEXT, reported previously.[42] The k_r-spectra were very narrow, due to the dominance of the MHD fluctuations, and adaptive filtering was used successfully to remove the

MHD from the data, in order that microturbulence at low frequencies might be investigated.

2.3.5. TCA

A very fine set of experiments was done in the TCA tokamak at Lausanne (Switzerland). Dupperex and others[43] reported measurements over the $f \leq 1$MHz range, finding $\tilde{B}_r/B \approx 10^{-5}$ for probes in the shadow of the limiters. Fluctuations increased with decreasing density and with decreasing τ_E. Mirnov oscillations were present at ~10 kHz, while for $f \geq 50$kHz the spectrum was broadband and featureless, decaying in amplitude with frequency according to f^{-2}. Also, $\tilde{B}_p \sim \tilde{B}_r$, and $\tilde{B}_t \sim (1/3)\tilde{B}_r$. Later, Hollenstein and others[44] reported measurements from an edge poloidal Mirnov array and a separate triaxial probe for frequencies below 500kHz. The correlation between radial and poloidal magnetic turbulence at the same location was small for $f \geq 100$ kHz, indicating that the sources of $\tilde{B}_p$ and $\tilde{B}_r$ are distinct. Poloidal coherence lengths of $\tilde{B}_p$ were found to be of the order of 10cm, even for high frequencies. However, the coherence was also strong for probes separated by any distance along a contour of q = 2. Radial amplitude decay measurements indicated that $6 \leq m_{mean} \leq 8$ from poloidal fluctuations, and this result was similar to that found from phase measurements. Density fluctuations measured by Langmuir probes behind the limiter were found to be unrelated to the magnetic fluctuations, in both scaling and spectra. Continuing experiments with

new arrays have shown that the maximum coherence occurs for displacements along the magnetic field lines.[45]

2.3.6. Doublet III

An external poloidal Mirnov array was used to measure poloidal magnetic fluctuations in neutral-beam-heated discharges outside the divertor separatrix in the Doublet III tokamak at General Atomic, Inc.[46] The discharges studied were primarily those referred to as "marginally diverted", which underwent repetitive transitions between the *L* mode and *H* mode. The fluctuation level decreased abruptly at the onset of the *H* phase, and then abruptly increased when the *L* phase returned. Radial amplitude decay measurements from the Mirnov array indicated a lower bound for the mean poloidal mode number of $m \approx 8$. From this decay measurement, the turbulence amplitude at the plasma surface was estimated at $\tilde{B}_p/B_t \approx 2 \times 10^{-4}$. The authors suggest[46] that the turbulence resulted from microtearing modes, and that this turbulence was quite possibly responsible for the *L*-mode scaling.

2.3.7. Other tokamaks

Some of the older magnetic turbulence studies not reported here were done on PLT[47] and JIPP T-II.[48] Recent magnetic turbulence work (published since the Liewer review) has been conducted on other machines of various sizes, including TORTUR,[49] TEXT,[50,51] TFTR,[52] and JET.[53] It is clear that many machines have become involved in magnetic

fluctuations since the theoretical studies suggested that indicated magnetic fluctuations might be important.

REFERENCES

[1]J. Hugill, Nucl. Fusion **23**, 331 (1983).

[2]P.C. Liewer, Nucl. Fusion **25**, 543 (1985).

[3]F.L. Hinton and R.D. Hazeltine, Rev. Mod. Phys. **48**, 239 (1976).

[4]M. Gaudreau, A. Gondhalekar, M.H. Hughes, D. Overskei, D.S. Papper, R.R. Parker, S.M. Wolfe, E. Apgar, H.I. Helava, I.H. Hutchinson, E.S. Marmar, K. Molvig, Phys. Rev. Lett. **39**, 1266 (1977).

[5]W. Pfeiffer and R.E. Waltz, Nucl. Fusion **19**, 51 (1979).

[6]R.J. Goldston, in *Invited papers of the eleventh European conference, Aachen, 1983*, Plasma Phys. Contr. Fusion **26**(1A), 87 (1984).

[7]P.C. Liewer, p.547.

[8]J.D. Callen and G.L. Jahns, Phys. Rev. Lett. 38, 491 (1977); M. Soler and J.D. Callen, Nucl. Fusion **19**, 703 (1979).

[9]J.D. Bell, J.L. Dunlap, V.K. Paré, J.D. Callen, H.C. Howe, E.A. Lazarus, M. Murakami, and C.E. Thomas, Nucl. Fusion **24**, 997 (1984).

[10]E.D. Fredrickson, J.D. Callen, K. McGuire, J.D. Bell, R.J. Colchin, P.C. Efthimion, K.W. Hill, R. Izzo, D.R. Mikkelsen, D.A. Monticello, V. Paré, G. Taylor, and M. Zarnstorff, Nucl. Fusion **26**, 849 (1986).

[11]P.C. Liewer, p. 545.

[12]P.C. Liewer, pp. 551–552.

[13]B.B. Kadomtsev and O.P. Pogutse, in *Reviews of Plasma Physics*, edited by M.A. Leontovich, Consultants Bureau, New York, **5**, 249 (1970).

[14]W.M. Manheimer and I. Cook, Comments Plasma Phys. **5**(1), 9 (1979).

[15]J.D. Callen, Phys. Rev. Lett. 39(24), 1540 (1977).

[16]S.I. Braginskii, in Rewiews of Plasma Physics, ed. M.A. Leontovich, Consultants Bureau, New York, **1**, 205 (1965).

[17]B.B. Kadomtsev and O.P. Pogutse, in *Proceedings of the Seventh International Conference on Plasma Physics and Controlled Nuclear Fusion Research,* Budapest,1978 (IAEA, Vienna, 1979), **1**, 649.

[18]F.A. Haas, A. Thyagaraja, and I. Cook, Plasma Phys. **23**, 1027 (1983); A. Thyagaraja, F.A. Haas, I. Cook, Nucl. Fusion **20**, 611 (1980).

[19]T.H. Stix, Nucl. Fusion **18**, 353 (1978).

[20]A.B. Rechester and M.N. Rosenbluth, Phys. Rev. Lett. **40**, 38 (1978).

[21]H.E. Mynick and J.A. Krommes, Phys. Rev. Lett. **43**, 1506 (1979).

[22]H.E. Mynick and J.A. Krommes, Phys. Fluids **23**, 1229 (1980).

[23]J.A. Krommes, C. Oberman, and R.G. Kleva, J. Plasma Phys. **30**, 11 (1983).

[24]W. Horton, in *Basic Plasma Physics II*, edited by A.A. Galeev and R.N. Sudan, North Holland, 383 (1985).

[25]R.E. Waltz, Phys. Fluids **28**, 577 (1985).

[26]P.C. Liewer, p. 581.

[27]J.F. Drake, N.T. Gladd, C.S. Liu, and C.L. Chang, Phys. Rev. Lett. **44**, 994 (1980).

[28]N.T. Gladd, J.F. Drake, C.L. Chang, and C.S. Liu, Phys. Fluids **23**, 1182 (1980).

[29]L. Chen, P.H. Rutherford, W.M. Tang, Phys. Rev. Lett. **39**, 460 (1977).

[30]K. Tsang, Phys. Fluids **24**, 2017 (1981).

[31]J.W. Van Dam, Ph.D. Thesis, Kinetic Theory of Ballooning Instabilities, UCLA (1979).

[32]A.B. Mikhailovsky, Nucl. Fusion **13**, 259 (1973).

[33]B.A. Carreras, P.W. Gaffney, and H.R. Hicks, Phys. Fluids 25, 1231 (1982).

[34]L. Garcia, P.H. Diamond, B.A. Carreras, and J.D. Callen, Phys. Fluids **28**, 2147 (1985).

[35]T.S. Hahm, P.H. Diamond, P.W. Terry, L. Garcia, and B.A. Carreras, Phys. Fluids **30**, 1452 (1987).

[36]S.J. Zweben, C.R. Menyuk, R.J. Taylor, Phys. Rev. Lett. **42**(19), 1270 (1979); Errata, ibid., 1720.

[37]S.J. Zweben, R.J. Taylor, Nucl. Fusion **21**(2), 193 (1981).

[38]M.A. Hedemann, Ph.D. Thesis, *Measurements of magnetic fluctuations in the Caltech Research Tokamak,* (1982); R.J. Taylor, P. Lee, N.C. Luhmann, Jr., A. Mase, G.J. Morales, W.A. Peebles, A. Semet, F. Schwirzke, S. Talmadge, S.J. Zweben, M.A. Hedemann, B.S. Levine, and R.W. Gould, in Proceedings of the eighth International Conference on Plasma Physics and Controlled Nuclear Fusion Research, Brussels, 1980, (IAEA, Vienna, 1981) **2**, 61.

[39]B.A. Carreras, Phys. Rev. Lett. **50**, 503 (1983).

[40]S.J. Levinson, B. Rogers, E.J. Powers, R.D. Bengtson, Bull. Am. Phys. Soc. **30**, 1441 (1985).

[41]J.M. Beall, Y.C. Kim, E.J. Powers, J. Appl. Phys., **53**, 3933 (1982).

[42]S.J. Levinson, J.M. Beall, E.J. Powers, R.D. Bengtson, Nucl. Fusion **24**, 527 (1984).

[43]P.A. Duperrex, Ch. Hollenstein, B. Joye, R. Keller, J.B. Lister, F.B. Marcus, J.M. Moret, A. Pochelon, and W. Simm, Physics Letters **106A**, 133 (1984).

[44]Ch. Hollenstein, R. Keller, A. Pochelon, F. Ryter, M.L. Sawley, W. Simm, and H. Weisen, in *Proceedings of the Cargèse Workshop*, 1986, edited by D. Grésillon and M.A. Dubois, (1986); Lausanne internal report LRP 306/86.

[45]F. Ryter, A. Pochelon, and F. Hofmann, in *Proceedings of the 14th European Conference on Controlled Fusion and Plasma Physics, Madrid, 1987*, edited by S. Methfessel (EPS, Petit-Lancy, 1987).

[46]N. Ohyabu, G.L. Jahns, R.D. Stambaugh, and E.J. Strait, Phys. Rev. Lett. **58**, 120 (1987).

[47]C.W. Barnes and J.D. Strachan, Phys. Fluids **26**, 2668 (1983).

[48]S.K. Guharay, K Kawahata, and N. Noda, J. Nucl. Mater. **128-129**, 325 (1984).

[49]H. De Kluiver, C.J. Barth, and A.J. Donné, Plasma Phys. Contr. Fusion **30**, 699 (1988).

[50]K.W. Gentle, Y.J. Kim, Ch.P. Ritz, and T.L. Rhodes, in *Proceedings of the Fourteenth European Conference on Controlled Fusion and Plasma Physics, Madrid, 1987*, edited by S. Methfessel (EPS, Petit-Lancy, 1987).

[51]Y.J. Kim, K.W. Gentle, Ch.P. Ritz, and Terry L. Rhodes, Bull. Am. Phys. Soc. **33**, 2026 (1988).

[52]S.J. Zweben, D. Manos, R.V. Budny, P. Efthimion, E. Fredrickson, H. Greenside, K.W. Hill, S. Hiroe, S. Kilpatrick, K. McGuire, S.S. Medley, H.K. Park, A.T. Ramsey, and J. Wilgen, J. Nucl. Mater. **145-147**, 250 (1987).

[53]M. Malacarne and P.A. Duperrex, Nucl. Fusion **27**, 2113 (1987).

CHAPTER 3:

Experimental Techniques

This chapter provides a basic description of the Tokapole II device, with references to more complete and detailed descriptions published earlier, and a description of those diagnostics and techniques specific to the experiments reported in this thesis.

The main experimental goal was to characterize the magnetic turbulence as a function of the safety factor q_a for the steady-state portion of the discharges only. No attempt is made in this thesis to study start-up and termination effects. The range of frequencies considered is $f \leq 400$ kHz, which is well below the ion gyrofrequency for all of these discharges.

The measurements were made as far into each discharge as the stability and probe conditioning would allow. For several values of q_a, amplitude and radial correlation measurements were made several centimeters within the sawtooth inversion radius, which usually occurs at $r \geq 6$cm for the steady state portion of the shots. To date, we know of no other machines that have reported magnetic turbulence measurements as far inside the plasma as this.

3.1. The Tokapole II tokamak

The Tokapole II tokamak was initially proposed with the intention of providing a small tokamak for research. It was funded to be operated without the use of costly, high-maintenance diagnostics such as radial interferometry arrays or laser scattering devices, which are the ordinary methods by which internal measurements are made, or profiles determined. This means that no profiles have been measured for the internal electron temperature, ion density and temperature, current density, and hence energy confinement. These quantities must be treated globally, and their profiles assumed, fitted to measurements of other quantities, or ignored. Notwithstanding, this thesis will show that a number of important statements about magnetic turbulence and its relation to confinement may be made using globally-defined quantities.

3.1.1. The toroid

Detailed descriptions of the Tokapole II device have been published.[1,2,3] Tokapole II is a torus with a square poloidal cross section and four internal chromium-copper rings. The rings are continuous and hence are driven inductively along with the plasma current, generating a divertor separatrix. The major radius is 50cm and the vacuum poloidal cross section is 44cm square, which includes the rings. The poloidal flux with plasma present is shown in Fig. 3.1. About half the poloidal flux due to the ring current is located around each of the four rings separately (private flux), and the rest links all four rings (common flux). With plasma present, then, the poloidal flux inside the

separatrix is almost entirely due to the plasma current alone. About 80 percent of the total plasma current is located in the square region within the separatrix, which is called this central current channel. This is where all the activity normally associated with a tokamak occurs, such as soft x-ray sawteeth or toroidal ohmic heating. Measurements described as "internal" were taken from the central current channel. Those called "external" were taken from the common flux (or "divertor") region.

Radial positions are measured from the geometric center of the poloidal cross section, which is 22cm from the center of each of the four vessel walls (Fig. 3.1). On the midplane, the outer separatrix is located nominally at minor radius r = 9cm, measured from the geometric center of the poloidal cross section. Due to the lack of profile measurements for all discharges, the absolute location of the separatrix is not consistently verified. In this paper, the separatrix is always taken to be at r = 9cm at the midplane.

3.1.2. Standard diagnostics and fields

The magnetic fields are driven by capacitor banks, sustainable over 10 to 20 milliseconds. The toroidal field (B_t) can be as much as 5500 gauss on axis. The poloidal field circuit drives ring currents of up to 300kA and plasma currents of 40kA when undamped, and 160kA ring currents with 25kA plasma currents when critically damped.

The standard diagnostics include: (1) plasma current derived from a measurement of the primary current; (2) a 70GHz interferometer

for R = 50cm line-averaged density measurements; (3) Ion saturation current measurement in the common flux region between the upper and lower outer rings and the outer wall (two planar probes) at one toroidal azimuth; (4) several soft X-ray PIN diode detectors arranged on the outer wall at a single toroidal azimuth in a vertical array; and (5) toroidal field from calibrated integration of the measured toroidal gap voltage.

Since the separatrix corresponds to a q=∞ surface, the value assigned to q_a, the equivalent edge safety factor, is calculated from a circuit model that gives the edge q of a simple cylindrical tokamak having the same toroidal field, plasma cross-sectional area, and plasma current as the central region of theTokapole discharge in question. The circuit model was originally presented by Sprott,[4] and the calculation involved is as follows. The plasma current I_p and the current in all four of the rings I_r determine the equivalent plasma radius a from

$$a = 17.3\,[\,I_p / (\,I_p + I_r)]^{1/4} \qquad (3-1)$$

where a is then the radius in centimeters of a circle with the same area as the square plasma enclosed by the separatrix. If one assumes the plasma current density is uniform over a circle of radius a centered on the geometric axis, the equivalent edge safety factor is then

$$q_a = 10^{-4}\, a^2\, B_t\, / I_p \qquad (3-2)$$

where B_t is the toroidal field in kG.

3.1.3. The range of safety factor

Tokapole II is capable of producing steady-state discharges (i.e., time invariant current, density, and temperature) of several milliseconds duration with a broad range of edge safety factor, $0.6 \leq q_a \leq 5$. Discharges at the various q_a were optimized for the longest duration and most time-invariant parameters achievable, typically by adjusting both toroidal field and current. It is necessary to remove the critical damping in the poloidal field circuit to reach $q_a \leq 1$. Macroscopic stability over the entire range of safety factor has been carefully studied and previously published.[1-3] In short, Tokapole displays many of the same oscillations and phenomena, such as soft X-ray sawteeth and disruptions, that occur in other tokamaks. Typical parameters for $q_a \approx 0.7$ and 3 are given in Table 3.1.

TABLE 3.1

Tokapole II Parameters

	$q_a \approx 0.7$	$q_a \approx 3$
Toroidal field	~3kG	~5kG
Plasma current	30 – 40kA	15kA
Line-avg. Density	$10^{13}/cm^3$	$6 \times 10^{12}/cm^3$
Electron Temp.	100eV	120eV
Ion Temp.	70eV	40eV
Pulse length	~4msec	~8msec
Loop Voltage	15V	2V
Magnetic Reynolds #	$<10^4$	$\sim 10^4$
τ_E	.05msec	.60msec

It is to be stressed that the discharges were optimized for density, duration, and invariance of parameters, with a particular q_a in mind. This meant that the toroidal field was adjusted as necessary to attain the desired q_a for the obtainable current on each run. Hence, the range of q_a was not achieved by maintaining toroidal and poloidal fields at constant values versus q_a since it was not generally possible to achieve stable plasmas for arbitrary field settings. While this does not necessarily simplify the interpretation of the data, it did provide for the most macroscopically stable discharges, which is a necessary condition for exploring the effects of microscopic instabilities and turbulence. It has been reported by Moyer[5] that the electron conductivity temperature

varies between 75eV and 120eV over the q_a-range. The central electron density varies by only about a factor of 2 over the range of $0.6 \le q_a \le 5$ reported in the present experiment. Hence the plasma β varies mainly because of the changes in magnetic field strength needed to scan q. The possible controlling effects of beta on magnetic turbulence will be investigated in § 4.1.

3.1.4. Confinement characteristics

Energy confinement in the Tokapole II tokamak is estimated globally, due to the absence of detailed radial profile information which is necessary to determine local radial energy flows. Particle confinement has not been measured in this device, and no attempt was made to do so in this experiment. The expression used for global confinement is

$$\tau_E = \frac{3<n>T_e V}{2V_l I_p} \qquad (3\text{–}3)$$

where T_e is the conductivity temperature assuming a flat current profile within the separatrix, $<n>$ is the line-averaged density, V is the interior volume of the vessel, V_l is the plasma loop voltage, and I_p is the plasma current. The ion temperature has been neglected, as it is significantly smaller (~50 eV) than the electron temperature.

It has been found that the global energy confinement scales significantly with q_a. In Fig. 3.2, the total available range of safety factor is represented with the ordinarily associated confinement times. The confinement data for $0.5 \le q_a \le 4.2$ was originally obtained by Moyer,[6]

and these will be the numbers used to represent confinement versus q_a throughout this paper.

A legitimate question to ask about Tokapole II confinement is whether or not it is indeed anomalous. Since it is a low-density, ohmically-heated tokamak, one would expect it to operate in the electron-dominated regime, which may make it particularly sensitive to thermal transport due to processes such as stochastic magnetic fields. But it is indeed possible to estimate the extent of anomalous energy transport in Tokapole II by considering the various loss mechanisms. The loss mechanisms that would generally be considered are radiation, ionization, charge-exchange, and collisional diffusion. It has been crudely determined that radiation losses are comparatively negligible.[7] If ionization and charge-exchange are negligible, as is typically the case for a tokamak, the remaining mechanism is the diffusion due to neoclassical collisional processes.[8,9] To evaluate the neoclassical loss rate one determines the collisionality of the ions and electrons, and evaluates the thermal diffusivities χ_i and χ_e for the respective regimes determined. (Usually the ion channel provides the larger neoclassical loss rate, but diffusivities for both will be presented here.) For Tokapole II discharges with $q_a \approx 2.5$, ($T_e \approx 100$ ev, $T_i \approx 50$ eV, $B_t \approx 4$ kG, $B_p \approx 300$ G, $Z_{eff} \sim 3$), the normalized collision rate for ions is $\nu_* \approx 8.1$ (in the "plateau" regime near the corner to the "banana" regime), corresponding to $\chi_i \approx 8 \times 10^3$ cm^2/sec. For the electrons, $\nu_* \approx 0.3$ ("banana" regime) and so $\chi_e \approx 8.7 \times 10^2$ cm^2/sec, a factor of ten smaller

than the ion value. Then the confinement expected if neoclassical losses dominate is $\tau_E \approx a^2/4\chi_i \approx 3.8$ milliseconds. The measured confinement time from Fig. 3.4 for $q_a \approx 2.5$ is $\tau_E \approx 300$ μsec, a factor of more than ten smaller; hence, the energy transport is anomalous.

3.2. Magnetic probe systems

3.2.1. The magnetic sensor arrays

A variety of coil arrays was employed in this experiment. Initially, a single 40-turn coil of 1mm radius was wound around a machined slot in the tip of a piece of cylindrical fiberglass rod (Fig. 3.3*a*). The leads from the coil were braided together and glued to the rod along its full length. At the other end the leads are soldered to a shielded twisted-pair cable, which carried the signals to an amplifier. No low-resistance termination was included in this configuration. However, the probe calibrations indicated no problems with sensitivity at $f \leq 500$ kHz, as would be expected if lead capacitance were significant. The rod was inserted into a .64cm-outer-diameter, 1.4mm-wall stainless steel tube (Fig. 3.3*c*) that could be pushed into the plasma, and which also provided the vacuum seal and electrostatic shielding. The innermost ten centimeters of the tube were thin-walled (.15mm wall) stainless steel covered with a cylindrical boron nitride particle shield of outer diameter 0.64cm. The portion of the probe containing the coil was always within the particle shield, but could be adjusted to different radii without moving the vacuum jacket.

When all work with single magnetic sensors was completed, namely when profiles for the $q_a \leq 3$ range were completed, multiple-coil probes were built to measure radial correlations. These probes usually consisted of eight radial coils spaced at 1cm radial intervals, with 10 to 25 turns in two layers so that they were of ~1.5mm radial extent, and wound with a 1mm radius around a piece of cylindrical stock, such as alumina (Fig. 3.3*b*). The coils and their leads were made using 42 AWG wire coated with a high-temperature insulator such as polyimide. Coils, stock, and twisted leads were placed in a 0.15mm-wall stainless steel tube which provided electrostatic shielding to coils and leads, as well as protection for the delicate wires. At the other end of the tube was a small aluminum box to shield and protect the solder joints. The leads were soldered to sturdy, individually shielded twisted-pair cables. The leads and cables carried the signals to the amplifiers. These cables were terminated in two 50 Ω resistors so that they were driven balanced with respect to the shield. These strong cables were shielded as a group by an external copper braid, grounded with the amplifiers, and connected to the aluminum box and stainless steel tubing to form a complete external shield.

A third useful probe design was a combination single magnetic sensor and Langmuir probe, which could measure correlations between electrostatic and magnetic turbulence. Shown in Fig. 3.4, this probe consisted of a coil fixed within a boron nitride-clad .25mm-wall stainless tube. The Langmuir portion was a .44mm-diameter tungsten wire

inserted through the single-bore alumina stock that held the magnetic coil, which extended through a hole in the tip of the particle shield 3.1mm into the plasma. The vacuum seal was maintained at the other end of the support tube. In this configuration, the magnetic sensor and Langmuir tip were separated radially by ~3mm. (As will be shown in § 4.2, this is much less than the radial coherence length of magnetic turbulence for the frequencies considered.)

Because these probes were placed well into the tokamak discharges, some discussion of probe disturbance of the plasma is appropriate. It was found that for the frequencies considered here (0 – 400kHz), no significant variation of the amplitude or frequency characteristics of the signal from a probe outside the separatrix occurs when a second probe is positioned inside at a different toroidal location. In addition, once a desired q_a is obtained with internal probes, global parameters and their profiles to the extent that they are known are found to be the same as would be obtained for that q_a without probes. The exception to these assertions occurs for probes placed at radii less than 6cm in discharges with $q_a \geq 1.5$. For two such cases ($q_a \approx 3$ and 4.2) magnetic turbulence data was obtained as far in as $r = 4$cm, despite the reduction of the edge signal amplitudes and small reduction of plasma current in the discharges. The $q_a \approx 3$ radial profile data was taken from a single coil. Thus, the edge measurements presented are unaffected by the internal ones. The $q_a \approx 4.2$ profiles are not inconsistent with those

for $q_a \approx 4.0$, which had a probe only as far in as $r = 6$cm; thus, the perturbation of the turbulence profile by the probe at $r = 4$cm is small.

3.2.4. Amplifiers, filters, and transmission lines

In order to digitize and store instantaneous sensor signals, the original probe signals had to be frequency filtered and amplified to improve the signal-to-noise ratio at the digitizers. In addition, ground-referencing of the equipment had to be provided, as well as elimination of external noise. This required the use of very flexible amplifiers, good low-pass filters and isolation filters (external to the amplifiers), and noise-proof cabling systems. As the experiment progressed into the correlations measurements, the isolation and noise-elimination systems became more elaborate, and various systems were used. Only the most frequently used systems will be described here, since the variations with functionality and availability of equipment were too numerous and ineffectual to describe.

The amplifiers used in this work were Tektronics AM502 variable-gain differential amplifiers with 0-1MHz frequency response. Gain factors used varied from 200 to 5000, depending on sensor location and discharge type. AM502's have internal upper and lower adjustable single-pole frequency filters. For radial coils, the lower filter was set to 0 (i.e., DC response) and the upper was set according to the demands of the external filtering system used. For toroidal and poloidal field signals there is a strong DC component resulting from the pulsing of these fields that is unrelated to plasma turbulence. These low-frequency

signals were eliminated by the low-f filters internal to the AM502's being set to roll off below 1 kHz.

Two distinct systems were used to filter and transmit the output signals of the AM502's. One was used only for the single-sensor probes described previously. The single sensor was connected to the amplifier with one lead at ground (not differentially). The probe vacuum jacket and amplifier were grounded at the vacuum vessel wall. The high-f filter on the AM502 was set to roll off above 300kHz, and its output was connected to a unity-gain optical isolation amplifier by a six-meter-long 50Ω coaxial cable. The isolation filters fed the ground-filtered signals to the digitizers.

For the multiple-sensor systems, the configuration used was designed to accommodate many simultaneous signals with minimum noise and crosstalk coupling loss. Each sensor was amplified differentially, with its balanced termination centered about the amplifier ground. The probes, as described above, included careful electrostatic shielding, and in like fashion, the amplifiers were placed within a Faraday cage. Each amplifier's high-f filter was set at 1MHz, and was connected to a low-pass filter/line driver circuit. These filters were connected to a multiple-conductor cable which transmitted the signals to the digitizers.

3.2.5. Calibration of the sensors

For the amplifier-filter-transmission system used, a calibration of coil-sensitivity was done as a function of frequency. This involved the

use of a carefully constructed Helmholz coil and a frequency generator with resistor to measure current through the coil (Moyer[10]). With the calibration available, the power spectrum (volts^2/frequency) of a given probe could be converted into gauss^2/frequency directly, and the result can be integrated to find the total RMS (root-mean-square) fluctuation amplitude. This will be discussed in § 3.3.

3.2.6. Digitization and Storage

All fluctuations data reported in this paper were digitized at a frequency of 1MHz. A finite time record of 256 points then has a period T = 256 microseconds. Various data acquisition systems were employed, including the DAMP system (DEC RT-11), DAS (DEC RSX), and MDS (VAX VMS). The ensemble average processing was done using IDL for both the DAS/DAMP storage files (DAS and DAMP files were of the same format), and those of MDS. The problem still exists in this field that there is no established database system for fluctuations data.

3.3. Spectral analysis methods

The principal type of analysis done for this paper is known as standard spectral analysis, including determination of power spectra, RMS amplitudes, correlation functions, coherence, and phase. The main references for the forms of these functions presented below are Bendat and Piersol,[11] and Brigham.[12] The analysis is concerned with the continuous, ensemble-averaged behavior of the probe signals. Specific events associated with large sporadic field changes, such as internal

disruptions or soft X-ray sawtooth crashes, were specifically *avoided* in the ensembles. This was true mainly because they were infrequent on the 128-256μsec time-scales of the data records selected in this analysis. Also these activities caused the digitizers to saturate because the response was so large compared to the more continuous turbulence.

3.3.1. Fluctuation amplitudes and spectra

The first and most important feature of any turbulence data analysis is the way the magnitude of the fluctuating quantity is determined. For a randomly-fluctuating quantity such as the magnetic field b(t) over a time period T which involves many frequency components, the amplitude should be expressed as a root-mean-square (RMS) value, given by

$$\tilde{B} \equiv \left(\frac{1}{T} \int_0^T b^2 \, dt \right)^{1/2}. \qquad (3-4)$$

which is easily determined without spectral analysis.

The signal from a magnetic sensor coil is not a B(t), but rather a $\dot{B}(t) = dB(t)/dt$. To use the above formula, one would first have to integrate the signal in time before proceeding. An alternative approach, used in the calculations for this thesis, is to use Fourier analysis, coupled with a frequency calibration of the entire probe-amplifier-transmission system (described in § 3.2.5). Let $\dot{B}(t)$ be a finite time record of a magnetic probe signal in volts, with period T. If $\dot{B}(f)$ is the Fourier transform of

$\dot{B}(t)$, and $C(f)$ is the calibration of the probe system in Gauss/volt, then the RMS fluctuation value in Gauss is given by

$$\tilde{B} = \left\{ \int df \, (C(f))^2 \frac{1}{T} \left\langle \left| \dot{B}(f) \right|^2 \right\rangle \right\}^{\frac{1}{2}} \qquad (3-5)$$

where "< >" indicates an ensemble average.

The discrete form of this, actually encoded in the computer software, is as follows:

$$\tilde{B} = \left\{ \frac{1}{N^2} \sum_{n=1}^{N} C_n^2 \left\langle \left| \dot{B}_n \right|^2 \right\rangle \right\}^{\frac{1}{2}} \qquad (3-6)$$

where the frequency range may be restricted by appropriately changing the limits of the summation. $\dot{B}_n$ is the Fast Fourier Transform obtained from the $N = 2^Y$ algorithm presented in Brigham.[13] The extra factor of N in Eq. (3 – 6) is an artifact of the discrete Fourier transform. In some software packages, such as IDL, the extra $N^{-1/2}$ is already included in the FFT routine.

The amplitude spectrum $\tilde{b}(f)$ in Gauss/$(kHz)^{1/2}$ is given by

$$\tilde{b}(f) = C(f) \left[\frac{1}{T} \left\langle \left| \dot{B}(f) \right|^2 \right\rangle \right]^{1/2} \qquad (3-7)$$

which has the discrete analog

$$\tilde{b}_n = C_n \left[\frac{1}{N^2} \left\langle \left| \dot{B}_n \right|^2 \right\rangle \right]^{1/2} \qquad (3-8)$$

The square of the amplitude spectrum is the power spectrum of B(t). The ensemble averages for amplitudes and amplitude spectra included 30 to 100 terms, with T = 256μsec.

3.3.2. *Correlation, coherence, and phase*

In addition to the amplitude, the scale lengths of the turbulence are also useful in attempting to understand its causes and effects. These are determined ordinarily by correlation analysis. This analysis requires large ensembles, particularly in the evaluation of the normalized spectral correlation, or "coherence". For the correlation analysis presented in this paper, the ensembles usually consisted of ≥ 100 data records of period T = 128 μsec. The specific functions calculated in correlation analysis are the correlation function, the coherence, and the phase.

The correlation function gives a power weighted measure of the degree of causal relation between to signals x(t) and y(t). It is defined as follows:

$$R(\tau) = \frac{\left\langle \int x(t)\, y(t+\tau)\, dt \right\rangle}{\left[\left\langle \int x^2(t)\, dt \right\rangle \left\langle \int y^2(t)\, dt \right\rangle \right]^{\frac{1}{2}}} \qquad (3-9)$$

where τ is the time-delay, and < > denotes an ensemble average over many data records. The cross-power spectral density is defined as

$$|\Gamma_{xy}(f)| = \frac{1}{T} \left| \left\langle X(f)\, Y^*(f) \right\rangle \right| \qquad (3-10)$$

Then the coherence, $\gamma(f)$, is the normalized cross-power spectrum:

$$\gamma_{xy}(f) = \frac{|\Gamma_{xy}(f)|}{\left[\Gamma_{xx}\, \Gamma_{yy}\right]^{\frac{1}{2}}} \qquad (3-11)$$

This is a measure of the causal relationship between two signals x and y at the particular frequency f, where a $\gamma = 1$ indicates a totally causal relation, and a $\gamma = 0$ indicates signals that are unrelated at f. The relative phase $\theta(f)$ is determined from the complex parts of Γ:

$$\theta(f) = \text{Arctan}\left[\frac{\text{Im}\,(\Gamma)}{\text{Re}\,(\Gamma)}\right] \qquad (3-12)$$

Scale lengths are found from the change in amplitude with location in some relevant direction, as well as the decay in $\gamma(f)$ with separation in relevant directions. In particular, the coherence length, the *e*-folding distance of γ, is defined as $L_d(f) = s/(-\ln \gamma(f))$, where s is the separation, and d is a label for the direction of s. These scale lengths are useful in evaluating what theoretical approach might be appropriate to explain the presence and to ascertain the consequences of the turbulence. The radial scale lengths indicate the radial extent of the magnetic oscillations, and in so doing, limit the region affected by the cause of the turbulence being considered. The causes of short scale-length magnetic turbulence are presumably local perturbed currents in the region of the coil. Long scale-lengths are caused by large-scale modes whose resulting

disturbances may propagate over the entire plasma without much amplitude decay or phase distortion, and the sources of the measured turbulence from these modes are not necessarily localized to the region of the coil.

The poloidal mode structure will be investigated using two distinct methods. First, the relative phase θ of poloidally-separated probes is related to the poloidal mode number m via $m = r\theta/s$, where s is the separation of the coils. The second methods employs the assumption of cylindrically symmetric vacuum field decay outside the plasma. In this case, m is found by fitting the radial amplitude decay of $b_r(f)$ to a curve of the form $r^{-(m+1)}$. There is a presumption here that the toroidal mode number n is low.

3.3.3. Uncertainty calculations

The uncertainties presented in this thesis are entirely from the statistics of the available ensembles. It is these uncertainties that are the error bars in the data plots. The measurements at a given safety factor could not be repeated often enough to give the day-to-day consistency of the turbulence.

Uncertainties in the power spectra were calculated as the standard deviation of the average, by retaining the individual power spectra calculated for each data record in the ensemble. The error in the RMS fluctuation level, since it is an integral of the power spectrum, is derived from the standard error propagation from the individual uncertainties

of the points in the power spectra. (All of this requires considerable computer memory.)

The uncertainties in the coherence spectra were assumed to be dependent only on the size of the ensemble. It was found by computation that the average value of the cross-coherence function of two independently-generated purely random data ensembles is equal to $N^{-1/2}$, where N is the number of terms in each ensemble. This implies that the smallest value of a coherence function at any frequency which is believable is $N^{-1/2}$. This is the value presented in this paper for the limit of resolution of $\gamma(f)$ in § 4.2. The uncertainty in the coherence length L is also taken to be determined by N. Since the coherence might always be smaller by an amount $N^{-1/2}$, the uncertainty in L is calculated by taking the difference between the value calculated from $L = s/(-\ln(\gamma(\omega))$, with s the sensor separation, and the value calculated from $L = s/-\ln((\gamma(\omega) - N^{-1/2}))$. Further, there is a limit of resolution, given by a flat, dashed line on all plots of coherence lengths. This is the value of $L_{limit} = s/(-\ln N^{-1/2})$, because no value of coherence below $N^{-1/2}$ should be accepted as true.

No uncertainties have been calculated for the phases given in § 4.3. The software for this was not developed in time for this thesis. It is strongly recommended that the procedures given in Bendat and Piersol [11] be encoded for future turbulence studies in Tokapole II.

REFERENCES

[1]T.H. Osborne, R.N. Dexter, S.C. Prager, Phys. Rev. Lett. **49**, 734 (1982).

[2]N.S. Brickhouse *et al*, in *Proceedings of the Tenth International Conference on Plasma Physics and Controlled Nuclear Fusion Research*, London, 1984 (IAEA, Vienna, 1984), p. 385.

[3]R.A. Moyer, Ph.D. thesis, Magnetic and Material Limiter Discharges in Tokapole II, University of Wisconsin-Madison, (1988).

[4]J.C. Sprott, University of Wisconsin – PLP 712 (1978).

[5]R.A. Moyer, ref. 3, p. 113.

[6]R.A. Moyer, ref. 3, p. 89

[7]R.N. Dexter, private communication.

[8]F.L. Hinton and R.D. Hazeltine, Rev. Mod. Phys. 48, 239 (1976).

[9]Status of Tokamak Research, edited by J.M. Rawls, DOE/ER-0034, (1979) p. 2-21.

[10]R.A. Moyer, ref. 3, p. 103.

[11]J.S. Bendat and A.G. Piersol, **Random Data**, J. Wiley and Sons, New York, NY, (1986).

[12]E.O. Brigham, **The Fast Fourier Transform**, Prentice-Hall, Englewood Cliffs, NJ, (1974).

[13]E.O. Brigham, ibid., pp. 161, 164.

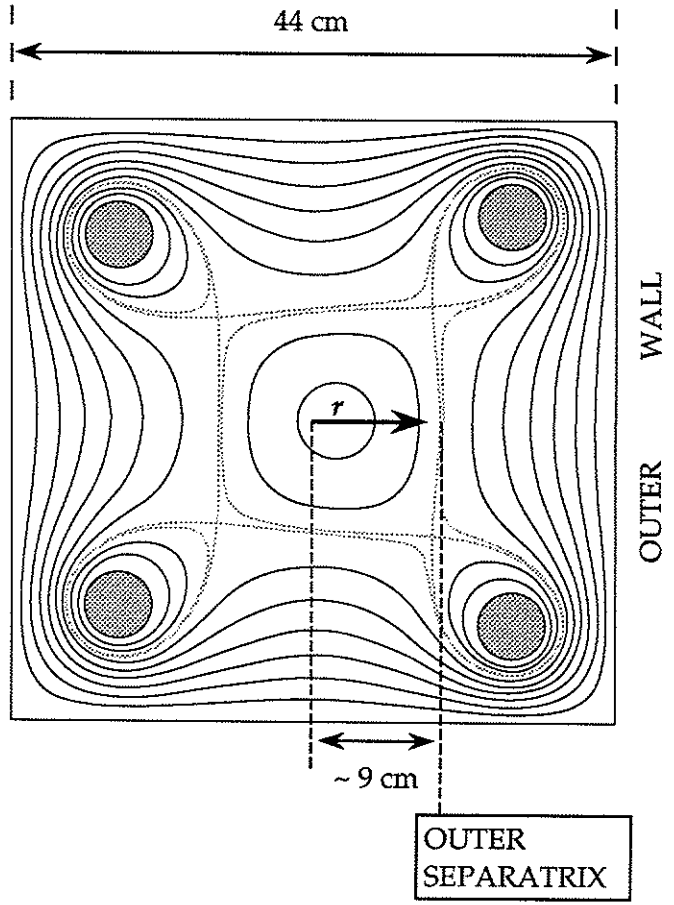

FIG. 3.1. Poloidal flux plot of Tokapole II. The four shaded circles are the cross sections of the rings. In this paper, the minor radius r is measured from the geometric center of the machine as shown, not from the magnetic axis. As shown, probes entering the machine from the outer wall reach the separatrix at $r = 9$cm.

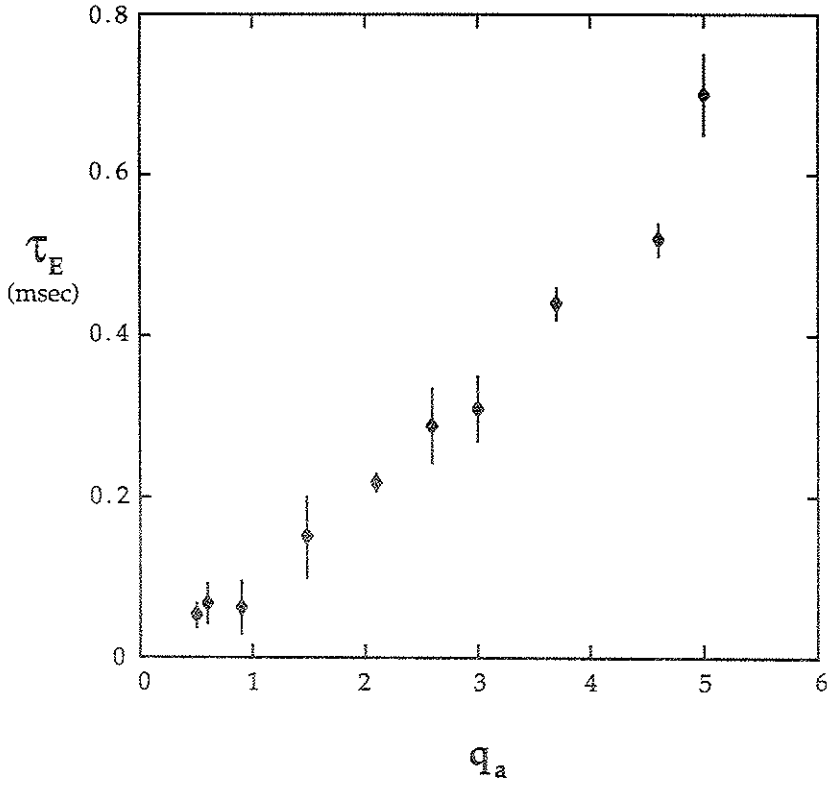

FIG. 3.2. Systematic variation of the confinement time with equivalent edge safety factor in Tokapole II. The data are quite linear on this scale up to $q \approx 4$.

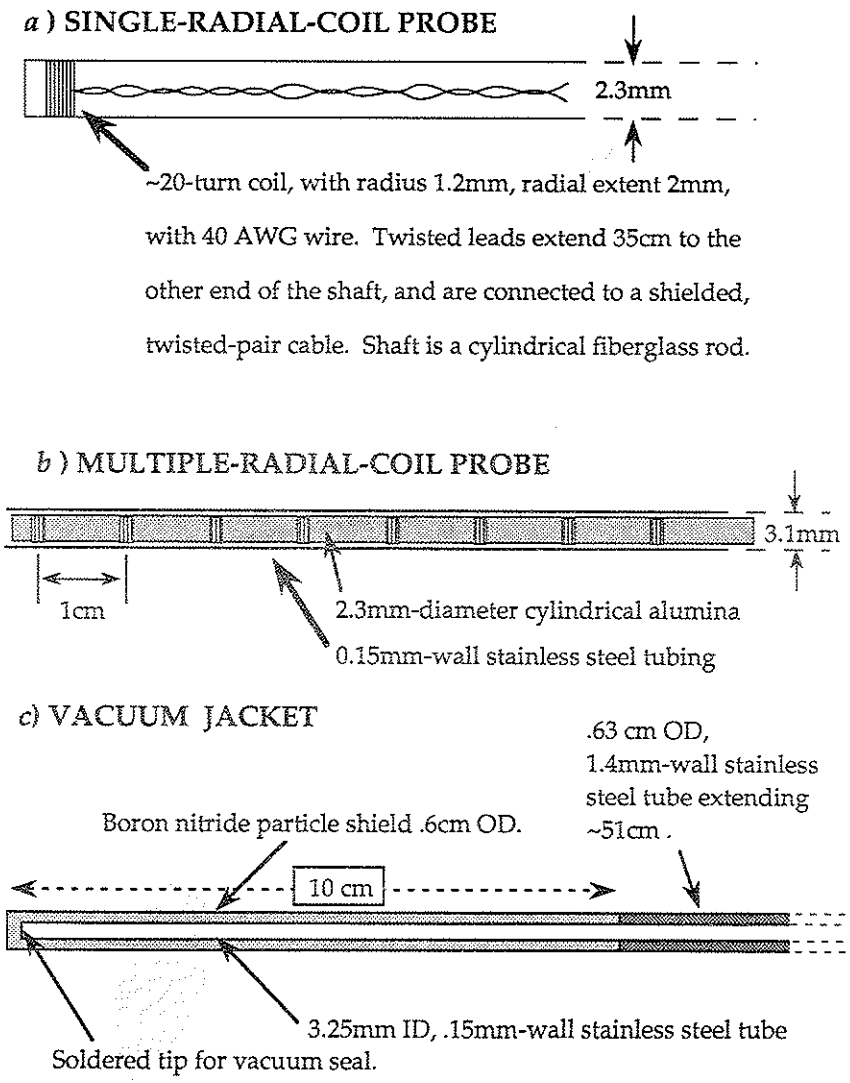

FIG. 3.3. The single and multiple radial magnetic sensors, and the vacuum jacket into which they slide for measurements in the plasma.

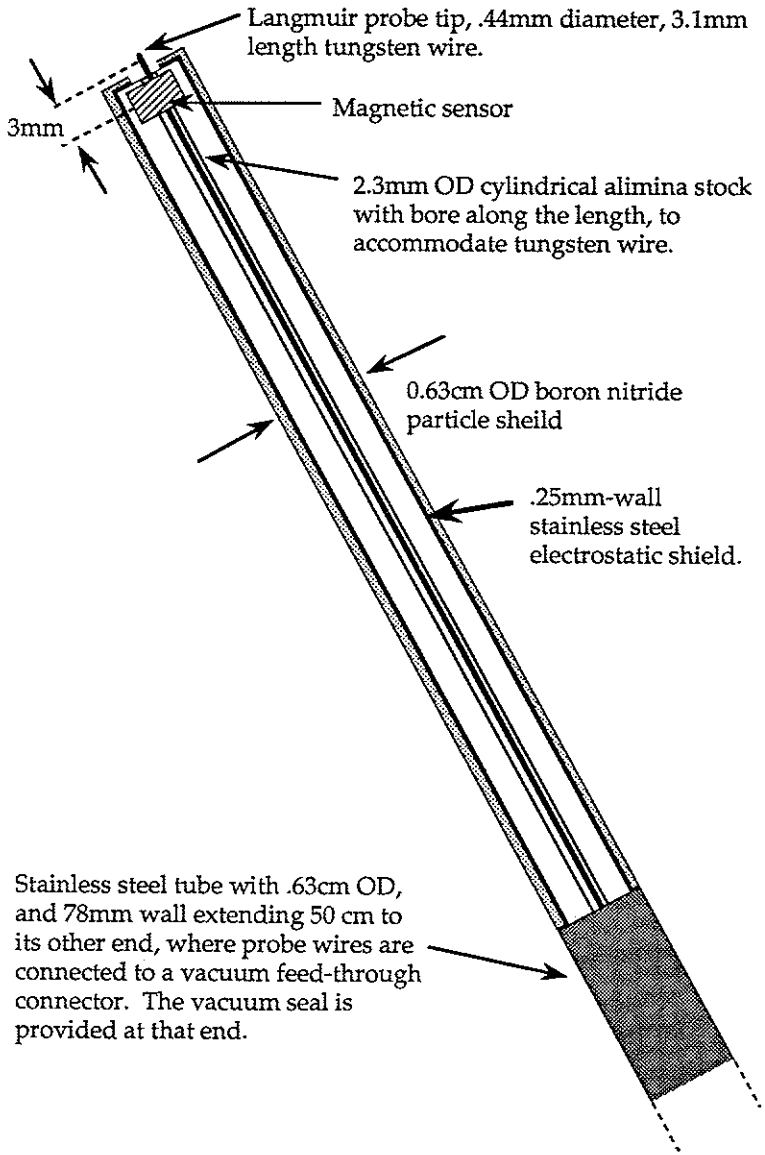

FIG. 3.4. The combination Langmuir and magnetic probe, with the two sensors separated radially 3mm when in the plasma.

CHAPTER 4:

Description of Experimental Results

The following is an extensive and detailed description of the magnetic turbulence amplitude and correlation measurements in the range of 10 - 400 kHz made on Tokapole II. Thirty to sixty percent of the total fluctuation power in this range appears below 100 kHz. As will be shown in § 4.2, the frequency range 10 - 100 kHz is dominated by fluctuations with very long radial and poloidal coherence lengths. These are not properly considered microturbulence, and do not apply specifically to microturbulent transport processes or microinstabilities. Nevertheless, they do scale in much the same way as the turbulence over 100-400 kHz. To allow for visualization and interpretation of both the full-range data and the high-f-only data, many figures in § 4.1 include the RMS fluctuation levels over both ranges, 10 - 400 kHz and 100 -400 kHz, as will be indicated in the figure texts.

4.1. Magnetic turbulence amplitude

4.1.1. Radial profiles

Radial profiles of the magnetic turbulence amplitude for discharges of various q_a are shown in Fig. 4.1, where $\tilde{B}_r$ is total for the frequency range 10-400 kHz. Included are the extreme values of q_a, as well as those for which measurements were made at minor radii less

than or equal to the nominal sawtooth-inversion radius for low to intermediate q_a, taken to be at $r \approx 6$cm. The profiles become higher and broader with decreasing q_a. For the available data, however, profiles flatten within the sawtooth-inversion radius at any q_a.

It is known that density profiles also broaden with decreasing q_a, and a comparison of existing estimates of such profiles with those of $\tilde{B}_r$ seems appropriate. Fig. 4.2 gives the comparison of measured ion saturation current (J_{sat}) from a Langmuir probe to that of $\tilde{B}_r$ at a point displaced 3mm radially for two q_a cases. The profiles are well matched in each case, suggesting that the turbulence may follow the equilibrium profiles such as density, pressure, and temperature.

Breaking the turbulence down according to frequency, the radial profiles including the separatrix region are as shown in Figure 4.3. The broadened low-q profiles still contrast with the narrow, peaked profiles at high-q. Also notable is that the high frequency profiles tend to decay faster with r in both q cases, indicating the high frequency oscillations are more restricted to the region within the separatrix. For $q_a \approx 0.7$, the decay outside the separatrix is monotonic. For $q_a \approx 4.2$, however, the external turbulence does not decrease with radius for some frequencies. This may indicate the presence of runaway electrons for those discharges in the edge.

4.1.2. $\tilde{B}_r$ *and confinement*

Initial measurements of magnetic turbulence at various q_a revealed that q_a was a control parameter for the fluctuation level as well as the global energy confinement in Tokapole II. A demonstration of this is shown in Fig. 4.4 for the full range of q_a. Here, $\tilde{B}_r$ is measured at r = 8cm, and is normalized to the local equilibrium field. The energy confinement time τ_E is estimated using an estimated conductivity temperature and a flat current profile within the separatrix. The confinement decreases as q_a is lowered and the fluctuations increase. This would be expected if $\tilde{B}_r$ were an important source of transport. However, a causal relation between τ_E and $\tilde{B}_r$ is not established by this comparison.

The confinement time τ_E was found to vary smoothly with optimized while discharges scanning q_a. This was done with a variety of plasma current and toroidal field settings. Density and electron conductivity temperature remain relatively constant. Hence, τ_E does not vary smoothly with any other combination of these parameters.

It may be of some use to find a scaling relation to predict the magnetic turbulence amplitude for given field settings. The best fundamental scaling parameter for the magnetic turbulence seems to be plasma current (Fig. 4.5). $\tilde{B}_r$ scales approximately as $I_p^{3/2}$, disregarding the variations in toroidal field, for turbulence data at r = 8cm. If turbulence is compared to B_t disregarding current, as in Fig. 4.6, the scaling is inconsistent at low amplitudes, which correspond to high q.

(A variety of q_a's could be established at a given toroidal field setting only at high q_a.) Hence toroidal field is influential but not as smooth a scaling parameter for $\tilde{B}_r$ as is plasma current. A combination of plasma current and toroidal field is perhaps the best way to predict turbulence levels for given field settings, and an example of this is q_a itself. One finds, then, that

$$\tilde{B}_r/B \approx 4.24 \times 10^{-4}\, q_a^{-1.78} \qquad (4-1)$$

will describe the turbulence in Tokapole II over $0.6 \le q_a \le 5$, for 100 - 400 kHz data at r = 8cm (microturbulence only), as shown in Fig. 4.7. Similar expressions with slightly different constants would be found for data at other minor radii.

To consider further the relation between τ_E and $\tilde{B}_r$, a plot of normalized τ_E versus normalized magnetic fluctuation level is shown in Fig. 4.8*a-c*. Here, τ_E was made dimensionless using $\tau_E = a^2/4\chi_e$, with electron thermal diffusivity $\chi_e = L_0\, v_{th}\, (\tilde{B}_r/B)^2$, as per the collisionless form of the stochastic magnetic fields transport coefficient as derived by Rechester and Rosenbluth.[1] The parallel correlation length L_0 is taken to be invariant at a value of 1.5m (§ 4.2). The results (Fig. 4.8*a*) indicate that $\tilde{B}_r$ has no effect on confinement for sufficiently low amplitudes (corresponding to $q_a \ge 3$). For higher turbulence, though, there appears a rapid decrease in the normalized τ_E. This suggests that some effect has become important relating $\tilde{B}_r$ and τ_E at normalized turbulence amplitudes of ~3×10^{-4} (considering the 100-400 kHz data). Similar

results are seen for fluctuations measured at r = 6cm (Fig. 4.8*b*) and r = 4cm (Fig. 4.8*c*), but the data set is more limited. In any case, the normalized fluctuation level is only large enough to satisfy the above equations for τ_E and χ_e at the highest $\tilde{B}_r$ values (low q_a) with the full frequency range included.

Certain microinstabilities, such as electromagnetic drift-wave turbulence[2] predict a dependence of $\tilde{B}_r/B$ upon β. In Fig. 4.9 the relation between normalized turbulence and β is presented. Here, $\beta = 2\mu_0\, n T_e/B^2$, with $n = 10^{19}/\mathrm{m}^3$ and T_e is the electron conductivity temperature, and B is the local net magnetic field at r = 8cm, so this is a local beta. (The ion contribution has again been neglected.) As shown in Fig. 4.9, a minimal β was obtained for which fluctuations could vary considerably at the lowest levels measured (high q_a). For higher β, the fluctuations increased, attaining values into the 10^{-4} range and higher for the frequency range 100 - 400 kHz. Recall that at turbulent amplitudes of ~3×10^{-4} (r = 8cm) the normalized confinement in Fig. 4.8*a* was seen to fall rapidly. This is as much as can be said at this point about possible causal relationships between discharge parameters, turbulence amplitude, and confinement. Further experimentation is needed to prove there is really a causal relationship between $\tilde{B}_r$ and τ_E.

4.1.3. Frequency spectra

The $\tilde{B}_r$ frequency spectra for several values of q_a are shown in Figures 4.10, 4.11, and 4.12. Data at r = 8cm, in the region of equilibrium gradients and outside the sawtooth-inversion radius, are shown in Fig.

4.10. For frequencies above ~100 kHz, the spectra are predominantly featureless for all q_a, decaying as a power of frequency f. The power law is different for $q_a > 4$ than for $q_a < 4$. For the lower q_a's, the exponent is –1.4, while for $q_a \approx 5$, the exponent is –2.3. For $q_a \approx 4$, both power laws are observed, with $f^{-1.4}$ decay appearing over ~60-200 kHz, and $f^{-2.3}$ governing for higher f. At frequencies below ~100 kHz, the character is q-dependent, ranging from conforming to the high-frequency power law at $q_a \approx 0.7$, to being very broad and flat to 80 kHz before assuming a power law decay for $q_a \approx 5$. For the higher-q_a cases, there appear one or more peaks in the spectra, suggesting that coherent modes might be present. Further discussion of this will follow in the evaluation of correlation scale lengths in section 4.2.

In Fig. 4.11, similar data are shown, but for r = 6cm. Levels are higher than for r = 8cm, and the same trend in amplitude with q_a appears. The characteristics of the turbulent spectra are much the same as for r = 8cm, with the same power law ($f^{-1.4}$) present at $0.7 \le q_a \le 4$, and with $q_a \approx 4.2$ showing a dual power-law-decay character, with a decay of $f^{-1.8}$ from 50 to 200 kHz, and $f^{-2.3}$ for above 200 kHz.

Inside the sawtooth-inversion radius, the spectra for $q_a \approx 0.7$, 3, and 4.2 are as shown in Fig. 4.12. The power law in the $q_a \approx 0.7$ and 3 cases is again $f^{-1.4}$. The q ≈ 4.2 spectrum shows the dual character again, following $f^{-1.4}$ over 30-200 kHz, and then shifting to exponent –2.3 for higher f. It is suggested that the similar frequency spectra indicate the same underlying cause or set of causes is involved in generating the

turbulence. The $f^{-1.4}$ power law dominates the microturbulent spectrum for $q_a \le 3$, and the normalized confinement for this range of q_a shows a strong variation with turbulence amplitude in Fig. 4.8*a*. Hence the underlying cause of the $\tilde{B}_r$ may strongly influence confinement.

The radial magnetic fluctuations have been emphasized here because the radial component is associated with the various magnetic transport processes presented in § 2.2. Other components have been measured to determine the polarization of the turbulence. Figure 4.13 shows a comparison of the spectra of $\tilde{B}_r$, $\tilde{B}_p$, (poloidal) and $\tilde{B}_t$, (toroidal) all at r = 4.5cm for $q_a \approx 0.6$. The poloidal component magnitude is about 1.4 times that of the radial component, while the toroidal fluctuations are smaller by about a factor of 5. All three spectra have about the same frequency structure. Toroidal and poloidal fluctuations data for higher q_a inside the separatrix are unavailable. Outside the separatrix, specifically at r = 11.7cm, the poloidal fluctuations are twice the level of the radial, with the same frequency structure for $q_a \approx 0.6$ and 2.5 (Figs. 4.14 and 4.15). Toroidal turbulence shows a frequency structure similar to the other components in both q-cases, smaller than $\tilde{B}_r$ by a factor of 3 for $q_a \approx 0.6$, and by a factor of 5 for $q_a \approx 2.5$. Since the field is more purely toroidal at higher q_a, the reduced level of $\tilde{B}_t/\tilde{B}_r$ at higher q may mean that the turbulence parallel to the field is small, and perhaps negligible. The similar frequency spectra at high f indicates again the same physical

process may be involved for all three components of the field, and this process may be related to the microturbulent transport.

4.2. Correlation and coherence measurements

Another important characteristic of turbulence is the correlation scale lengths associated therewith. When a signal which is random in time is *not* random in space, i.e. the spatial correlation is non-zero, a causal relation may be said to exist between the measurements at one point to measurements at another. The correlation measurements, then, give an important insight into the nature of the modes and instabilities present, because they provide an estimate of the radial extent of the modes.

The second area of prime emphasis of this work is a detailed correlation mapping of discharges versus q_a. This was done in the hope of providing previously unavailable data concerning the radial extent of internal magnetic microturbulence, as well as some measure of the mode structure thereof. This information may prove helpful in the derivation of improved theoretical models of $\tilde{B}_r$ and its associated transport. All correlations presented here are for radial magnetic turbulence.

4.2.1. *Radially - displaced sensors*

One suitable estimate of the degree of correlation between two simultaneous samples of turbulence data is the absolute maximum of their cross-correlation function. Since this correlation function is one in

time and not a Fourier decomposition of the data, its properties are weighted by the power of the many Fourier components included in the cross-correlated time-records. If $R(\tau)$ is the correlation function with τ the time-lag variable, then the quantity desired is $|R|_{max}$, and the corresponding time-lag is then τ_{max}. For radially-displaced sensors in Tokapole II, it is experimentally determined that $\tau_{max} \approx 0$ μsec always when the full 10 to 400 kHz frequency range is included. The meaning of this is that the highest-power fluctuations exhibit no phase shift in the radial direction. This is not true for sensors displaced poloidally or toroidally.

The multiple-coil radial arrays used in this experiment are well suited for radial correlation decay measurements for the 0–400 kHz frequency range. A single coil, perhaps the one at the smallest minor radius, can be chosen as a reference, and cross-correlated with successively more distant coils. The result is a measure of the gross correlation decay with distance. For Fig. 4.16, this calculation was done for $q_a \approx 0.7$, using the innermost coil as the reference. (For one set of points, the innermost coil was at $r = 4$cm, and for the other set, the innermost coil was at $r = 9$cm. Fig. 4.17 is the same but for $q_a \approx 4.2$. The value of $|R|_{max}$ decreases more quickly for coils within the separatrix than for those outside. This is found to be true for all q_a. It indicates fewer sources of turbulent currents in the divertor region, a result of the separatrix magnetically limiting the discharge.

With the reference coil at r = 6cm, the correlation decay for various q_a are shown in Fig. 4.18. The decay is faster for the higher-q cases. The same result is found for the two available cases with the reference sensor at r = 4cm (Fig. 4.19). The curves indicate mostly the extent of the high-power activity which corresponds to low frequencies (f < 100 kHz). To investigate the correlation of oscillations as a function of frequency, the *coherence* must be calculated.

The coherence is a measure of the correlation of two signals at specific frequency intervals such that the correlation at each interval is linearly independent of the correlation at all other intervals. Hence, except for numerical error, the coherence for a low-power oscillation at one frequency will not be influenced by high-power fluctuations at other frequencies. The coherence, $\gamma(f)$, versus radial separation from r = 4cm for $q_a \approx 0.7$ is shown in Fig. 4.20. While the low-f coherence decays slowly with distance, the high-f components exhibit rapid decay. In any case, the radial decay is not consistent with separation, indicating the variation of coherence lengths with minor radius. To find local coherence lengths (the e-folding distance of the coherence as a function of frequency), it is necessary to restrict the radial region of the data considered in the calculations. This was done by using signals from adjacent coils along the 8-coil radial arrays, and the minor radius quoted for the result is the average of the two coils' radial locations.

An example of radial coherence lengths versus frequency is shown in Fig. 4.21 for $q_a \approx 0.7$ at r = 4.5cm. At frequencies below

~100 kHz, the coherence lengths are quite large, even with respect to the tank dimensions. This turbulence is a large-scale effect and, despite its broadband character, is not properly considered microturbulence. This does not mean that no microturbulence is present in this range of frequencies. It does mean that most of the power at these frequencies is coming from coherent oscillations. Above 100 kHz, the coherence lengths become small compared to the plasma radius. Values of $L_r(f)$ from 0.5 to 2.5 cm are found. Turbulence with this scale-length characteristic is what has been called "microturbulence" in this work. Hereafter, the radial coherence of only the high-frequency, microturbulent modes will be discussed.

Radial coherence lengths inside the separatrix are relatively independent of q_a for $0.6 \le q_a \le 3$, but for higher safety factors the coherence lengths are measurably shorter (by about a factor of 2), as shown in Fig. 4.22 with data at r = 6.5cm. Recall that the frequency structure of the microturbulence is also somewhat different at $q_a > 3$ (Fig. 4.10). These L_r results again suggest that different physics is involved in discharges with the higher q_a's. At r = 4.5cm (Fig. 4.23) and r = 8cm (Fig. 4.24), similar results are found. The plots all show relatively large uncertainties and sporadic variations. This is partly due to the limited linear scales used, but may also suggest that the data are not perfectly stationary statistically. It is the general behavior of $L_r(f)$ that is considered here, and not the details of the high-f spectrum.

It is now appropriate to look at coherence lengths as a function of radius for a range of safety factor. Fig. 4.25 shows the variation of microturbulent coherence lengths with minor radius for $q_a \approx 0.7$. Coherence lengths are shown for r = 4.5cm (inside the separatrix), for r = 8.5cm (near the separatrix), and for r = 14.5cm (outside the separatrix). A similar plot for $q_a \approx 2.8$ is Fig. 4.26, and for $q_a \approx 4.2$ is Fig. 4.27. The average of the coherence lengths increases with increasing r. Outside the separatrix, coherence lengths are significantly larger than inside for $q_a \leq 2.8$. The high coherence in the edge indicates that sufficiently far outside the separatrix the region is more vacuum-like. Hence, radial amplitude decay measurements might be made to estimate the poloidal mode structure. Radial decay measurements will be discussed in § 4.3. Radial coherence lengths increase more gradually at $q_a \geq 2.8$ because of reduced edge correlation in these higher-q_a discharges. This reduced edge correlation indicates the presence of perturbed current sources in the edge meaning that this region is less vacuum-like above $q_a \approx 2.8$ than for lower q_a. Radial amplitude decay measurements are much less believable for $q_a \geq 2.8$. In any case, the separatrix seems to have no sudden effect on the microturbulent coherence, since $L_r(f)$ changes smoothly from the exterior, through the separatrix, to the interior.

4.2.2. Poloidal correlations and Δm.

Poloidal correlations measurements are helpful in describing the poloidal mode structure of the turbulence. In this thesis, the direction "poloidal" is perpendicular to the toroidal field and the radial direction,

not perpendicular to the equilibrium field and radial direction. Probes with radial sensors were placed in the machine at a single toroidal azimuth with one- or two-centimeter poloidal displacements. Since these were also the standard multiple-coil radial arrays, poloidal correlations at several radii could be taken simultaneously.

As with the radial correlations, $|R|_{max}$ versus poloidal separation for two cases of q_a will be presented first (Fig. 4.28). Recall that $\tau_{max} \neq 0$ for poloidally separated sensors. In contrast to the radial correlations, these values decay quickly with separation for both q_a's. The poloidal coherence decay for the two cases at r = 6cm is shown in Fig. 4.29. Again, the lower frequencies are the most coherent. The calculated coherence lengths are shown in Fig. 4.30. The low-q coherence lengths at f>100 kHz are shorter than for high q.

Poloidal coherence lengths are an indication of the spread in poloidal mode numbers at a given frequency, by the relation $\Delta m = \pi r/L_p$. Figure 4.31 gives the Δm versus frequency for the low- and high-q cases considered here, for r = 6cm. A clearly broader m-spectrum exists at low q_a than at high q_a for nearly all frequencies considered. It is not clear from the information to date why this is so, although the presence of more modes could explain the increase in turbulence level and reduction in q_a.

As stated, the calculations presented for r = 6cm were also done for other r, including r = 7, 8, and 9cm. The results are shown in Fig. 4.32*a* for low q_a, and 4.32*b* for high q_a. While the low-frequency values

show some deviations with r, $L_p(f)$ is largely independent of r for both q_a, showing no systematic variation with minor radius. A direct consequence of this is that the Δm does vary with radius at f>100 kHz. This is shown in Fig. 4.33*a*&*b*, for both q-cases. At low frequencies, there is little variation in Δm with radius, and this reinforces the statement of these being large-scale oscillations or global modes.

4.2.3. Toroidal and Parallel Displacements

Just as poloidal correlations can be useful in determining the poloidal mode structure of turbulence, toroidal correlations help determine the toroidal mode structure. Further, the strongly toroidal direction of field lines suggests that toroidal displacements may be appropriate for measuring the parallel correlation length L_0. This quantity is a necessary parameter not only for understanding the structure of the turbulence, but also for determining the energy transport rate due to the turbulence.

Toroidal correlation estimates from $|R|_{max}$ for toroidally separated sensors at r = 8cm are shown in Fig. 4.34. Again, $\tau_{max} \neq 0$ in general for this type of sensor displacement. For low q, $|R|_{max}$ falls quickly to a steady level, indicating that the large-scale components of $\tilde{B}_r$ survive all around the machine. The high-q case shows an interesting characteristic in that the decay is oscillatory with separation, rather than a simple exponential decay. If the high-q coherence versus separation is plotted for several frequencies, it becomes clear that the oscillation is present over a broad range of frequencies, and includes a

significant portion of the spectrum above 100 kHz. This behavior is not easily explained. Radial or poloidal mislocation of the sensors within the experimental uncertainties is insufficient to explain the regularity and comparatively large amplitude of the oscillation. Hence, the effect is real, and demands a physical explanation.

One plausible explanation involves the possibility that correlation lengths along the field lines are quite large. Suppose the sensors are all located on a flux surface of q = 9/4. If a particular sensor at r = 8cm is chosen as a reference and assigned the toroidal azimuth $\phi = 0$, with other sensors located at $\phi = \pi/3$ and $\phi = \pi/2$, then the field line crossing $\phi = 0$ passes within 2cm of the sensor at $\phi = \pi/2$, but within no less than 8cm from the one at $\phi = \pi/3$. Since poloidal correlation lengths are short, less than three or four centimeters, a lower value of correlation is expected with the $\phi = \pi/3$ sensor than the one at $\phi = \pi/2$, provided one expects the correlation to be significantly higher along field lines. Likewise, this line passes more closely to a sensor at $\phi = \pi$ than to one at $\phi = \pi/3$, $2\pi/3$, or $5\pi/6$. While this should not be taken as the only possible explanation for the data in question, it certainly invites one to attempt to measure the parallel correlation length, and to find the direction of maximal correlation.

An attempt was made to measure L_0. The determination of the direction in which the maximal correlation exists is left to other experimenters. For the L_0 experiment, probes were placed in the machine so as to be able to trace out a q=1 contour at arbitrary minor

radius. The arrangement is described in Fig. 4.35. At the q=1 surface, it should be possible to align three sensors in the array with a single field line. For $q_a \approx 0.6$ discharges, the q=1 surface oscillates about minor radius $r \approx 6.5$cm, according to Osborne[3]. Sensors were placed, then, at radii bracketing this radial position, namely at r = 5, 6, 7, and 8cm. Discharges with $q_a \approx 0.6$ were fired. The results of $|R|_{max}$ versus separation are shown in Fig. 4.36. Two points are plotted for angular separations of $\pi/2$, depending on the direction of the (reversible) toroidal field. The direction of the toroidal field should have no effect on the coils separated π radians toroidally and poloidally, since the same line will still pass both points. But for sensors separated $\pi/2$ radians poloidally and toroidally, the direction of B_t is of ultimate importance, as a line passing the first sensor will be displaced π radians poloidally from the second sensor if B_t is reversed. Figure 4.36 shows that the correlation is reduced to the minimal level when the toroidal field is reversed, and the correlation is strong for forward B_t. Hence the correlation is enhanced when coils are displaced parallel to the net field. If a simple exponential curve fit is applied to these data, the parallel correlation length is estimated at $L_0 \approx 150 \pm 10$ cm, approximately one-half of the toroidal circumference of Tokapole II

Due to the ensemble-averaging process used to determine the parallel correlation length, one may regard the result of 150 cm as a lower limit. It is not known what the true direction of maximal correlation within the machine is, or if this will correspond to the

direction of the net field. However, the inclusion of terms in the ensemble for which the field direction may vary from the contour traced by the coils considered above should likely be the strongest factor in L_0.

The lack of detailed profile information on current density makes unreliable the use of a field line tracing code to map the path of a specific line. Other experimenters are continuing to look for helical correlations at present,[4] but have not as yet found a number for L_0 which is in significant disagreement with the one found here.

4.2.4. *Correlations with* $\tilde{n}$ *and* $\tilde{\phi}$.

As described in Chapter 3, a probe was constructed which could simultaneously measure fluctuations in ion saturation current or floating potiential and the radial magnetic field at almost exactly the same location. Hence some measure of the correlations of density and potential fluctuations could be obtained. The fluctuations in J_{sat} are taken to be a reasonable measure of $\tilde{n}$, and $\tilde{\phi}_f$ is taken to be a useful indicator of plasma potential fluctuations, despite the likely strong influence of temperature fluctuations.

The power spectra of $\tilde{n}$ and $\tilde{\phi}_f$ have been measured over the 0-300 kHz frequency range. Typical internal power spectra (r=8cm) are shown in Fig. 4.37 for $q_a \approx 2.3$, with an example of $\tilde{B}_r(f)$ at the same radius for comparison. The spectra of the electrostatic turbulence are similar to each other and to the magnetic spectrum at high frequency, showing the same power-law decay.

Measurements of $<\tilde{J}_{sat}\,\tilde{B}_r>$ and $<\tilde{\phi}_f\,\tilde{B}_r>$ were made at $q_a \approx 0.6$ and at $q_a \approx 2.3$. The results were similar for the two q_a. The correlation coefficients $|R|_{max}$ for various minor radii is shown for both q_a-cases in Fig. 4.38. The correlation is weak at all locations measured, although it is slightly stronger within the separatrix than in the edge. (The local β increases with decreasing r, and the increase in cross-correlation inside the separatrix might concur with theoretical predictions, e.g. the result of Waltz[2] for electromagnetic drift waves.) The coherence versus frequency for $0 \le f \le 300$ kHz is shown in Fig. 4.39, for both values of q_a, both inside and outside the separatrix. The internal coherence in particular is rather steady at 25% across the spectrum. Thus the correlation between $\tilde{n}$ and $\tilde{B}_r$ is small but statistically significant, and is independent of current, net magnetic field strength, and $\tilde{B}_r$.

Measurements of $<\tilde{\phi}_f\tilde{B}_r>$ were made for $q_a \approx 0.65$ and 2.3. The radial profiles of are shown in Fig. 4.40. For low q, the radial profile is peaked slightly just outside the separatrix (r = 9-10cm), and becomes insignificant nearer the center and nearer the outer wall. For the high-q case, there is no consistent behavior with minor radius. This may be due to a lack of statistically-stationary data, particularly from the edge. Coherences within the separatrix are shown in Fig. 4.41, as well as the coherences for points just outside the separatrix. At both q_a's, the high frequency (>150 kHz) turbulence is more correlated in the near edge than in the center. The relatively large correlation measured inside the separatrix at high-q is due to turbulence at frequencies less than 150 kHz.

At any rate, some non-zero correlation may exist between magnetic and potential fluctuations, but, as for density turbulence, the correlation is small.

Because the correlation with electrostatic fluctuations is only slight, the correlations in the radial magnetic turbulence are distinct from those of the electrostatic turbulence, whose characteristics are more readily determined by the existing theory than those of $\tilde{B}_r$. Thus, the character of electrostatic turbulence remains almost completely undetermined by the magnetic measurements presented here, and other experimenters must (and indeed already have begun to[5]) measure the electrostatic turbulence and its correlations in Tokapole II. With a high correlation between electrostatic and magnetic measurements, it would have been possible to compare the correlation results of the magnetics directly to the expectations of existing theory for turbulence in density and potential, but this cannot be done.

4.2.5. *Correlations between components of* $\tilde{B}$

In Fig. 4.14, the spectra for radial, poloidal and toroidal components of the fluctuating magnetic field were shown for discharges of $q_a \approx 0.6$ at $r = 4.5$cm. All three components were found to have very similar frequency structure. It was stated that this could mean that they all are caused by the same instabilities. In that vein, a reasonable issue to address is whether or not they are correlated to one another. Fig. 4.42 shows the cross-coherences between fluctuations in (a) the radial and

poloidal field, (b) the radial and toroidal field, and (c) the poloidal and toroidal field. The coherence for $f \geq 100$ kHz is almost always weak ($\gamma \leq 0.3$), implying that the localized turbulence sources for the three components are distinct. If the same instabilities produces all three ($\tilde{B}_r$, $\tilde{B}_p$, and $\tilde{B}_t$), then the sources of the turbulence for each component must be in different locations, and the sources are separated by at least some significant fraction of the local coherence length.

4.3. Mode structure estimates

The short poloidal coherence lengths found for most of the high-frequency turbulence make it impossible to determine its absolute poloidal mode structure, particularly with regard to asymmetries. But the m-numbers are high, usually on the order of 10 or more for microturbulence,[6,7] and an estimate of m, including trends with amplitude and frequency, is likely to be helpful to development of theory. In Tokapole II, the q_a-scan may well be expected to affect the mode structure, since q_a is an important factor controlling resonances within the plasma.

Attempts were made to determine the poloidal mode numbers making various symmetry assumptions, from both phase shifts for poloidally separated sensors and radial amplitude decay measurements outside the divertor separatrix. A comparison of the two methods will then be some measure of the accuracy of edge radial amplitude decay

measurements, which are the only measurements of microturbulent m's made in several tokamaks.[8,9]

4.3.1. *Poloidal phase shifts*

To determine the mode structure from poloidal phase shifts requires that the average phase varies systematically with frequency. (Random phase values correspond to zero significant coherence in the given frequency range.) Phase shifts for sensors separated 2cm poloidally are shown for discharges of different q_a in Fig. 4.43. The actual values of the phase shifts may be imperfect because of misalignment of the coils from the radial direction due to the irregular shape of the flux surfaces. The phase velocity for the turbulence can be calculated according to $v_p = s\,\omega/\theta$, where s is the coil separation. The phase velocities calculated are shown in Fig. 4.44, and, for both values of q_a, these phase velocities are in the electron diamagnetic drift direction. It is assumed that the sensors are within one low-frequency wavelength of each other. If the modes are also poloidally symmetric, the m-numbers from the phase shifts are as given in Fig. 4.45. This is simply the result of fitting m wavelengths of the oscillations to the circumference of a circle of radius 6cm. Poloidal mode numbers from phase shifts (m_{ps})are higher at low q_a.

Poloidal mode numbers so determined at r = 9cm for three values of q_a are shown in Fig. 4.46. The poloidal mode numbers decrease with increasing q_a. The actual values are found to be around ten for the microturbulent modes ($f \geq 150$ kHz), and may be considerably higher for

oscillations with $f > 500$ kHz. Comparing these values of m to those of Δm in Fig. 4.31, it is seen that $\Delta m \sim m$.

An interesting issue in determining the types of modes present is the variation of poloidal mode numbers with minor radius. This is shown for low q_a in Fig. 4.47, and for high q_a in Fig. 4.48. In both cases, there is little significant variation in m_{ps} with minor radius. (Recall that there *is* some variation in Δm with radius, as discussed in § 4.2.2.) This result suggests that the magnetic microturbulence is related to the macroscopic coherent structure.

4.3.2. Radial amplitude decay

For some large tokamaks,[8,9] the only measurements made of mode structure for magnetic turbulence in large tokamaks are faint attempts to represent the dominant poloidal mode numbers m by observing what is presumed to be vacuum field decay in the edge regions of the machine. This is usually done using poloidal field coils mounted on the walls of non-circular poloidal cross section vacuum vessels. These coils are thus at varying distances from the nominal center of the discharge, and hence the amplitude spectra can be compared, and a radial amplitude decay profile can be established, as a total amplitude decay or as a function of frequency. In the machines cited above, the correlation between even adjacent coils is very small, because the coils are separated farther than the poloidal coherence lengths. The measurement, then, is always questionable.

In Tokapole II, a multiple-coil radial array has been used to measure the edge field decay for several q-cases. These coils are highly correlated for the cases of $q_a < 2.8$ (§ 4.2.1), and only those (two) cases will be considered. The radial amplitude decay curves for several frequencies at two values of q_a are shown in Fig. 4.49. The higher frequencies show more rapid decay, and hence will be associated with higher m_{rd}. Fig. 4.50 shows the values of m_{rd} calculated as described in § 3.3 by fitting to curves of $r^{-(m+1)}$ for each frequency. The same observation is made as with phase shifts, that the low q_a displays higher poloidal mode numbers. However, there are not enough cases of q_a available with this data to make any determination of a continuing trend of decreasing m_{rd} with increasing q_a.

4.3.3. Legitimacy of edge decay measurements

It has already been determined that radial amplitude decay measurements cannot be made for discharges of $q_a \geq 3$ in Tokapole II, because of the short edge radial coherence lengths, and nonmonotonic edge radial amplitude profiles in these discharges. On the other hand, for the two cases in which m_{rd} was determined above, the edge amplitude decay is vacuum-like, and the correlation is high.

Fewer symmetry assumptions are made in the determination of m_{ps} than for m_{rd}, so one may consider the direct internal phase measurements to be the more reliable determination of m, and hence, the best available standard by which radial decay measurements may be judged. A comparison of values for the same or nearly the same q_a is

shown in Fig. 4.51. In general, the values of m_{rd} are somewhat but not greatly higher than those of m_{ps}. The trends in the data with frequency are similar. Therefore, the use of radial amplitude decay measurements has some foundation, and is to a limited degree useful for estimating the mode structure of short-scale-length turbulence.

REFERENCES

[1]A.B. Rechester and M.N. Rosenbluth, Phys. Rev. Lett. **40**, 38 (1978).

[2]R.E. Waltz, Phys. Fluids **28**, 577 (1985).

[3]T.H. Osborne, Ph.D. Thesis, *Disruptive Instabilities in a Poloidal Divertor Tokamak*, University of Wisconsin-Madison (1984) p. 176.

[4]M.A. LaPointe, R.N. Dexter, E.J. Haines, and S.C. Prager, Bull. Am. Phys. Soc. **33**, 2020 (1988).

[5]I.H. Tan, R.N. Dexter, S.C. Prager, and T.D. Rempel, Bull. Am. Phys. Soc. **33**, 2020 (1988).

[6]Ch.P. Ritz, R.D. Bengtson, K.W. Gentle, K.W. Gentle, Y.J. Kim, P.E. Phillips, T.L. Rhodes, and A.J. Wooton, Bull. Am. Phys. Soc. **32**, 1842 (1987).

[7]S.J. Zweben, C.R. Menyuk, and R.J. Taylor, Phys. Rev. Lett. **42**, 1270 (1979).

[8]N. Ohyabu, G.L. Jahns, R.D. Stambaugh, and E.J. Strait, Phys. Rev. Lett. **58**, 120 (1987).

[9]S.J. Zweben, D. Manos, R.V. Budny, P. Efthimion, E. Fredrickson, H. Greenside, K.W. Hill, S. Hiroe, S. Kilpatrick, K. McGuire, S.S. Medley, H.K. Park, A.T. Ramsey, and J. Wilgen, J. Nucl. Mater. **145-147**, 250 (1987).

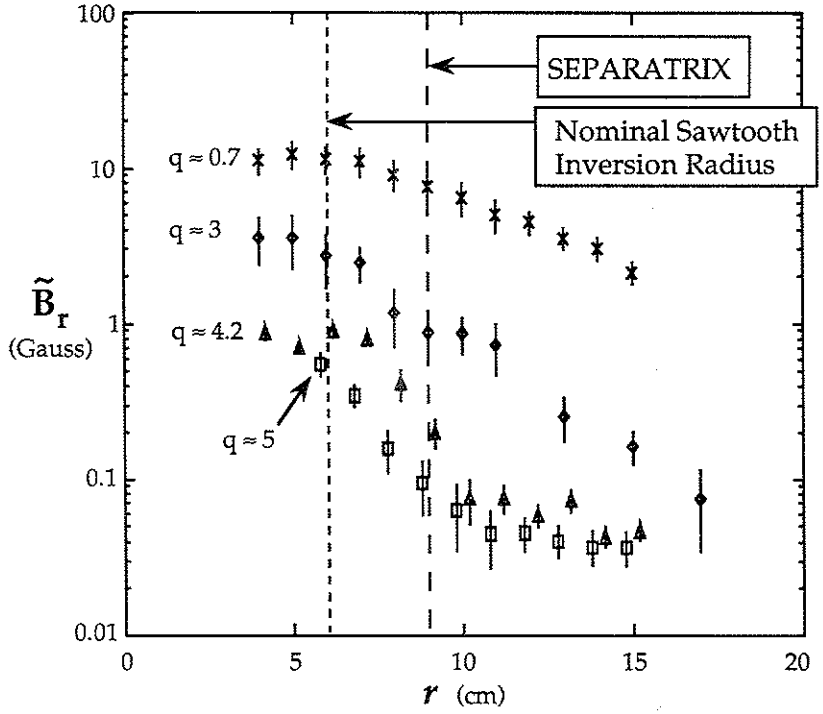

FIG. 4.1. Radial profiles of magnetic turbulence amplitude for $f \approx 10 - 400$kHz for several edge q. Error bars are from statistical scatter in the power spectra.

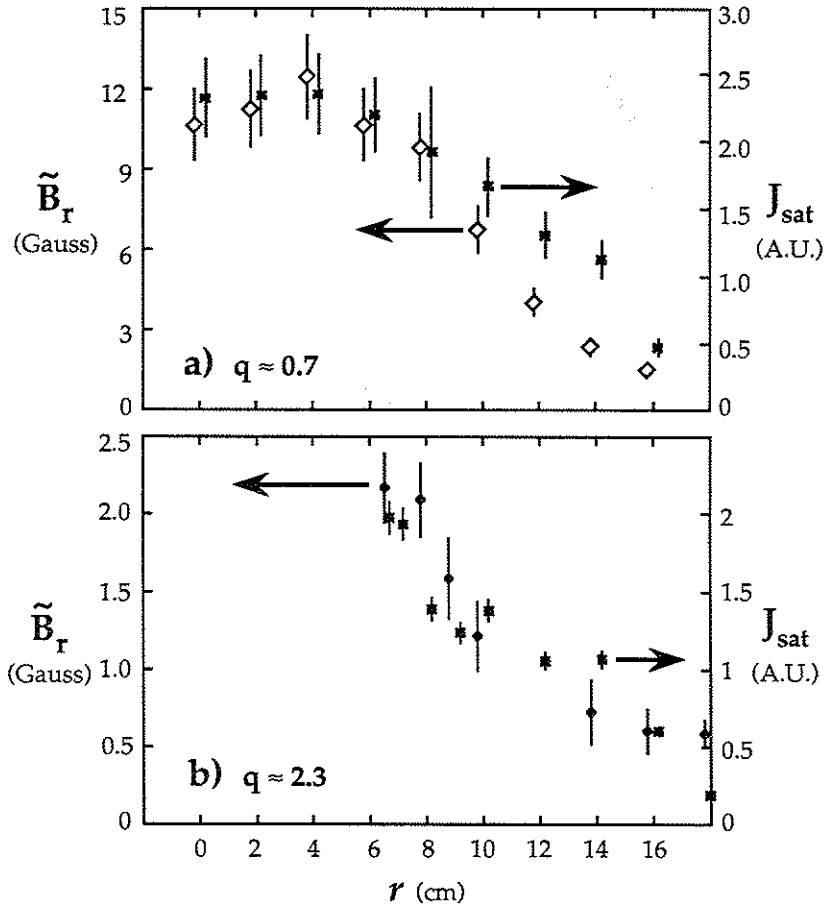

FIG. 4.2. Radial profiles of turbulence amplitude compared to that of the equilibrium ion saturation current for (a) edge q ≈ 0.7 and (b) edge q ≈ 2.3. Error bars are from the statistical scatter in the data.

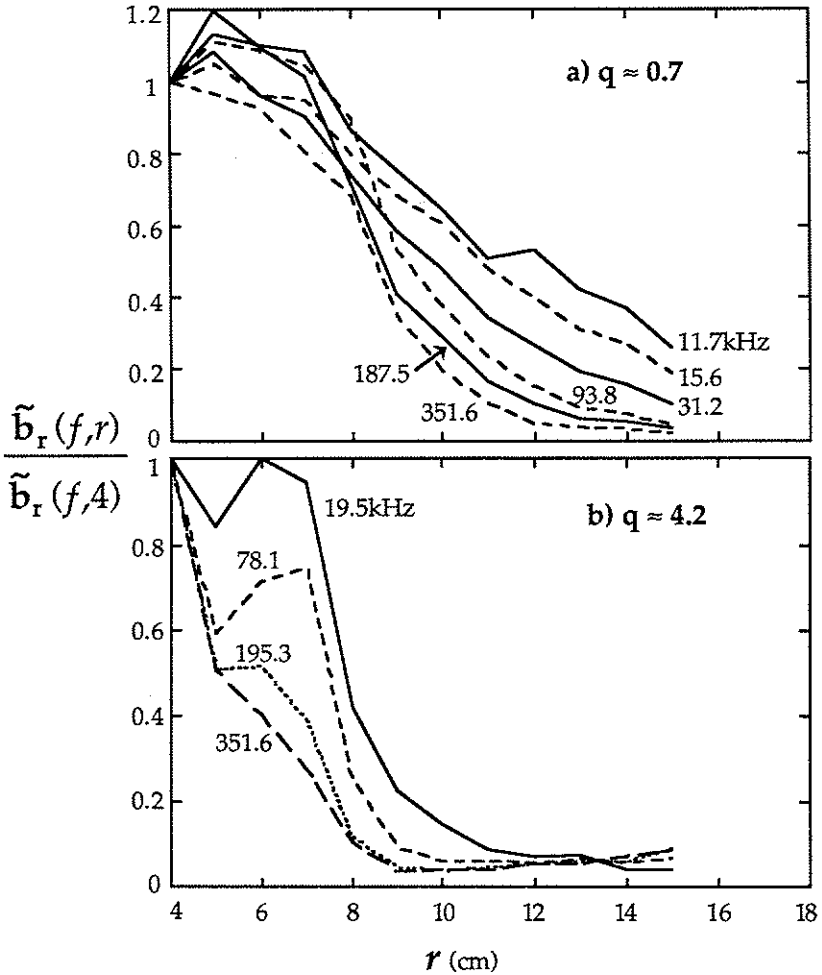

FIG. 4.3. Radial profiles of turbulence amplitude at specific frequencies normalized to the amplitude at r = 4cm for (a) $q_a \approx 0.7$ and (b) $q_a \approx 4.2$.

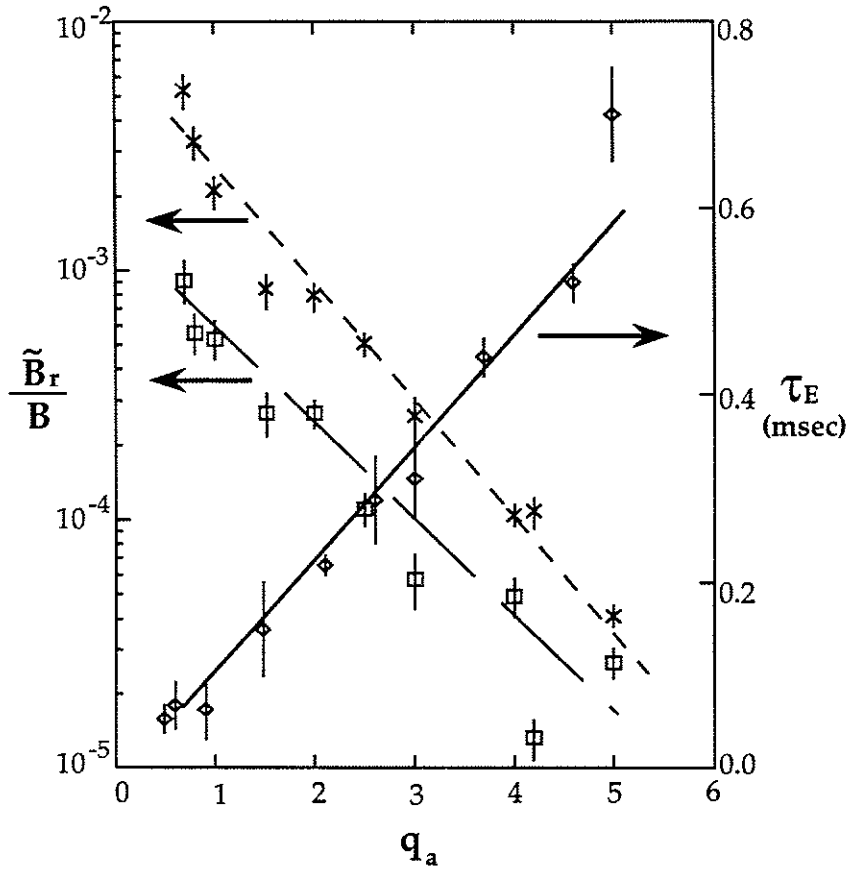

FIG. 4.4. The q -scaling of magnetic turbulence amplitude at r = 8cm and energy confinement time. Fluctuations are normalized to the total field. Turbulence data are included for f = 10-400kHz (✱) and for f = 100-400kHz (⊞).

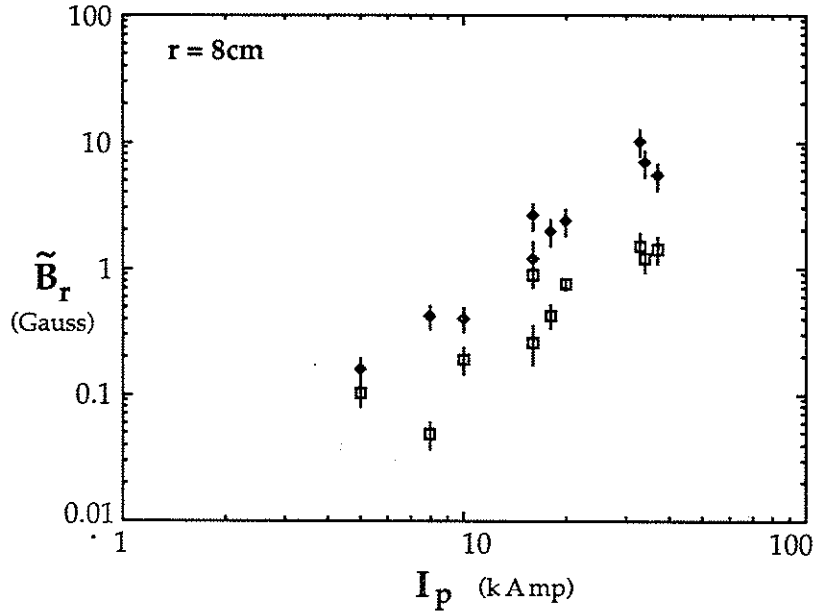

FIG. 4.5. Scaling of $\tilde{B}_r$ (r = 8cm) with plasma current, disregarding variations in the toroidal field. The slope of the data gives $\tilde{B}_r \sim I_p^{3/2}$ for both frequency ranges.

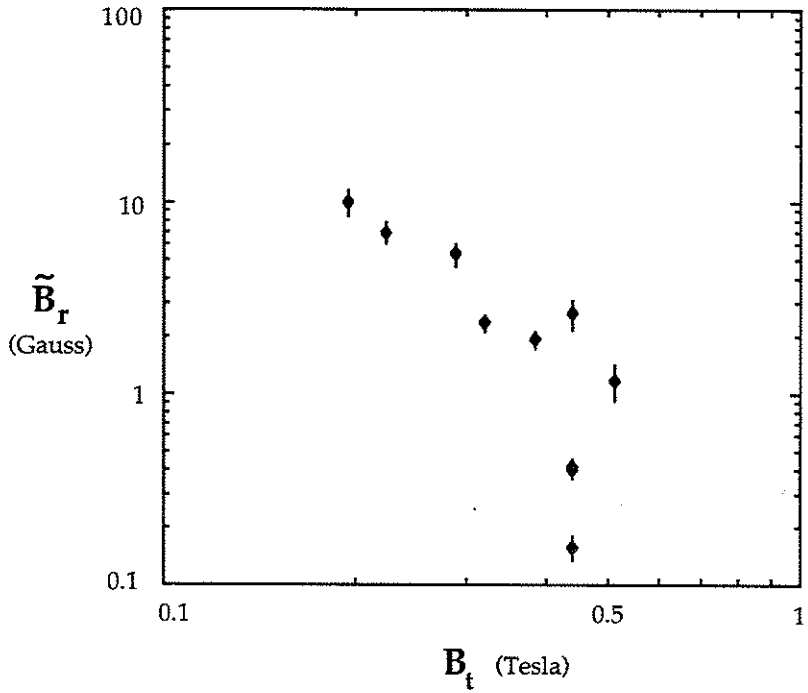

FIG. 4.6. Scaling of $\tilde{B}_r$ (r = 8cm) with toroidal field disregarding current variations. Data are for f = 10 - 100kHz.

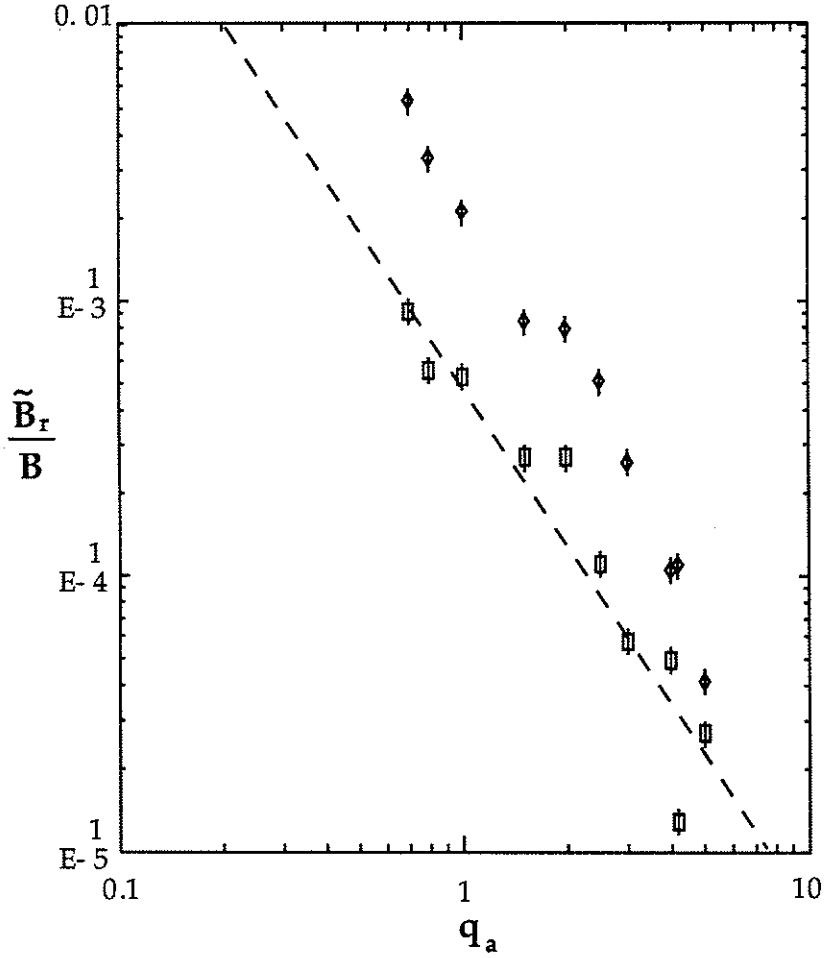

FIG. 4.7. Edge-safety-factor-scaling of magnetic fluctuations normalized to the total field at r = 8cm. Magnetic turbulence data are shown for f = 10 - 100kHz (♦), and for f = 100 - 400kHz (⧫).

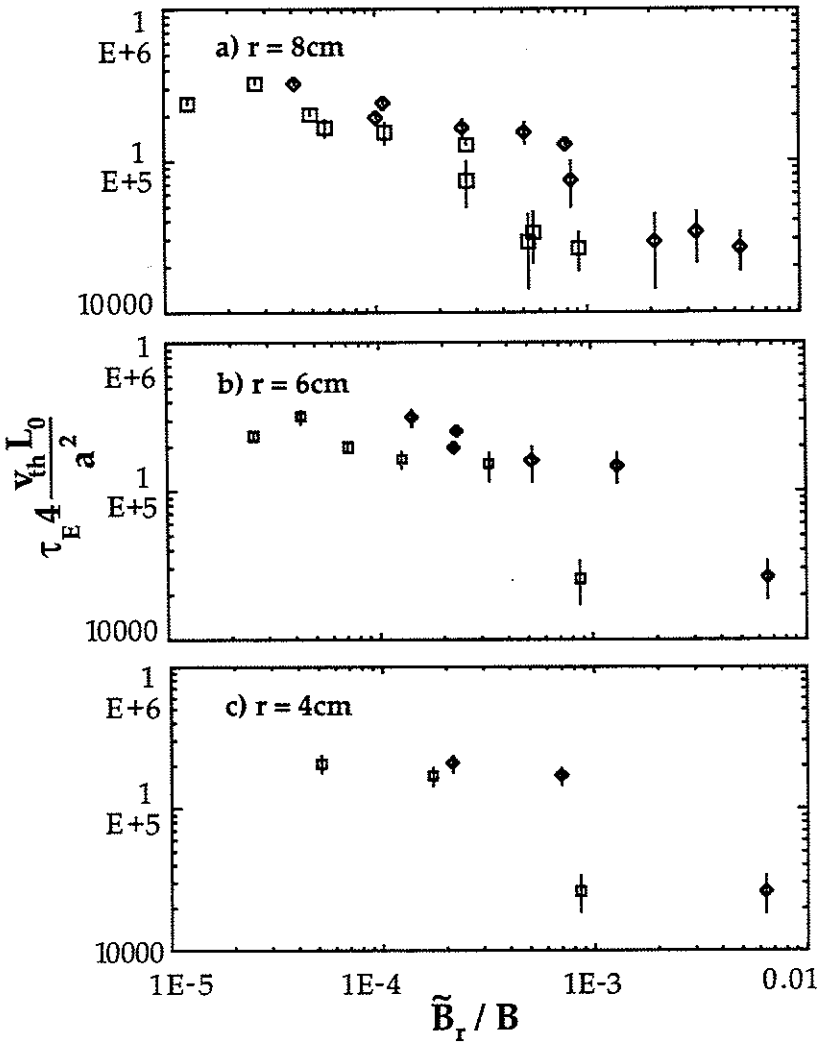

FIG. 4.8. Variation in confinement with the normalized turbulence level. Confinement degrades rapidly once turbulence reaches the 10^{-4} level in the 100-400kHz range. Data are for a) r = 8cm, b) r = 6cm, and c) r = 4cm.

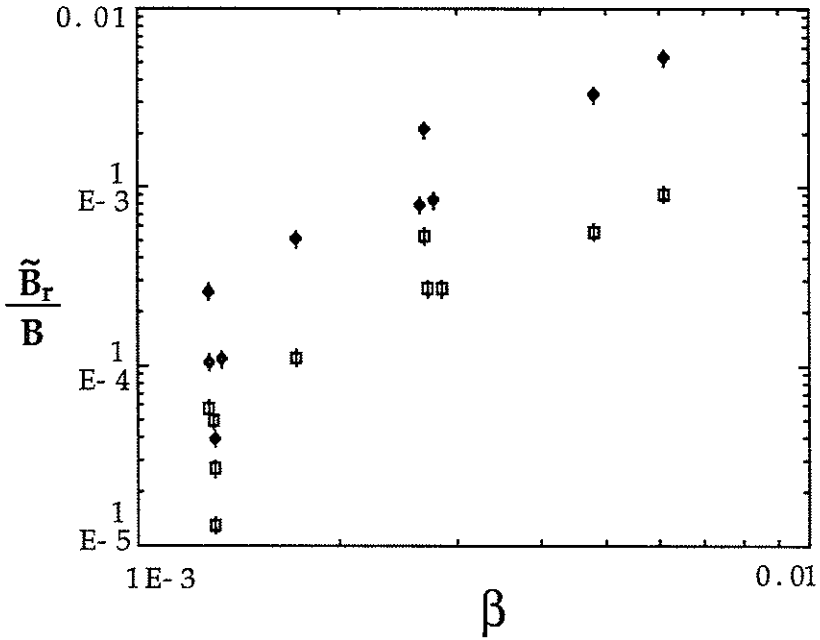

FIG. 4.9. Scaling of turbulence amplitude (r = 8cm) with total beta. Sufficient β may have an effect on the turbulence amplitude.

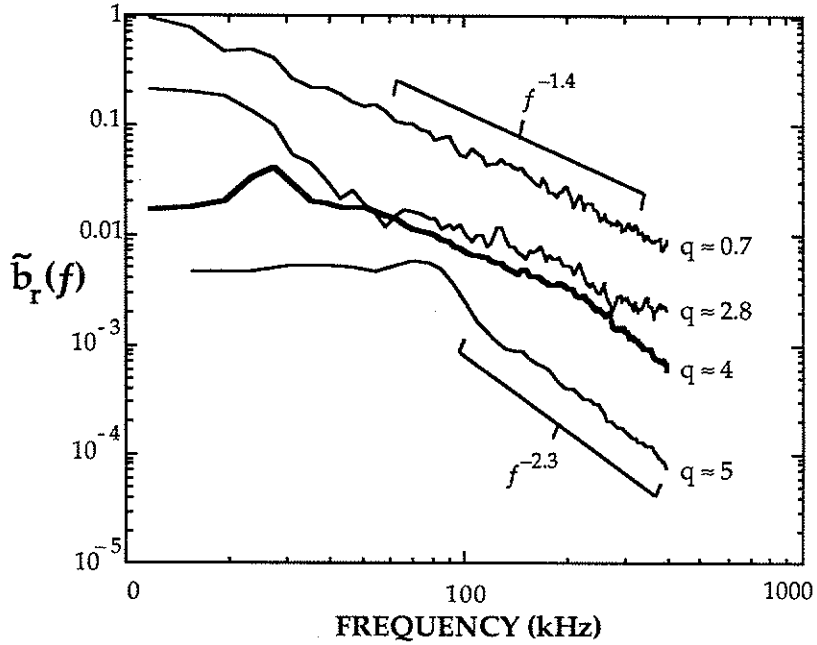

FIG. 4.10. Amplitude spectra in Gauss/$\sqrt{\text{kHz}}$ at several q_a for r = 8cm, showing the power-law decay at high frequency.

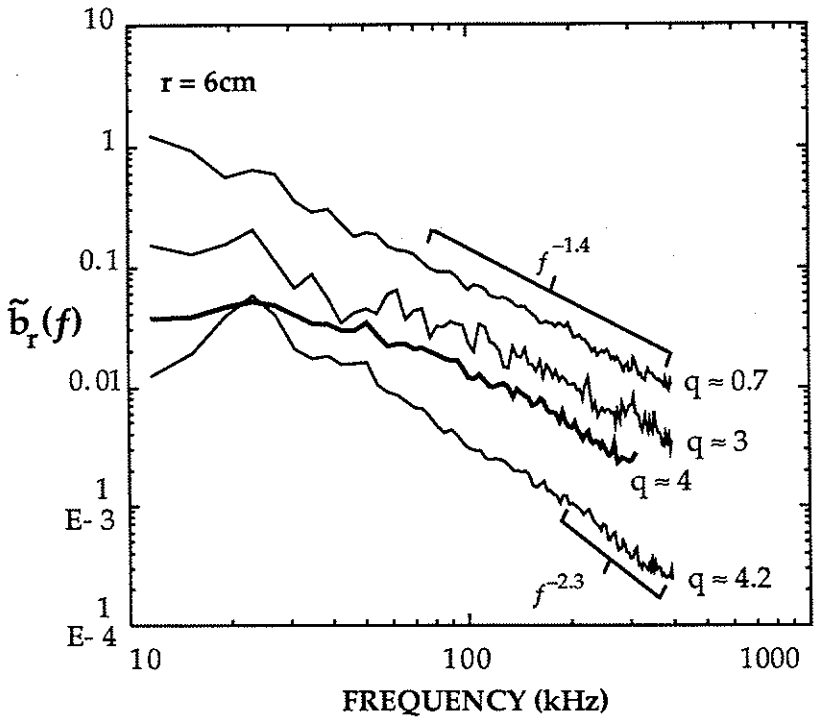

FIG. 4.11. Amplitude spectra in Gauss/$\sqrt{\text{kHz}}$ at r = 6cm for various q. This is the nominal sawtooth inversion radius for $q_a \leq 2$.

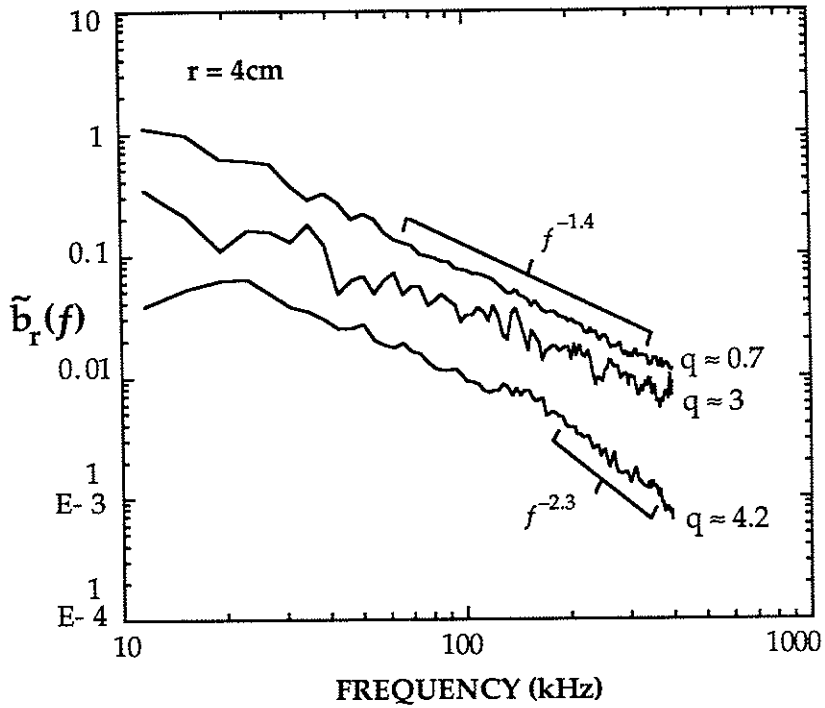

FIG. 4.12. Amplitude spectra at r = 4cm, inside the sawtooth inversion radius for all edge q, showing the same power-law decay at high frequency as data at r = 6 and 8cm.

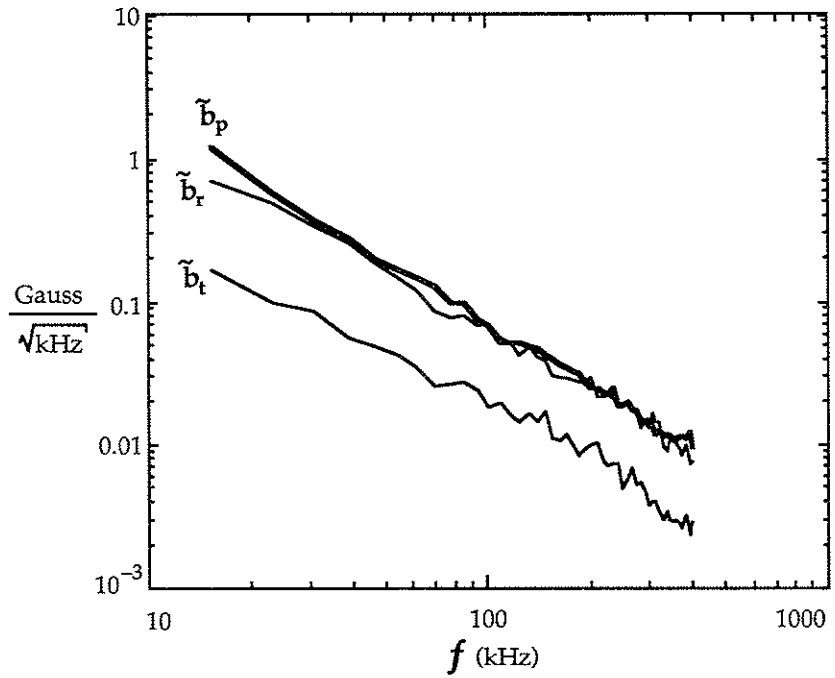

FIG. 4.13. Low q magnetic amplitude spectra for poloidal, radial and toroidal components at r = 4.5cm. All three spectra are very similar, suggesting that they may all be related to the same instabilities.

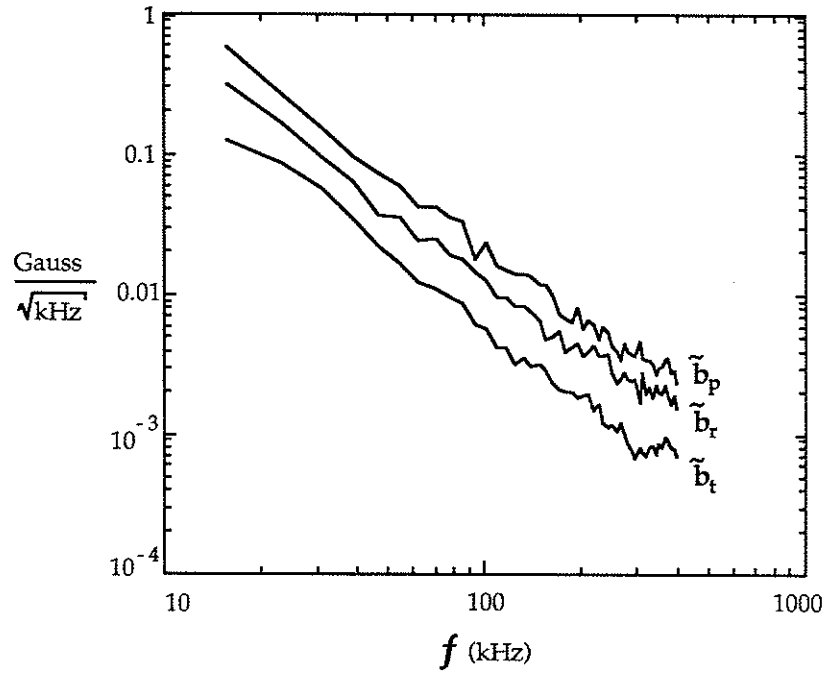

FIG. 4.14. Magnetic turbulence amplitude spectra for edge q ≈ 0.6 outside the separatrix (r = 11.7cm), for all three components of the field. As in Fig. 4.13, all spectra show the same structure.

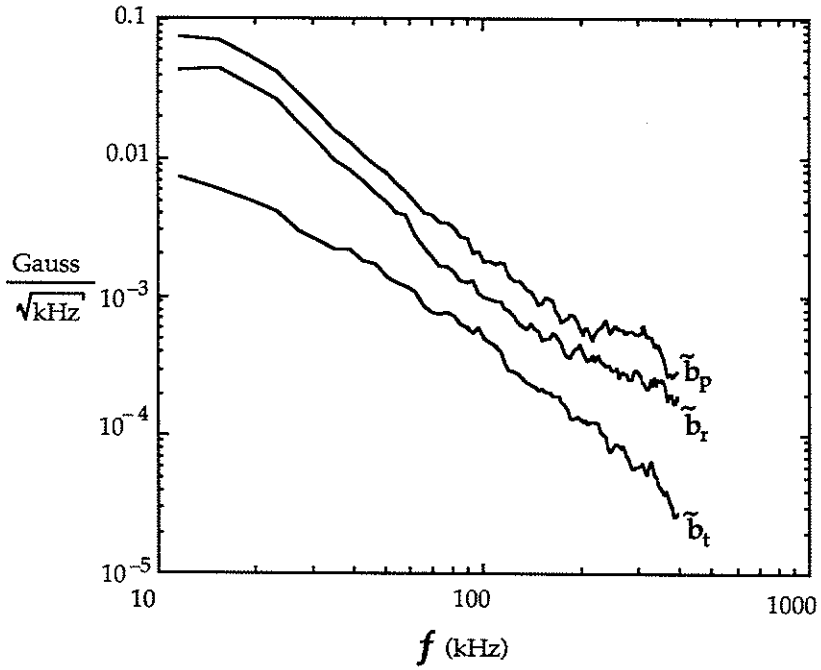

FIG. 4.15. Amplitude spectra of the three components of $\tilde{B}$ outside the separatrix (r = 11.7cm) for edge q ≈ 2.5. The spectra are all similar, as with low q.

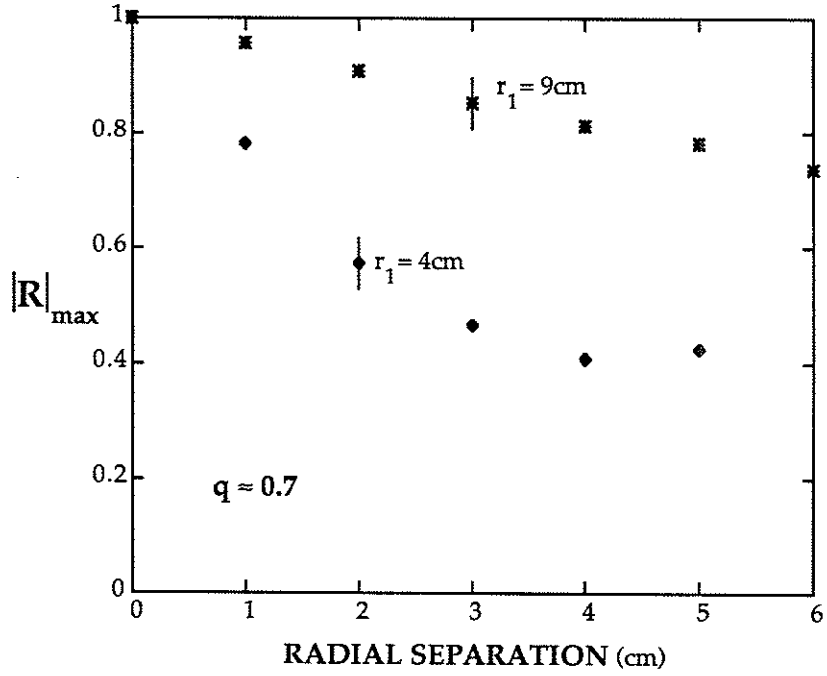

FIG. 4.16. Radial decay of the absolute maximum of the correlation function for signals of radially-separated sensors at edge $q \approx 0.7$. The diamonds represent separations within the separatrix. The asterisks represent separations outside the separatrix. The data were taken with multiple-coil probes, and the innermost coil is used as a reference in each case. For the internal case, the innermost coil was located at r = 4cm. For the external case, the innermost coil was at r = 9cm.

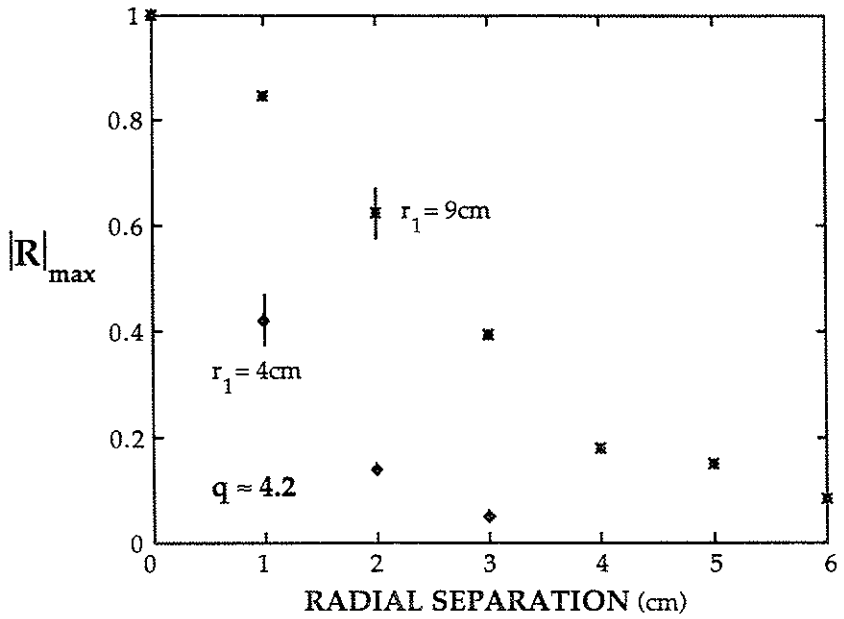

FIG. 4.17. Radial decay of the absolute maximum of the correlation function for signals of radially-separated sensors at edge $q \approx 4.2$. The diamonds represent separations within the separatrix. The asterisks represent separations outside the separatrix. The data were taken with multiple-coil probes, and the innermost coil is used as a reference in each case. For the internal case, the innermost coil was located at $r = 4$cm. For the external case, the innermost coil was at $r = 9$cm.

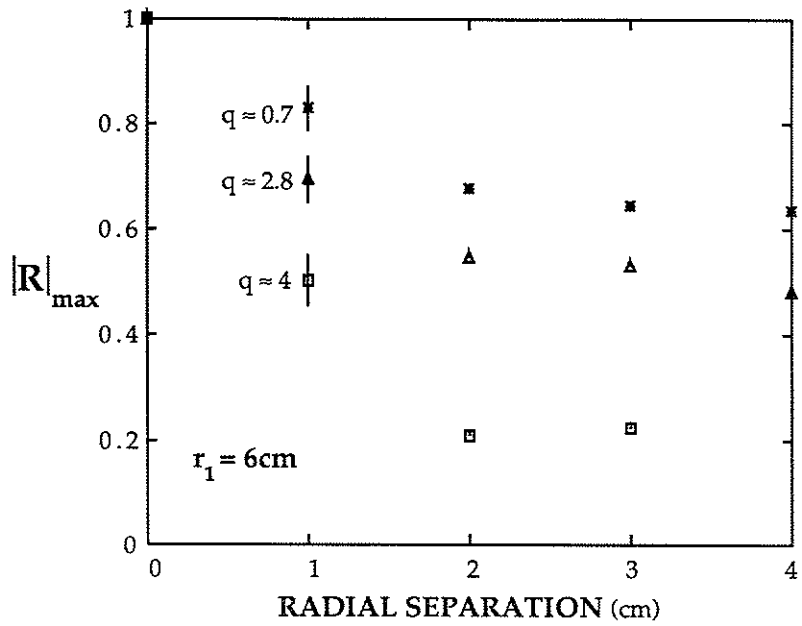

FIG. 4.18. Radial correlation decay from $r = 6$cm outward for low q, intermediate q, and high q. Long scale-length effects diminish toward higher q.

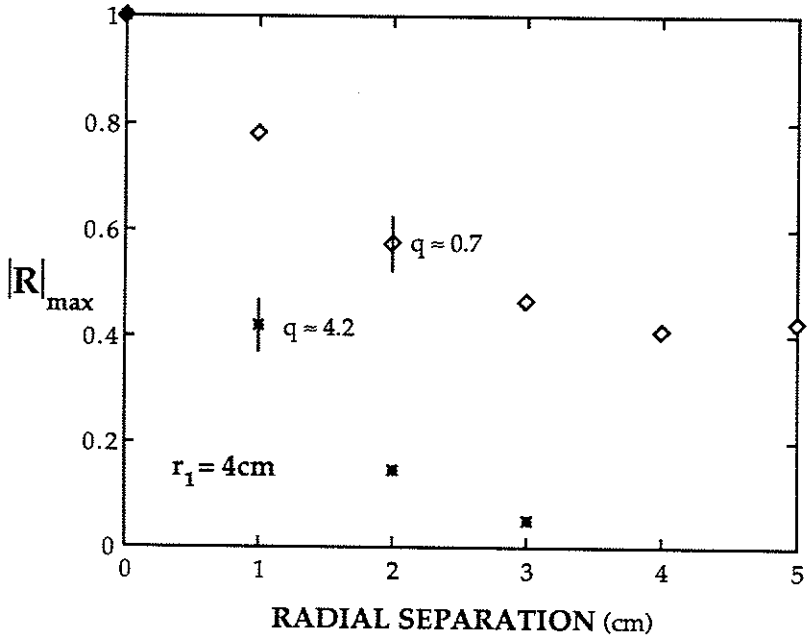

FIG. 4.19. Radial correlation decay for low q and high q from r = 4cm. Again, the high q shows more rapid decay, indicating a decrease in the dominance of large-scale activity at high edge safety factor.

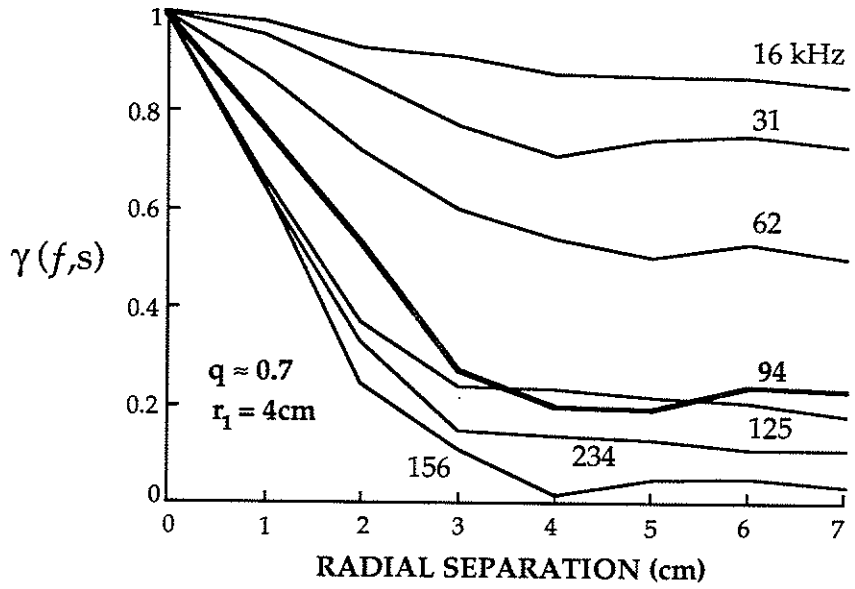

FIG. 4.20. Coherence decay with radial separation for sensors inside the separatrix at low edge q. The innermost coil is the reference coil, located at r = 4cm. Higher frequencies have a steeper coherence decay.

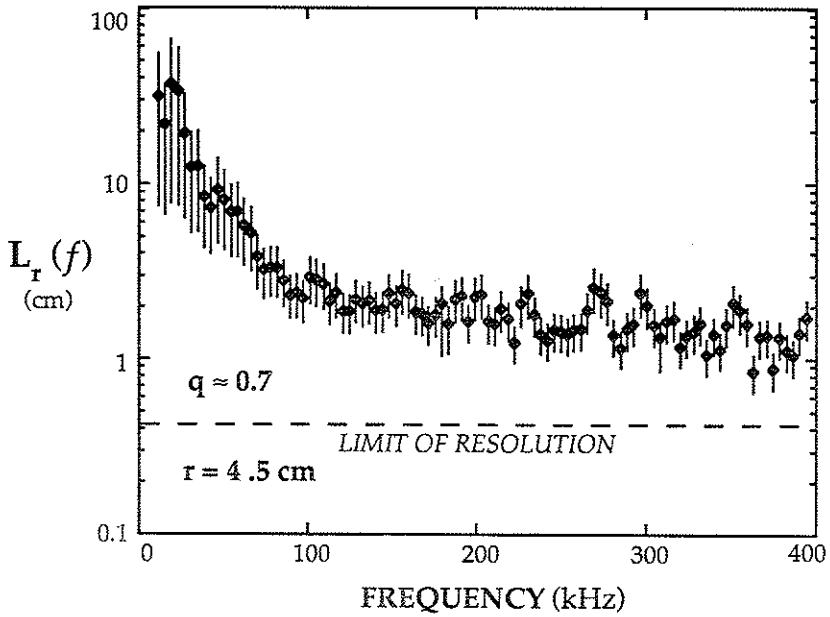

FIG. 4.21. Low q radial coherence lengths calculated from a pair of sensors centered around r = 4.5cm. (One sensor was at r = 4cm, and the other at r = 5cm.) Low-frequency coherence lengths are greater than the minor radius of the plasma.

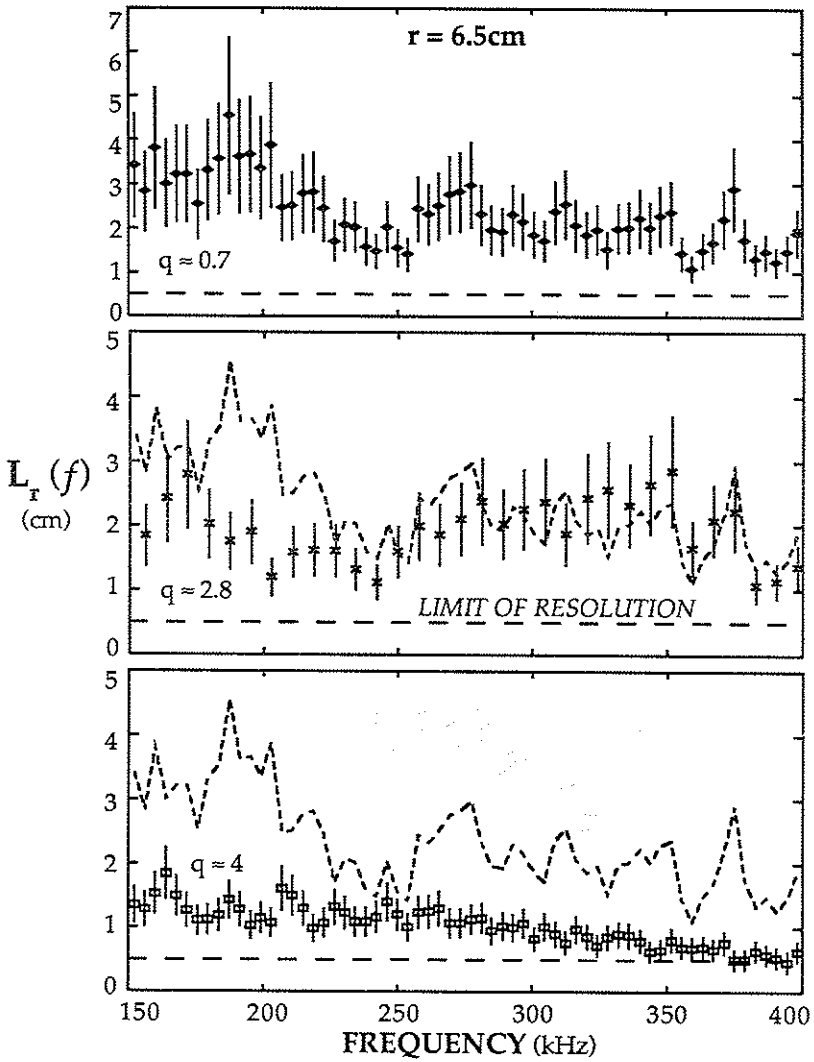

FIG. 4.22. Microturbulent coherence lengths at $r = 6.5$ cm for low, intermediate, and high edge q. The dashed curves in the two lower plots trace the values for $q \approx 0.7$.

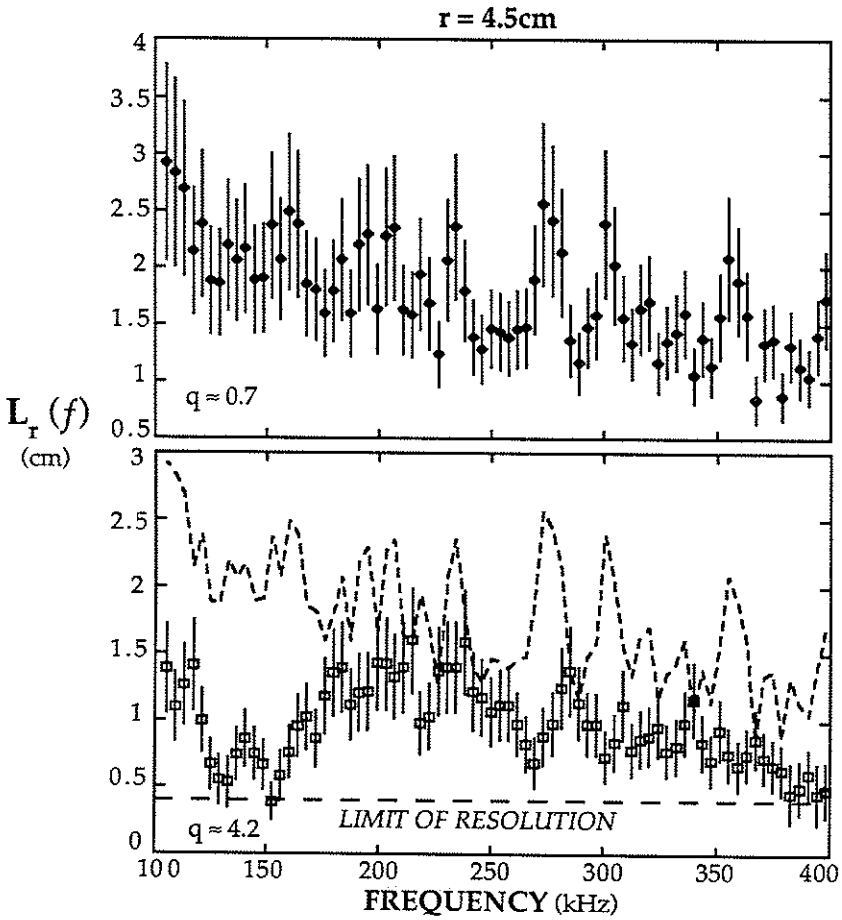

FIG. 4.23. Radial coherence lengths at $r = 4.5$cm for low and high edge safety factor. The dashed line on the lower graph traces the $q \approx 0.7$ values for comparison.

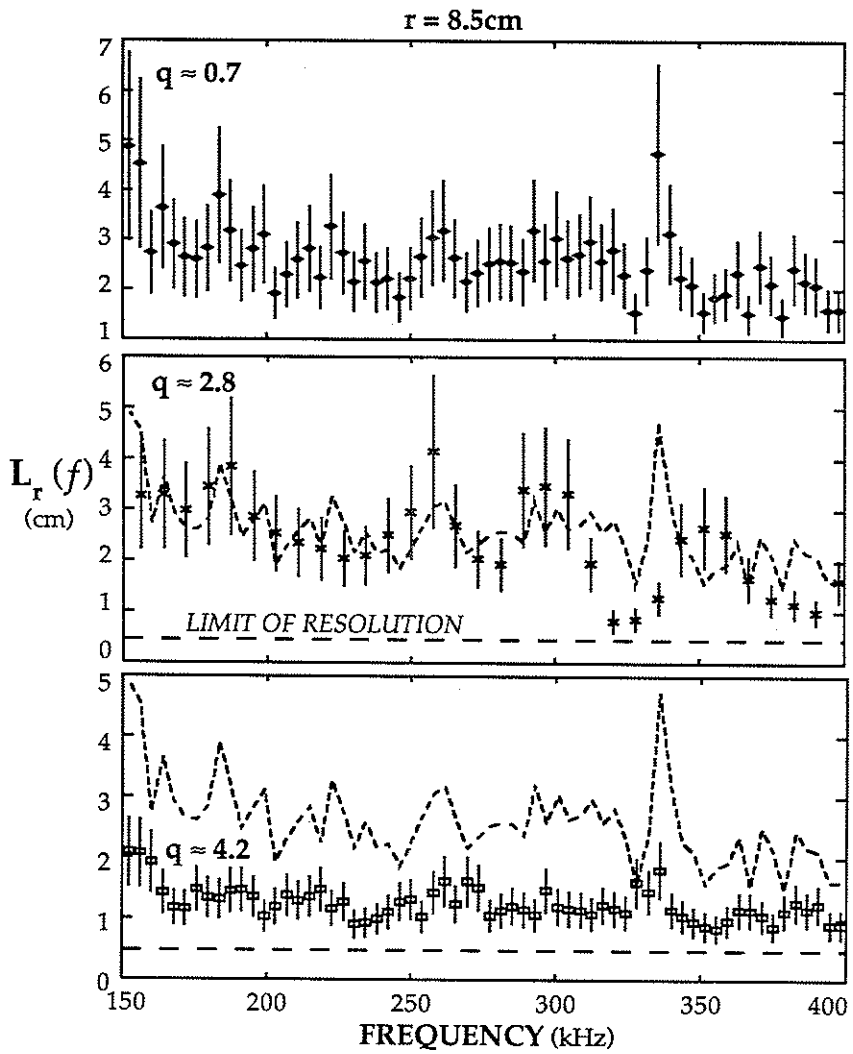

FIG. 4.24. Radial coherence lengths at r = 8.5cm for low, intermediate, and high edge q. The dashed lines on the lower two figures trace the q ≈ 0.7 values for comparison.

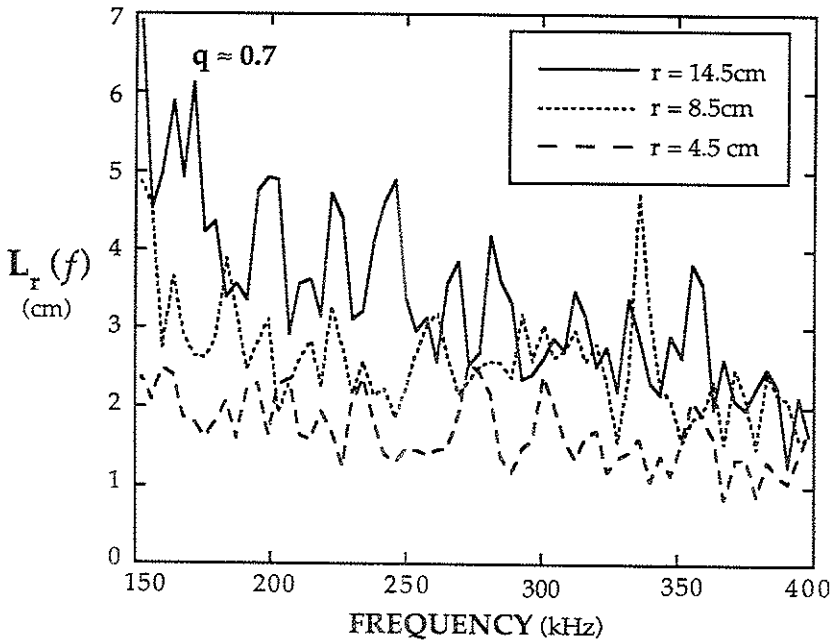

FIG. 4.25. Curves showing the variation of microturbulent radial coherence lengths with minor radius for $q \approx 0.7$.

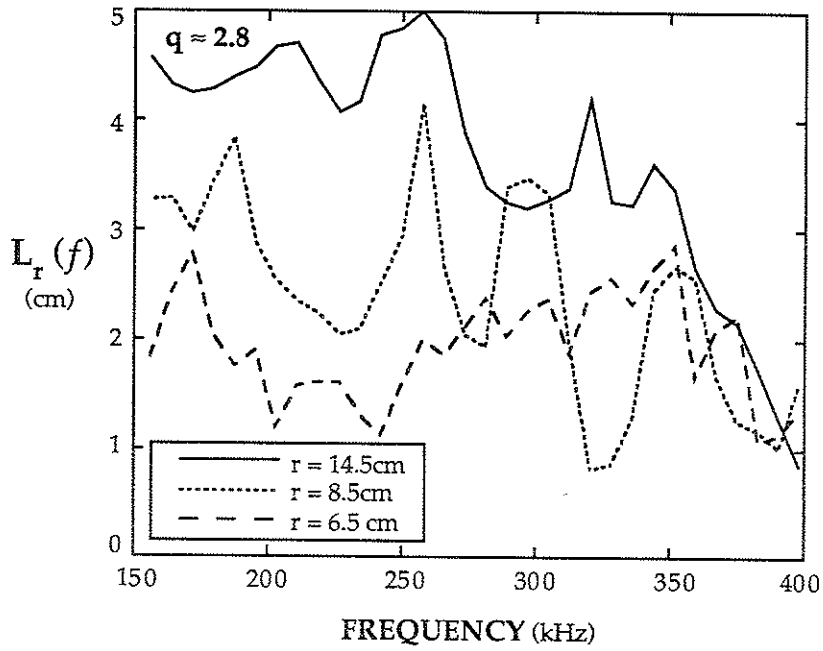

FIG. 4.26. Curves showing the variation in radial coherence length with minor radius at $q \approx 2.8$.

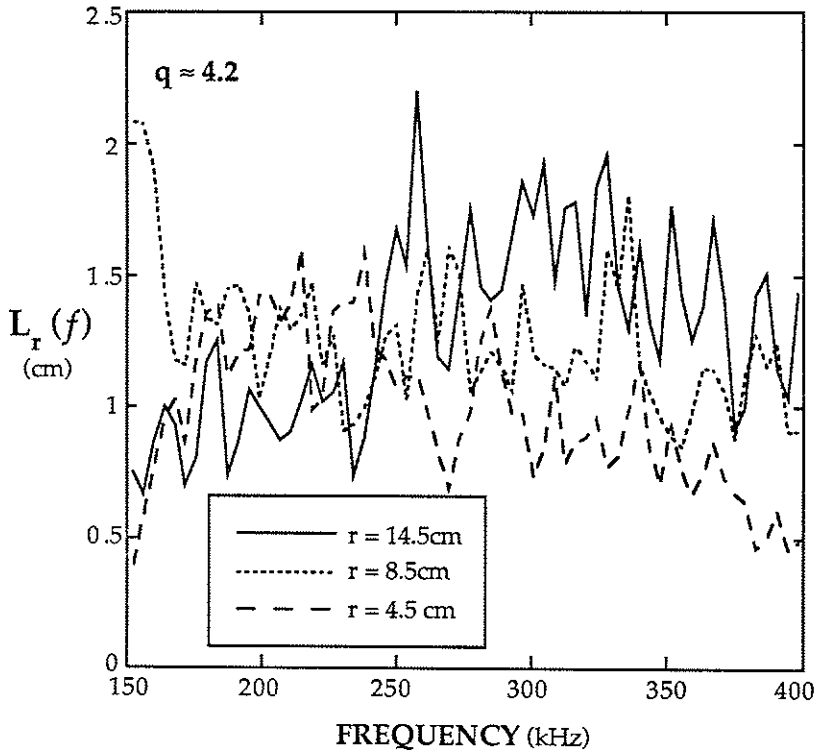

FIG. 4.27. Curves showing the variation of radial coherence lengths with minor radius for $q \approx 4.2$.

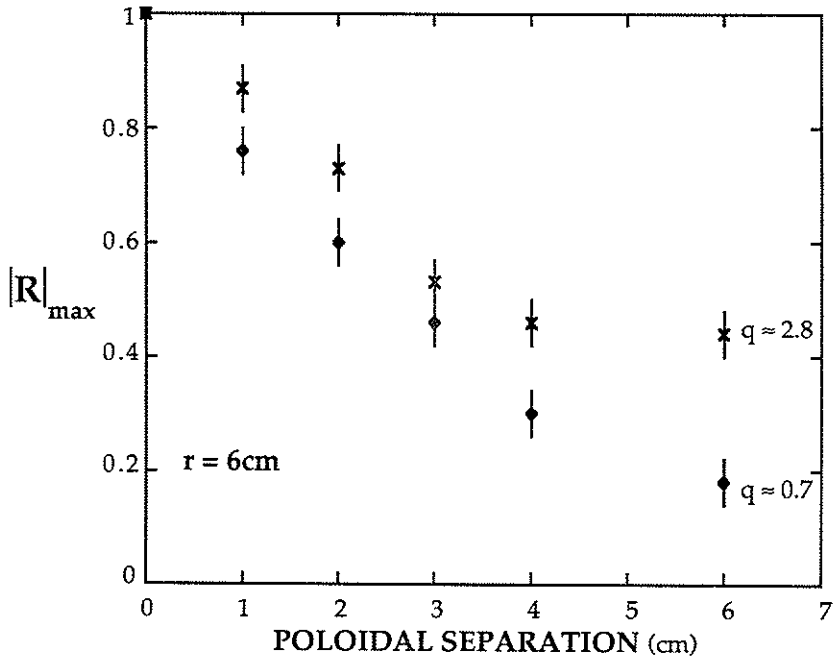

FIG. 4.28. Poloidal correlation decay for $q \approx 0.7$ and 2.8 at $r = 6$cm.

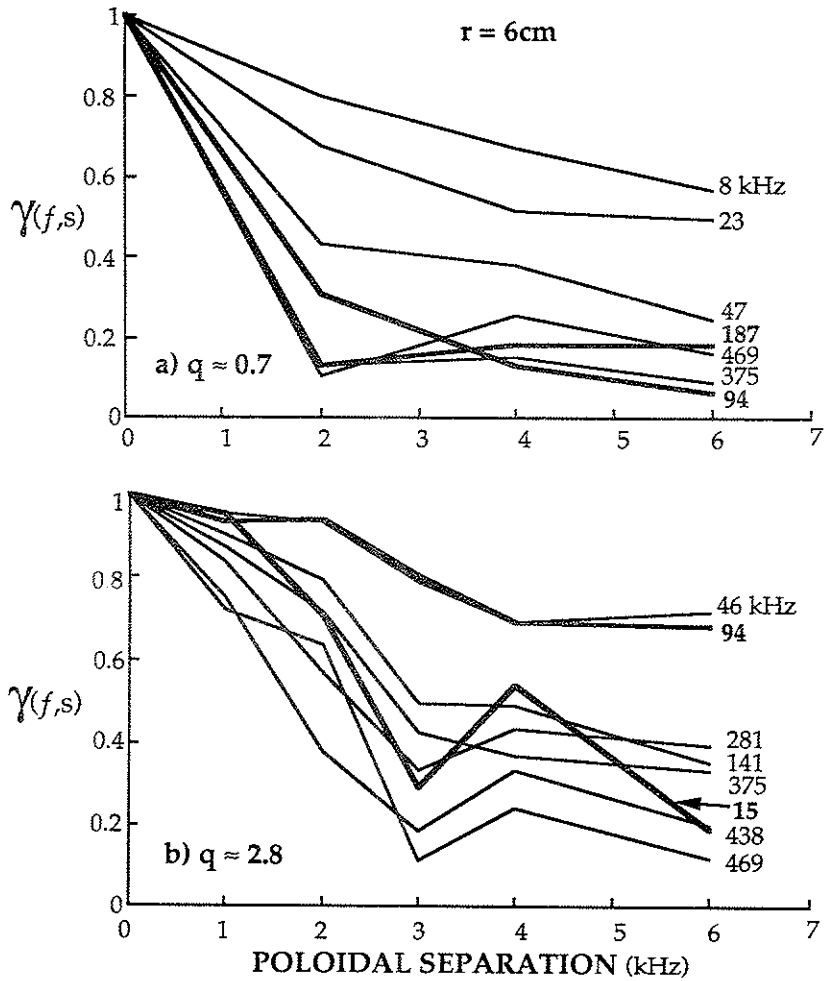

FIG. 4.29. Poloidal coherence decay at r = 6cm for (a) q ≈ 0.7 and (b) q ≈ 2.8, for various frequencies.

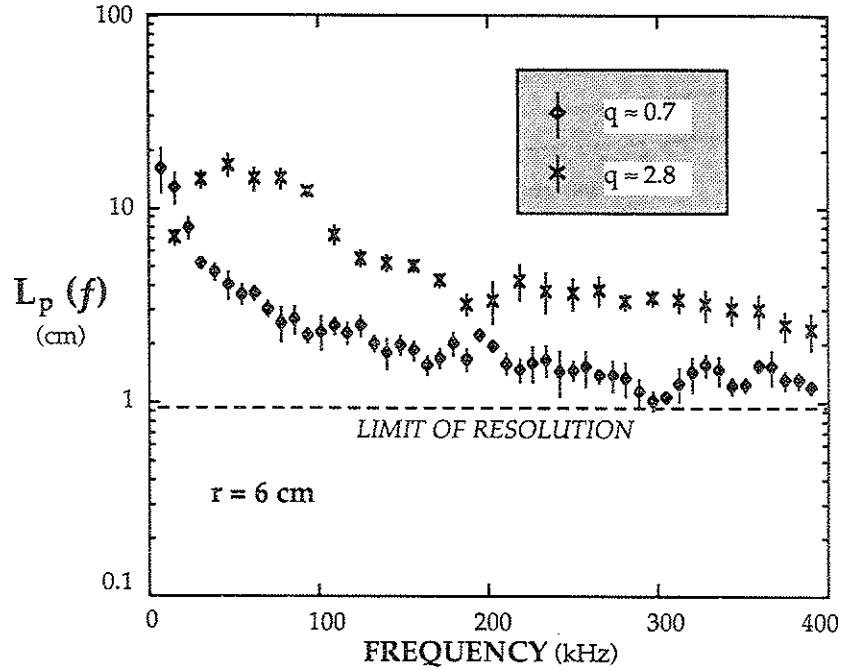

FIG. 4.30. Poloidal coherence lengths at r = 6cm for q ≈ 0.7 and 2.8.

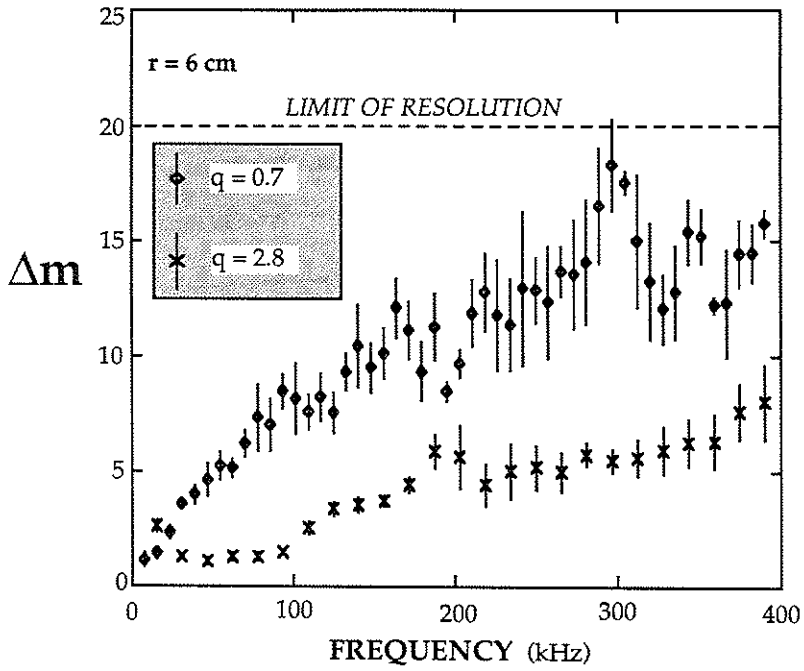

FIG. 4.31. Spread in poloidal mode number from poloidal coherence at r = 6cm for two values of q.

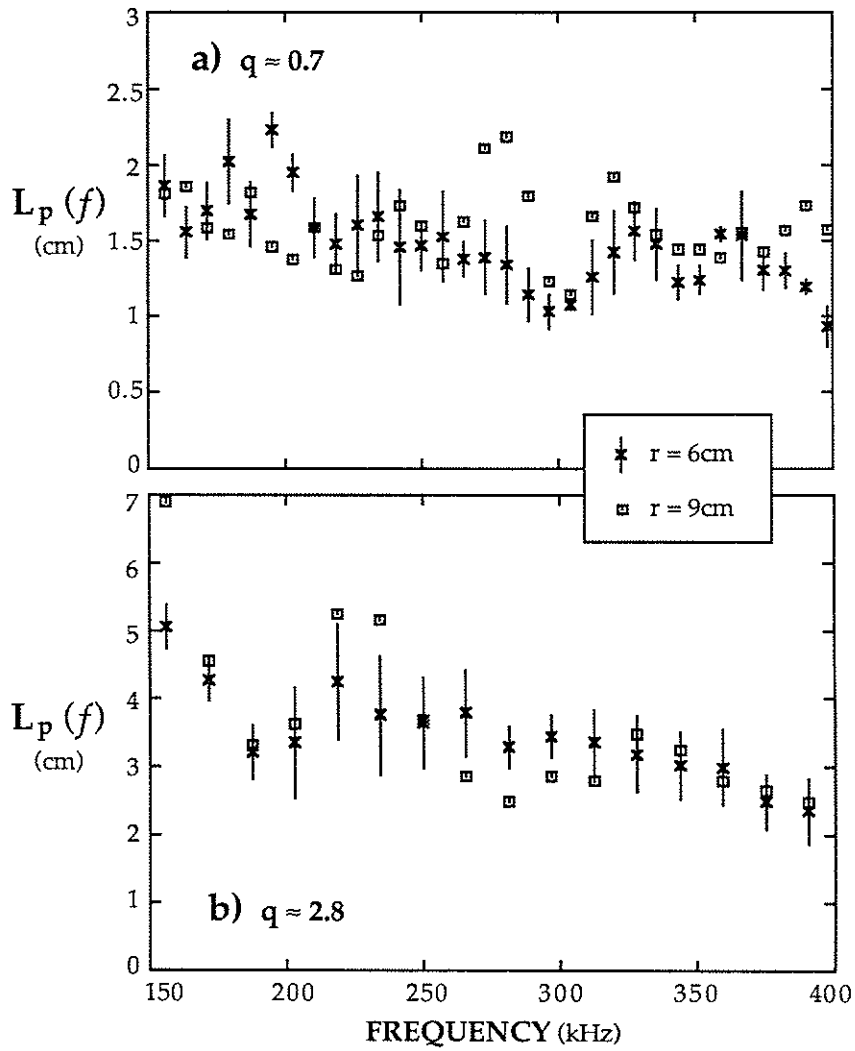

FIG. 4.32. The invariance of poloidal coherence length with radius for microturbulence at (a) q ≈ 0.7 and (b) q ≈ 2.8.

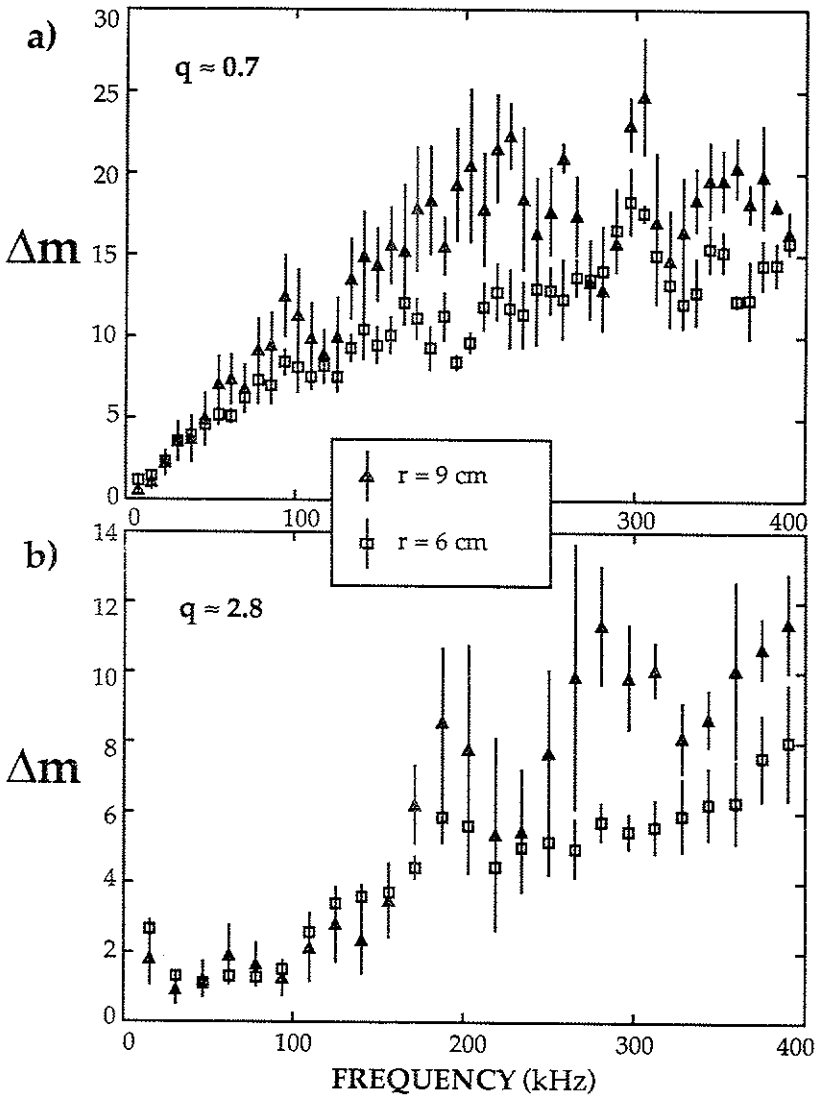

FIG. 4.33. The variation in Δm with minor radius resulting from the invariance of poloidal coherence lengths in Fig. 4.32.

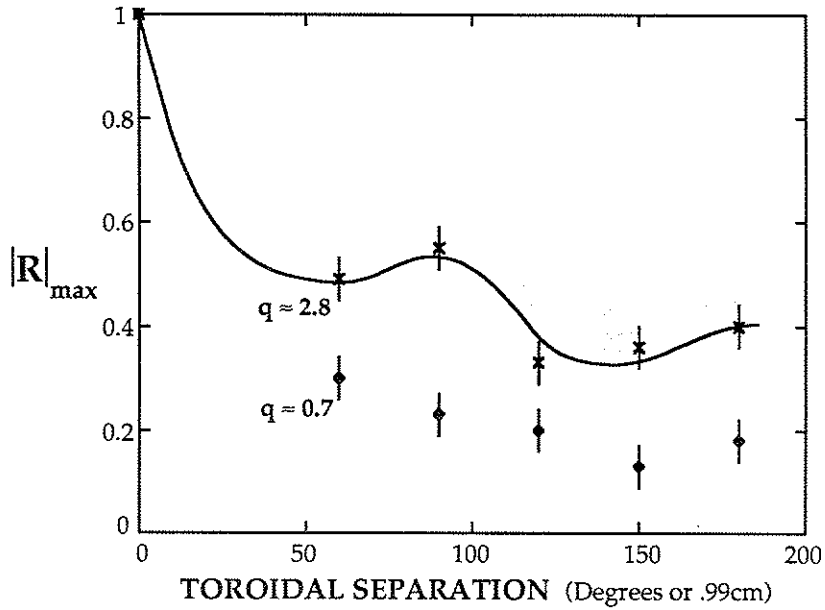

FIG. 4.34. Variation in correlation amplitude with toroidal separation at $r = 8$cm. Note the apparent oscillation in the $q \approx 2.8$ case.

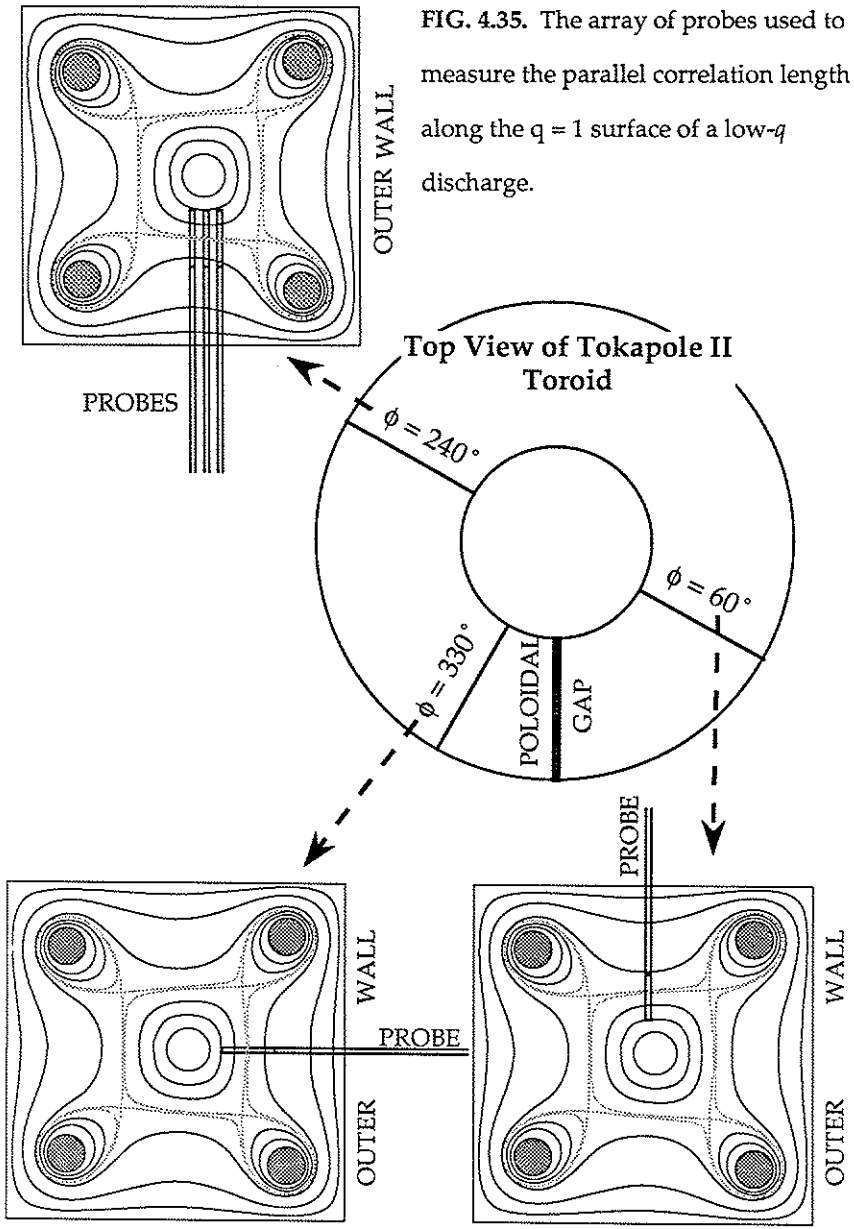

FIG. 4.35. The array of probes used to measure the parallel correlation length along the q = 1 surface of a low-*q* discharge.

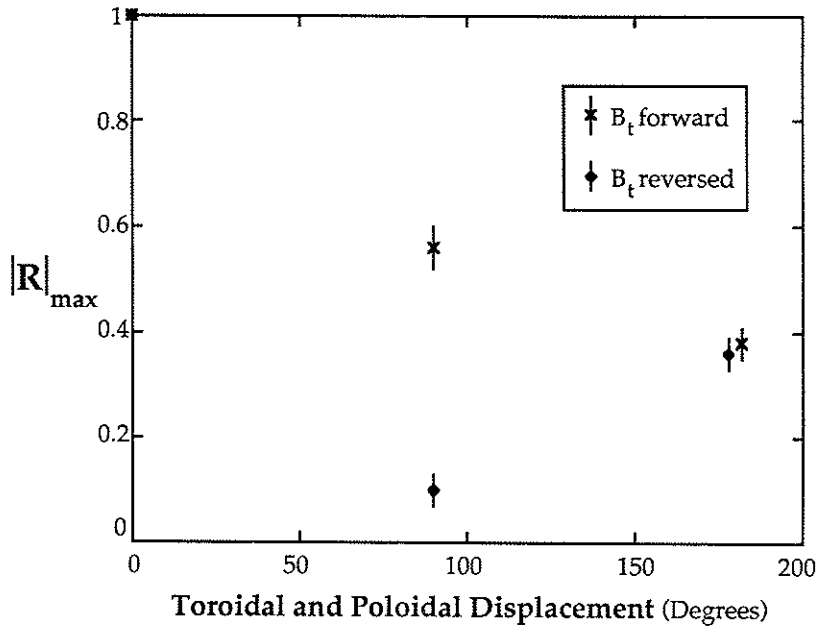

FIG. 4.36. Variation in total correlation amplitude with separation believed to be along a q = 1 flux surface in a q ≈ 0.7 discharge. The "X's" give the result with the probes placed along the lines of force. The diamonds give the result for reversed toroidal field, meaning that the 90° displacement is not along a line.

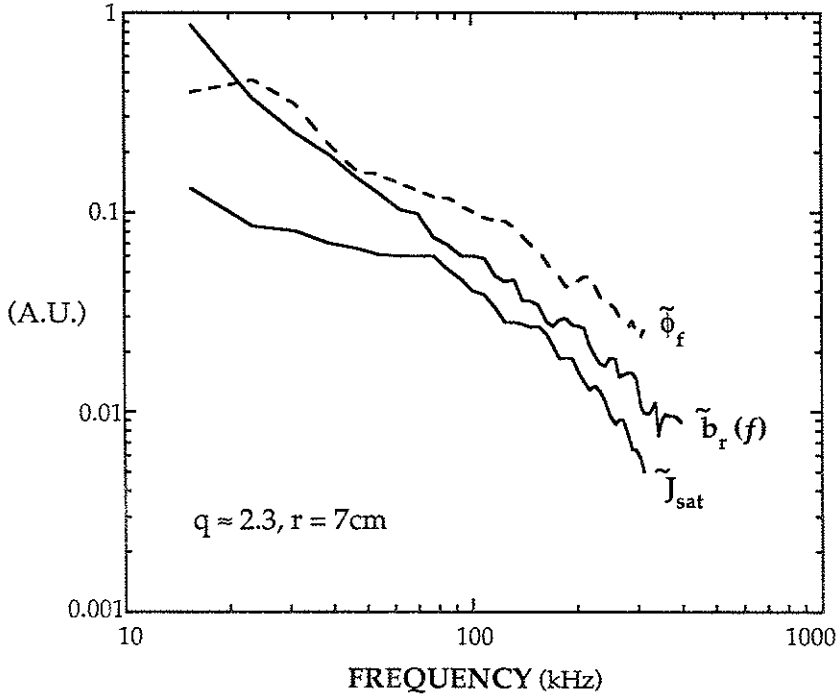

FIG. 4.37. Comparison of the frequency structure of turbulence in the local ion saturation current (density), the floating potential, and radial magnetic field at r = 7cm in a discharge of $q_a \approx 2.3$.

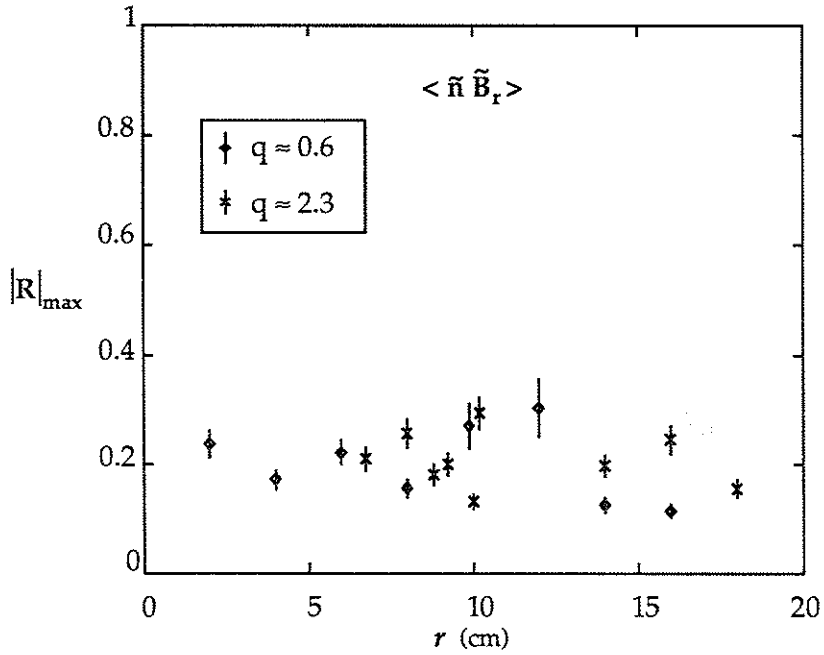

FIG. 4.38. Full cross-correlation between magnetic and ion saturation current (density) fluctuations displaced 3mm radially, at various radii, for two values of q_a.

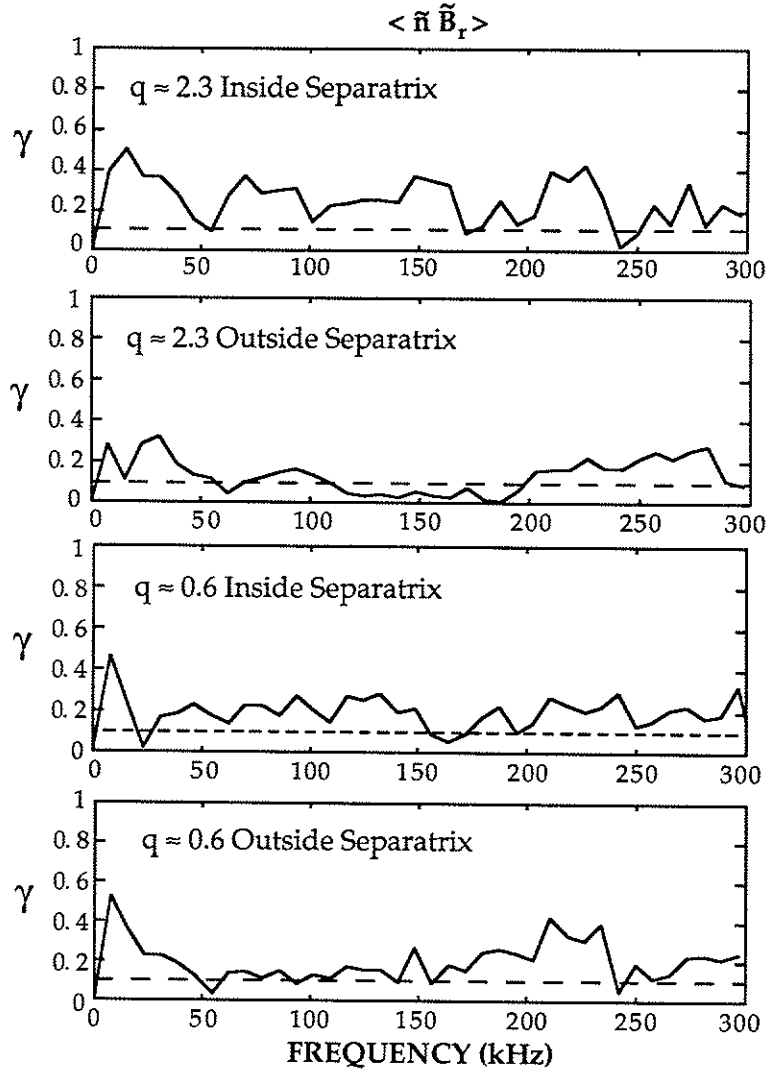

FIG. 4.39. Coherence between ion saturation current (density) fluctuations and radial magnetic fluctuations at points inside (r = 7cm) and outside (r = 14cm) the separatrix, for two values of q_a.

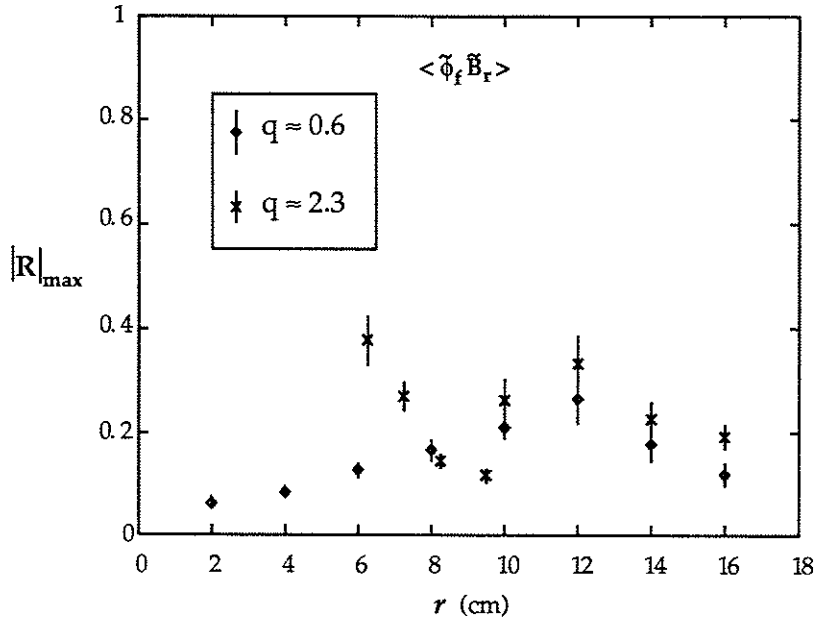

FIG. 4.40. Full cross-correlation amplitude for floating potential and magnetic fluctuations displaced 3mm radially.

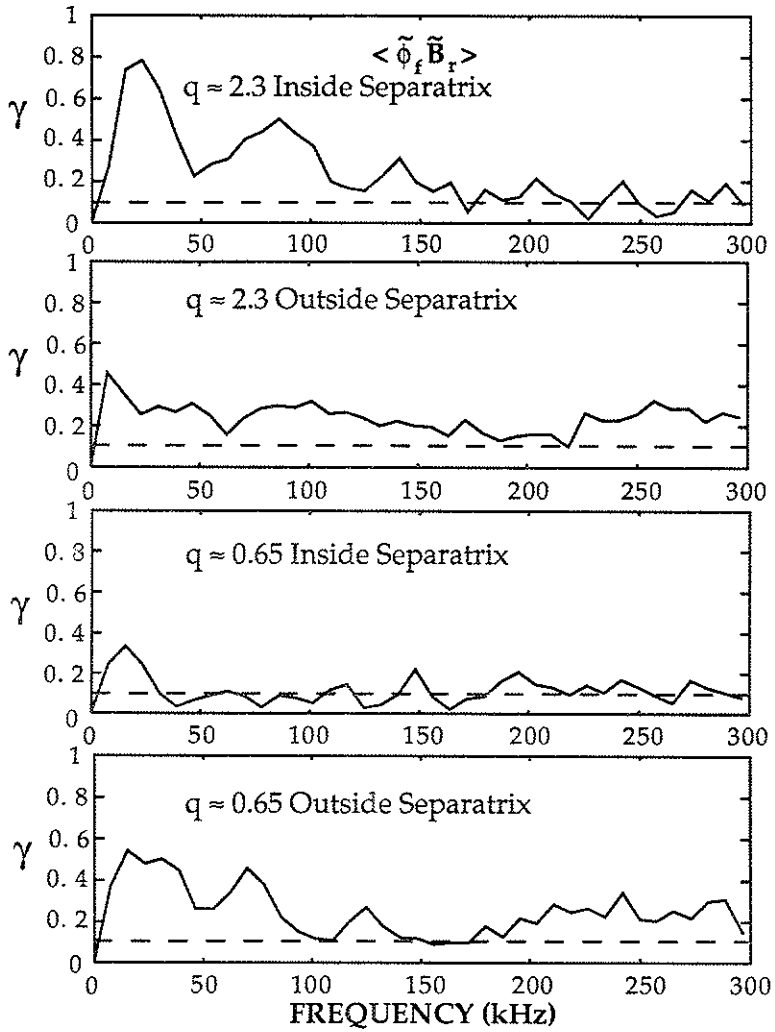

FIG. 4.41. Coherence between floating potential fluctuations and radial magnetic fluctuations at points inside ($r = 7$cm) and outside ($r = 14$cm) the separatrix, for two values of q_a. Floating point probe and magnetic sensor are displaced 3mm radially.

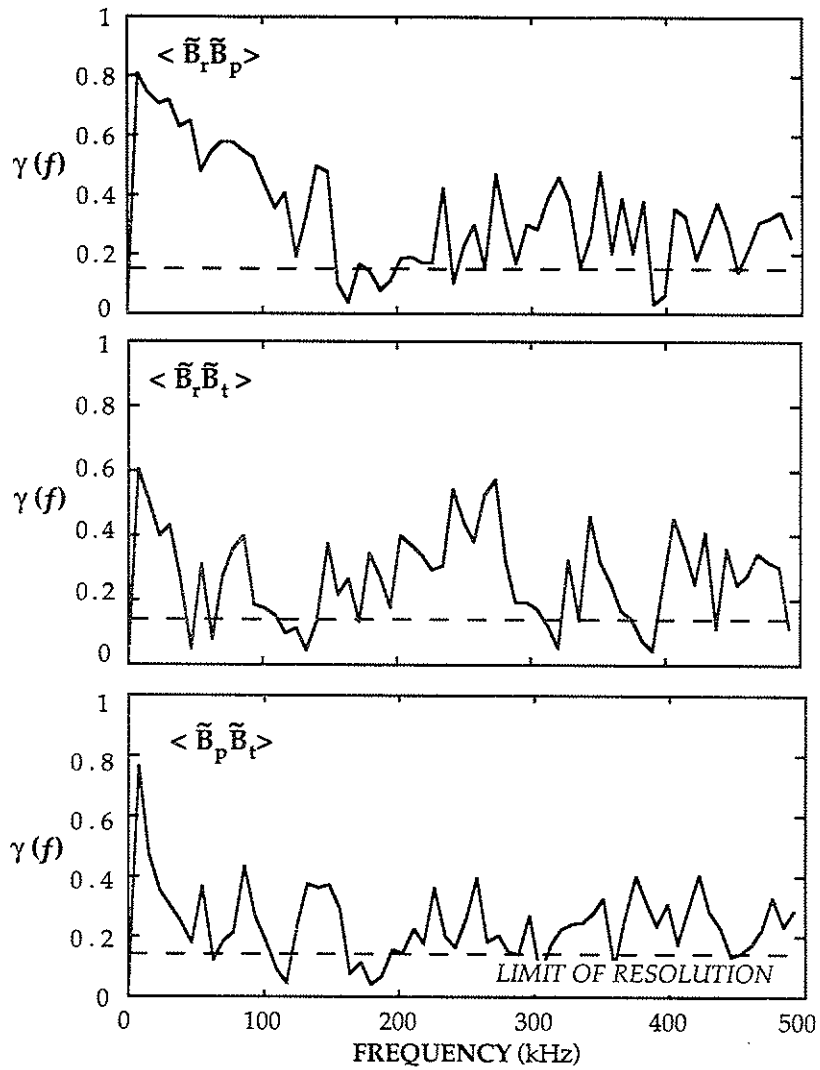

FIG. 4.42. Cross-coherence versus frequency for perpendicular magnetic sensors at the same location, with $r = 4.5$cm, and $q \approx 0.6$. (a) Radial × poloidal; (b) Radial × toroidal; (c) Poloidal × toroidal.

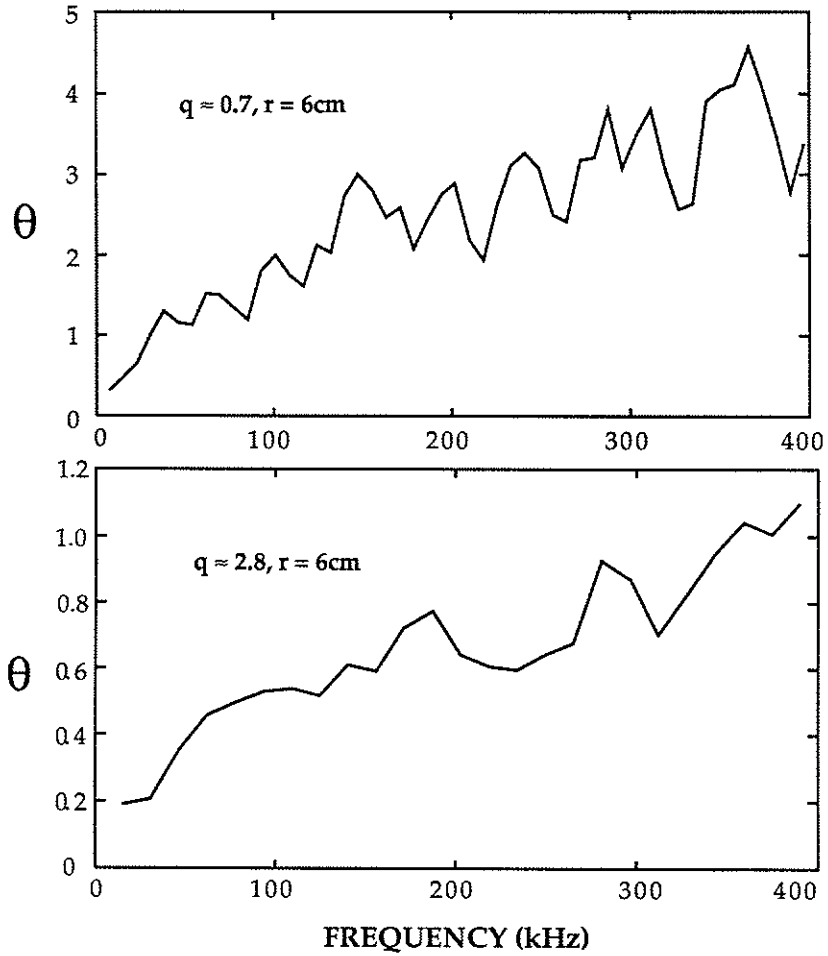

FIG. 4.43. Ensemble-averaged phase shift between two poloidally separated sensors for $q_a \approx 0.7$ and 2.8 showing a rather linear variation with frequency. The curves are fairly linear with frequency, suggesting a reasonably constant phase velocity for the microturbulence.

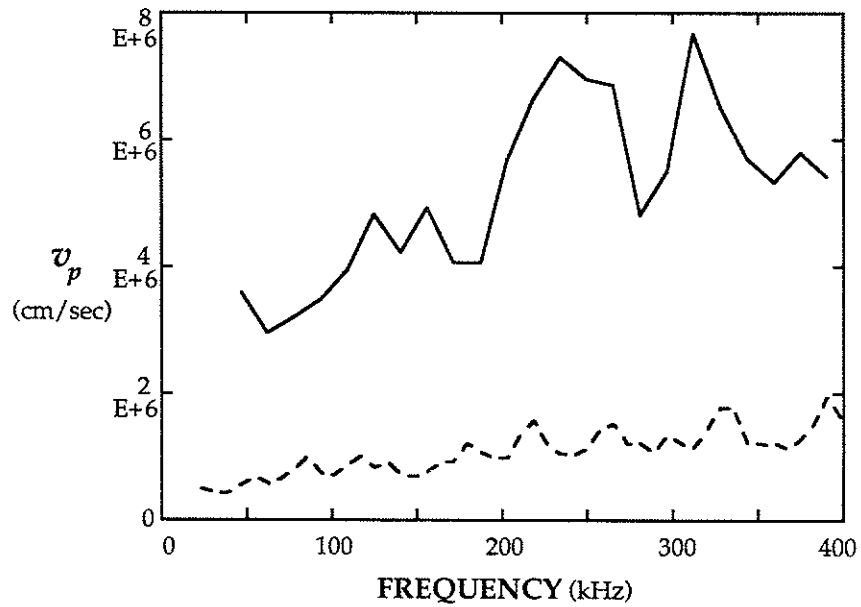

FIG. 4.44. Phase velocities as functions of frequency for high and low edge q, from relative phases of poloidally-separated coils located at $r \approx 6$cm. This is from the phase data plotted in Fig. 4.43.

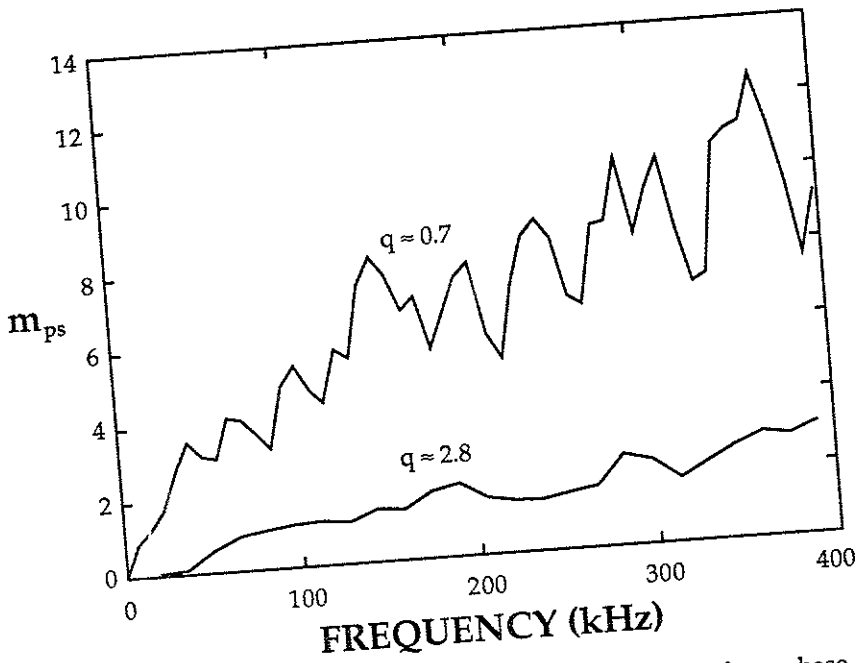

FIG. 4.45. Poloidal mode number estimates versus frequency from phase shifts in poloidally separated coils at $r = 6$cm, for two different values of edge q.

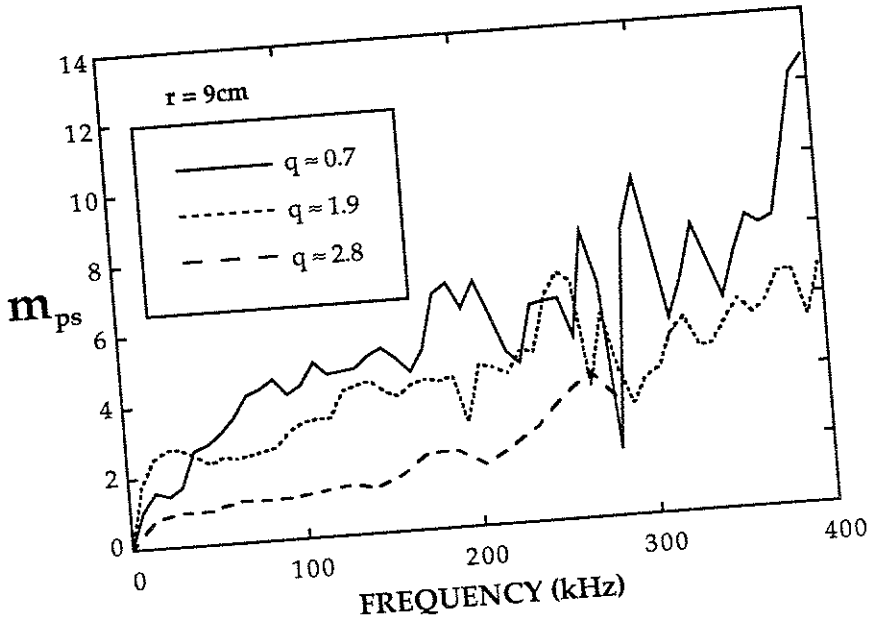

FIG. 4.46. Curves tracing poloidal mode numbers calculated from phase shifts of poloidally separated sensors at $r = 9$cm. Three values of edge q are represented, and in general the values of m_{ps} decrease with increasing q.

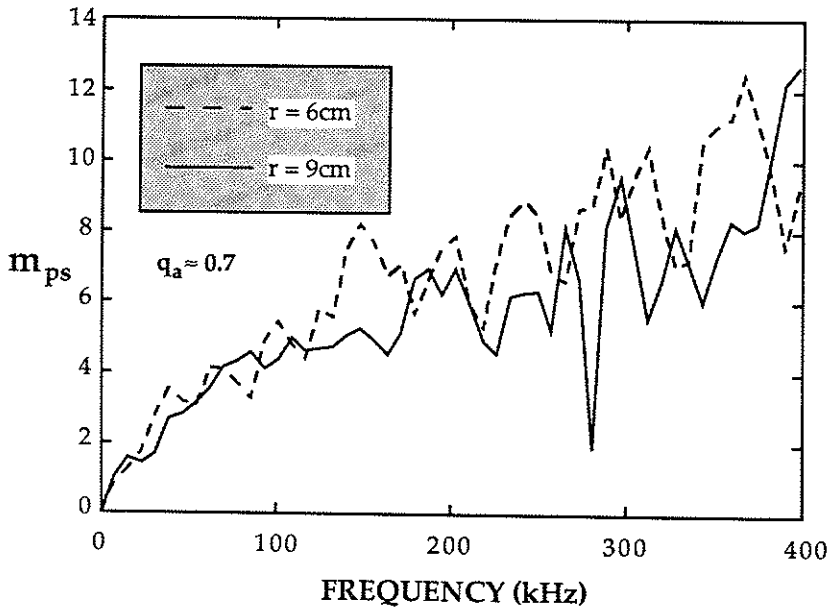

FIG. 4.47. Poloidal mode numbers determined from phase shift measurements at $r = 6$ and 9cm for $q_a \approx 0.7$. The values are quite similar for all frequencies, indicating that m is independent of minor radius.

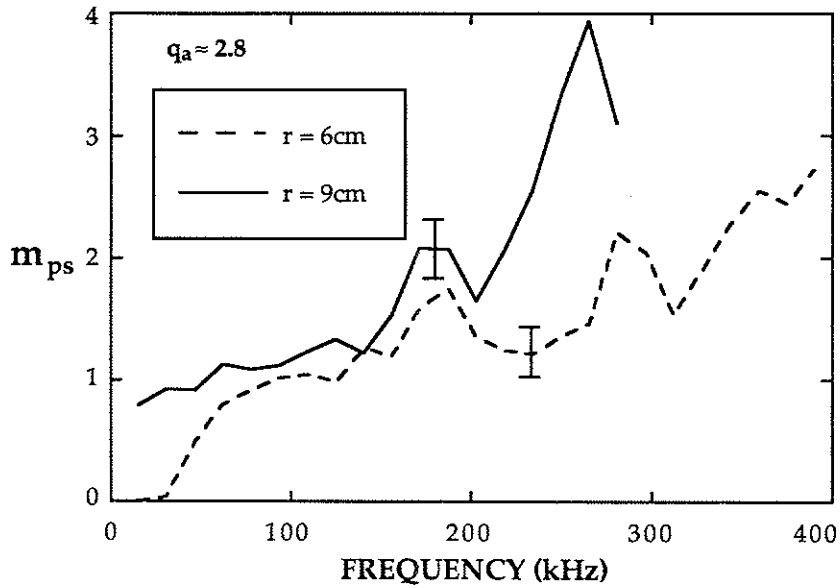

FIG. 4.48. Poloidal mode numbers from phase shifts at $r = 6$ and 9cm for $q_a \approx 2.8$. For most f, the values are not significantly different. The measured phase at $r = 9$cm becomes irregular for $f > 300$kHz, despite the presence of significant coherence.

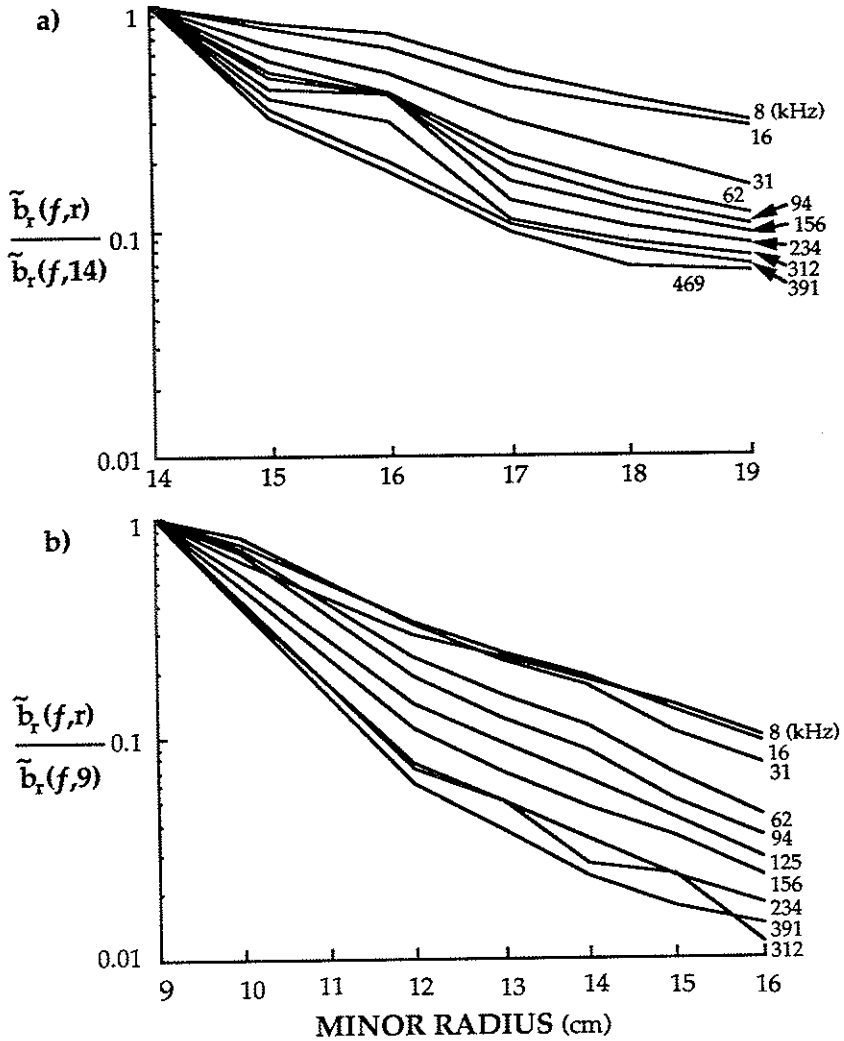

FIG. 4.49. Radial amplitude decay outside the bulk of the plasama for two values of edge q. The minor radius scales are different, because the profiles of low q are much broader.

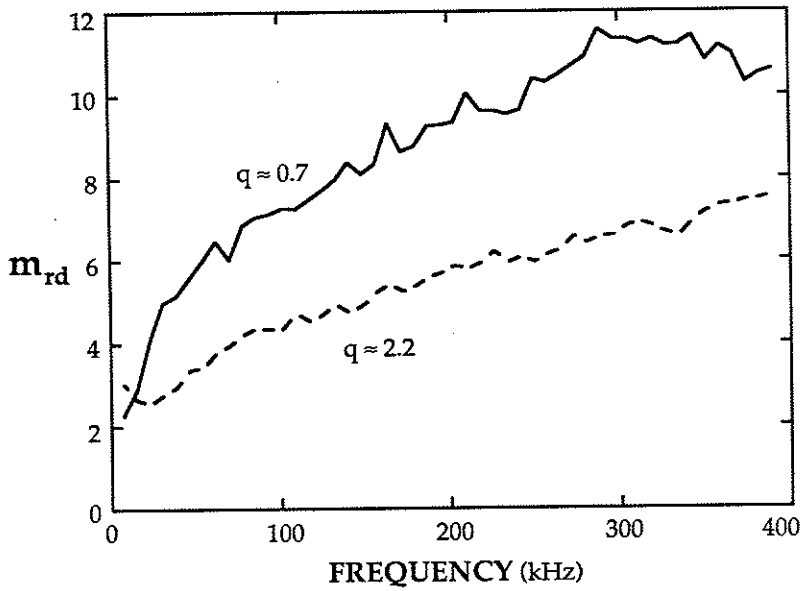

FIG. 4.50. Poloidal mode numbers as determined from radial amplitude decay for two values of edge q.

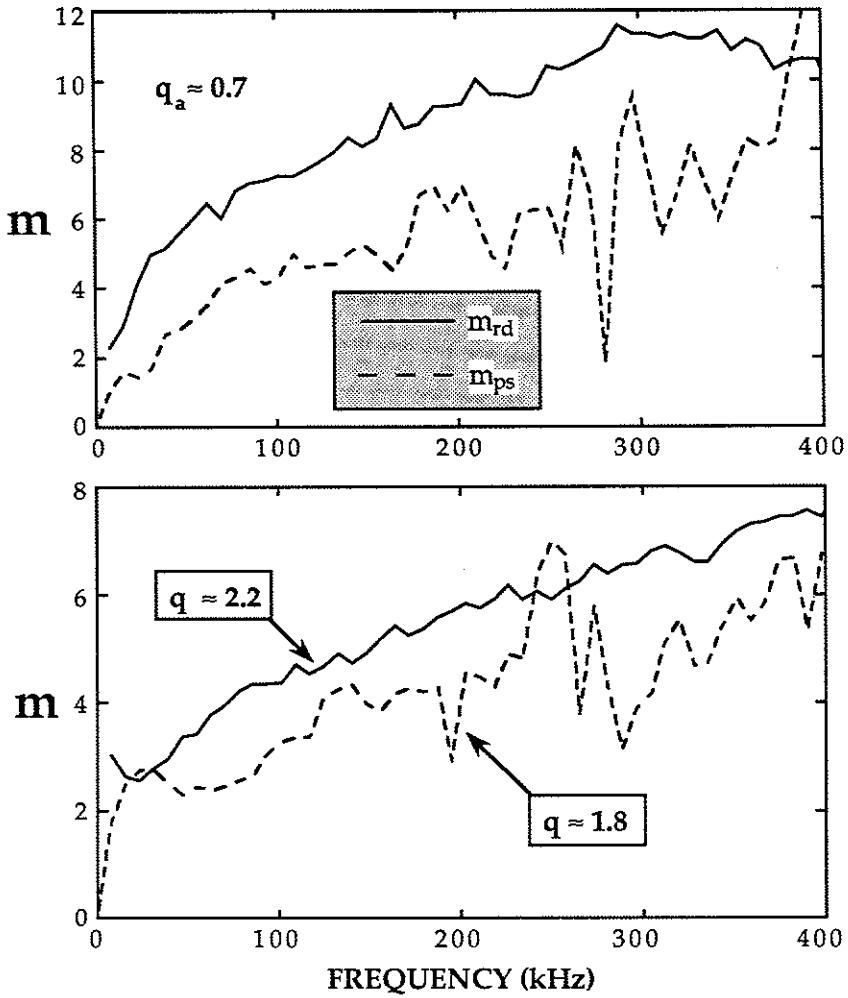

FIG. 4.51. Comparison of poloidal mode numbers vs frequency as determined from radial amplitude decay measurements with those from phase shifts presented earlier.

CHAPTER 5

Discussion and Conclusions

This final chapter is dedicated to a review of the findings of the low-frequency magnetic turbulence measurements on Tokapole II, and to initiate discussion of the possible meanings and implications of these measurements with regard to the underlying physical processes in tokamak plasma turbulence. Tokapole II is a unique device which allows these initial internal magnetic turbulence measurements to be made.

The theoretical and experimental study of turbulence is a fledgling field indeed, and many contributions, whether forthcoming or not, will be required to develop a complete picture. The findings of this particular work are mostly not startling, but do serve to bring some degree of clarity and light to the interior workings of tokamaks in general. It is to establish this point that Chapter 5 is included.

5.1. General discussion of results

Because of the large volume of data presented, it will be necessary to break down the discussion into sections paralleling those of Chapter 4, and only then to cross-correlate results and compile conclusions.

5.1.1. Amplitudes, profiles, and transport

Tokapole II has been operated with edge safety factors in the range $0.6 \leq q_a \leq 5.0$. As q_a is reduced over this range, the level of the turbulence increases uniformly by a factor of fifty, while the confinement steadily decreases by more than a factor of ten. Normalization of τ_E to render it dimensionless reveals little change in confinement with $\tilde{B}_r/B$ for $q_a \geq 4$, suggesting that some instability present at lower q_a is rendered ineffectual at higher q_a, at least for this machine. For $q_a \leq 3$, the normalized τ_E varies significantly with the turbulence level, suggesting some causal relation has intervened in this range. Further experimentation with varying turbulence levels is needed to establish the causal relationship.

With regard to amplitudes of the turbulence, Fig. 5.1 indicates the electron thermal diffusivity from the Rechester-Rosenbluth formula[1] for the levels of turbulence over the full frequency range and the microturbulent range (100-400 kHz), as well as the actual value needed to account for the global confinement time, all versus q_a. It is seen that the turbulence level is only large enough to give a comparable χ_e via this model at the lowest values of q_a when the full frequency range is considered. (A value of 150 cm is assigned to L_0 here, for all q_a. The electron temperature is taken to be constant at 100 eV) This may indicate that other effects are more directly responsible for energy loss in the central regions of this tokamak, but the variations in the magnetic

turbulence level may be a manifestation of these effects becoming important.

For all cases measured, the radial profiles of $\tilde{B}_r$ closely resemble the local J_{sat} equilibrium profiles. This implies that the local magnetic turbulence amplitude actually follows the density and temperature profiles, which are likely to be similar in this machine. Hence, the turbulence may not be driven by instabilities derived from the density or temperature gradients alone, as are some drift-wave models. Those models derived from ratios of local gradients, or weak dependences on gradients, such as resistivity-gradient-driven turbulence,[2] may be more likely to explain the turbulence amplitude profiles.

The turbulent spectra above 100 kHz exhibit a power-law decay with frequency for all q_a. For $q_a < 4$, the power law is always $f^{-1.4}$. For higher q_a, the power law is $f^{-2.3}$. The implication is that for $0.6 \leq q < 4$, the same physical process is driving the turbulence despite the factor of ~10 variation in $\tilde{B}_r/B$ over this range. Also, this process may be responsible for the decay in normalized τ_E discussed above.

5.1.2. Correlations, mode structure, and models

Radial coherence lengths were measured as a function of edge safety factor. Large values (≥10cm) are found below 100kHz, but above that frequency the results depend on minor radius and q_a. Inside the separatrix, $L_r(f>100\text{kHz}) \approx 2\text{cm}$ for $0.6 \leq q_a \leq 3.0$, and markedly less (≤1cm) for higher safety factors. This is another indication that the same turbulent process or processes are involved in the range of $q_a \leq 3$.

Outside the separatrix, coherence lengths are 5–10cm for f>100kHz in the range $0.6 \leq q_a < 2.8$, and smaller for higher safety factors. This is because the edge is more or less vacuum-like at the lower q_a, and the higher-q discharges have more edge activity such as runaway electrons to contribute to local fluctuations.

Poloidal coherence lengths of $\tilde{B}_r$ were measured in the interior for $q_a \approx 0.7$ and 2.8. The values found are similar to those found in other tokamaks. For f<150kHz the values are large (≥10cm). For higher frequencies the values were small, but also higher for high q than low q. The spread in poloidal mode numbers is thus higher in low q, so that a larger number of poloidal modes exist at the low q. Further, the microturbulent $L_p(f>150\text{kHz})$ is independent of radius for both q_a, indicating the turbulence may be linked to some intensive parameter such as gyroradius or resistive layer width. It turns out that $L_p \approx 1\text{-}2L_r$ for $f \geq 150$kHz, so that the microturbulent coherence is basically isotropic in the plane perpendicular to $\boldsymbol{B}$.

The parallel correlation length has been measured by placing an array of sensors along what is believed to be the q = 1 surface of a low-q discharge. A lower-limit value of 150 ± 10 cm was obtained for L_0. Improvement in the measurement of this value is under way by other experimenters.

Correlations of $\tilde{B}_r$ with electrostatic fluctuations within a radial separation of 3mm are non-zero, but small (~20-30%). This may be due to the relatively low β of this device. This carries the implication that specification of magnetic turbulence properties in no way determines those of electrostatic fluctuations. Hence these measurements must be made independently, and are being pursued now by other experimenters.

Attempts to measure the poloidal mode structure $m(f)$ reveal that m decreases as q_a is increased, and that it is also basically independent of minor radius (unlike Δm). This could be a result of interaction of the turbulence with macroscopic coherent oscillations, or a result of the turbulence being linked to micro-MHD instabilities or q-resonant modes.

5.2. Relevance to general tokamaks

5.2.1. Comparison of results to other experiments

The edge $\tilde{B}$ measurements of Zweben *et al*[3] revealed that the amplitude of the turbulence increased steadily as the probe was moved in toward the center from the wall. In all other cases, similar edge results were found. In the present experiment, the radial profile could be measured well into the plasma, particularly in the case of low q, and it was found to resemble that of J_{sat} in all cases. This result may indeed be found in any tokamak, and it is suggested that predictions of general tokamak turbulence profiles should be similar to the assumed or measured density and temperature profiles.

The microturbulent spectra have power laws much like any other tokamak in which they have been measured. The specific power law

may depend on the local or global geometry of the system, but this does not necessarily mean that different turbulent processes dominate $\tilde{B}$ in machines of differing shapes. The available data are still insufficient to establish which process or processes are in fact responsible for $\tilde{B}$ in any single machine, to say nothing of establishing the causes in tokamaks in general.

Radial and poloidal coherence lengths in Tokapole II are similar to those measured within the plasma in other devices.[1,4] In all machines reporting edge correlations measurements, correlation lengths are found to be in the 2–10cm range, regardless of machine parameters. In Tokapole II, the measurements have been extended to the interior, where values of L_r between .5 and 2.5cm have been herein reported. Furthermore, a very long correlation parallel to the field has been found, as has been reported in other machines.[5,6] Tokapole II also exhibits small but nonzero correlations between electrostatic and magnetic fluctuations in the frequency range 0-300kHz, which is not inconsistent with the results of Zweben on Macrotor.[7]

Therefore, despite the uniqueness and small size of the Tokapole II device, there is no evidence to indicate that the characteristics of magnetic turbulence measured in Tokapole II are in any way significantly different from those found in other machines to date. This implies that the results reported here may be considered fully relevant to the study of any other tokamak, until such time as it is demonstrated

that turbulent processes in the other machine are distinct from those in Tokapole II.

5.2.2. External versus internal results

Internal measurements of $\tilde{B}$ are at present impossible in high-temperature, high-density tokamaks such as TFTR, JET, or TEXT. This warrants some discussion of the Tokapole II results to determine which, if any, of the needed internal turbulence parameters can be estimated from edge $\tilde{B}$ measurements.

Despite the result that the turbulent amplitude resembles the I_{sat} profiles, it is unlikely that non-intrusive measurement of density and temperature profiles is a reliable way to determine the interior $\tilde{B}_r$. This must be done by direct internal measurement; it cannot be extrapolated from edge measurements.

Internal radial, poloidal, and parallel correlations of $\tilde{B}$ measurements cannot be extrapolated from the edge, either. Nor can they be inferred from internal electrostatic turbulence measurements. Nevertheless, the activity at the outer plasma surface may be observed from the vacuum region outside it. For example, if radial correlations in the edge are strong, poloidal (and, for that matter, toroidal) mode numbers at the outer surface of the plasma can be measured from the edge using phase shift measurements from sensors spaced within a coherence length of one another. Also, if the toroidal mode numbers are small, radial amplitude decay measurements may give a reasonable estimate of m and its variation with frequency, again at the plasma

surface. Further, Δm and Δn can be determined at the plasma surface from edge measurements, provided the radial coherence is large over the frequency range in question.

It is therefore possible to make some determinations of the activity at the boundary of the plasma from a distance. Truly internal information cannot be obtained for microturbulence from the limiter or divertor regions of a tokamak, mainly because of the short radial scale lengths which are the essence of microturbulence. Models dealing with internal $\tilde{B}$ must be tested against the extant locally-measured internal data, much of which is presented here.

5.3. Suggested future experiments

In view of the necessity of direct, internal measurements to determine many important relationships in magnetic turbulence, the work in Tokapole II in particular is perhaps well advised to be continued. Here are a few of the experiments which are immediately suggested by the results of this work, as well as some that were attempted, but remain incomplete at the writing of this thesis.

5.3.1. Other magnetic turbulence measurements

A more detailed scan of q_a for internal poloidal coherence measurements is necessary to establish the apparent trend in m and Δm with turbulence amplitude. This may hold the clue as to why turbulence decreases as q_a is increased.

5.3.2. The parallel correlation length

The parallel correlation length measurement included here did not include points for which the coherence was high for the entire 0-400kHz frequency range. More closely-spaced sensors need to be used to make a better measurement. This means in particular that sensors will not be separated by the "corners" in the flux surfaces caused by the divertor. The problem still exists that knowledge of the direction of the field lines in Tokapole II at the various flux surfaces remains imperfect, and it is not known that the direction of maximal correlation will necessarily correspond to the direction of the field lines. To improve the certainty of the measurement would require good current profile measurements, so that a field-line-tracing code could be used in locating the sensors for the measurement. An improved L_0 measurement is currently being pursued by LaPointe.[8]

5.3.3. Higher-order spectral analysis and wavenumber spectra

That the poloidal mode number m is independent of the minor radius suggests that there may be coupling between the microturbulence and some large-scale oscillations in the plasma interior. Higher-order spectral analysis should be used to determine the extent of coupling between the low-f large-scale modes measured here and the microturbulence. This should include an evaluation of the energy flow in this coupling, where present.

A better evaluation of space-time statistics of the turbulence than the standard spectral analysis presented here is the evaluation of

wavenumber spectra. This gives a power-weighted distribution of waves in the ensemble of data taken.[9] The problem is that the microturbulence will be largely insignificant if the high-power global low-frequency data are included. These could be eliminated through frequency-filtering, but this would eliminate all data in the immediate range of ω_{*e} (drift waves). Another way is to eliminate only the large-scale fluctuations through the use of adaptive filtering.[10] An attempt has already been made to do this with magnetic turbulence data from PRETEXT by Levinson.[11]

5.3.4. Confinement measurements

The absent detailed confinement measurements in Tokapole II are the key weakness of this work. The locations of surfaces where global confinement might be critically determined (and hence where magnetic turbulence might be most influential) are not known at all. As stated, this requires profile measurements for which this device was neither designed nor funded. From an experimental standpoint, to do turbulence measurements and establish causality with transport requires transport profile determination. From a programmatic standpoint, this will likely never be done in Tokapole II.

5.4. Conclusions

This work has established the following conclusions and suggestions as to the interpretation of the available results:

(1) $\tilde{B}_r$ inside the separatrix increases by a factor of fifty as the edge safety factor is reduced from 5.0 to 0.7, while confinement degrades by a factor of sixteen.

(2) If τ_E is normalized by the Rechester-Rosenbluth stochastic fields formula for collisionless electrons, the variation in turbulence level corresponds to little change in confinement for $q_a \geq 4$. For lower q, the normalized confinement varies considerably with magnetic turbulence amplitude, suggesting that some effect has "turned on", or at least become influential for $q_a < 4$.

(3) The local $\tilde{B}_r$ increases steadily as the estimated local β is increased. The increase in β is a natural consequence of the reduction in q_a.

(4) The low-frequency ($f < 100$kHz) portions of the turbulence spectra consist mainly of large-scale modes which may be MHD oscillations. For $100 \leq f \leq 400$kHz, fluctuations with .5-2.5cm radial scale lengths are present, and this is the "microturbulence" measured in this experiment.

(5) The low-f spectra vary inconsistently with q_a, as might be expected of MHD modes, since different safety factors might mean different macroscopic resonances in the plasma. At $f \geq 100$kHz, however, the spectra are featureless, decaying as power laws of frequency. The power law is $f^{-1.4}$ always for $0.6 \leq q_a \leq 3$, the range corresponding to the rapid change in normalized τ_E in (2). For higher q_a, the high frequency decay law becomes $f^{-2.3}$. This suggests that

transport mechanism is involved in generating the slower $f^{-1.4}$ power-law turbulence.

(6) For $0.6 \le q_a \le 3$, the radial coherence measurements within the separatrix are all similar, and $L_r(f>100\text{kHz}) \ge 1\text{cm}$. For $q_a \ge 4$, the internal coherence lengths at high frequencies become less than 1cm, slightly smaller overall than those for the range $0.6 \le q_a \le 3$. Apparently the increased transport versus magnetic turbulence related in (2) above also coincides with increased radial coherence lengths.

(7) In all cases measured, the radial profiles of $\tilde{B}_r$ resemble rather closely the equilibrium J_{sat} profiles, implying that they resemble temperature and density profiles in Tokapole II. This suggests that the turbulence does not result from instabilities derived from temperature or density gradients alone. Instabilities dependent on the ratios of or fractional powers of the gradients, such as resistivity-gradient-driven turbulence, may be more likely to predict this characteristic.

(8) Estimates of the poloidal mode structure at the plasma surface indicate that m(f) generally increases with frequency for all q_a, and that it decreases with increasing q_a (or B_t) for almost all f, in the range $0.6 \le q_a \le 2.8$, which includes all available measurements. In the two available q-cases with internal m-measurements, m is generally independent of minor radius.

(9) Poloidal coherence lengths (measured at $q_a \approx 0.7$ and 2.8) at $f \ge 150\text{kHz}$ are similar to those measured in other machines[3,4,6] and do not vary with minor radius, i.e., $\Delta m(f \ge 150\text{kHz})$ does vary with radius

or machine size. The lack of a minor radius dependence suggests that the microturbulence may be linked to some intensive parameter such as gyroradius or resistive layer width.

(10) The above nine points imply that the turbulence over the range $0.6 \le q_a \le 3$ might be due to a single underlying cause or set of instabilities, with the differences in the observed fluctuations due to geometric effects associated with the safety-factor scan; qualitative changes in the turbulence at $q_a \le 1$ (as might be expected from resistive interchange or kink modes) are *not* observed.

(11) Point (10) implies that the q_a-scan is perhaps a good way to control turbulence levels directly, without changing other important microturbulent instability factors. This could be the method most capable of observing the causal relation between magnetic turbulence and transport without good local transport measurements.

(12) The reason for the decrease in poloidal mode numbers with increasing q_a is not known; however, the smaller number of poloidal modes (smaller Δm) at higher q_a could account for the lower turbulence level and lower transport.

(13) The fluctuation level and confinement at $q_a \approx 0.6$ are similar to those measured for the reversed field pinch (RFP) experiments.[12] Thus, one might speculate that the commonality of the magnetic turbulence extends to the very low-q range of the RFP.

(14) The global confinement degrades significantly as q_a is lowered, and fluctuations increase. Precise comparison of measured

transport with that expected from stochastic magnetic fields requires improved measurement of transport in Tokapole II, as well as an improved measurement of the parallel correlation length of $\tilde{B}_r$, which is presently under way.

(15) The findings of this experiment may be considered relevant to the study of any tokamak with regard to its magnetic turbulence characteristics, at least until such time as models are developed sufficiently to show that these turbulence properties vary significantly from one machine to another.

REFERENCES

[1]A.B. Rechester and M.N. Rosenbluth, Phys. Rev. Lett. **40**, 38 (1978).

[2]B.A. Carreras, P.W. Gaffney, H.R. Hicks, and J.D. Callen, Phys. Fluids **25**, 1231 (1982); L. Garcia, P.H. Diamond, B.A. Carreras, and J.D. Callen, Phys. Fluids **28**, 2147 (1985).

[3]S.J. Zweben, C.R. Menyuk, and R.J. Taylor, Phys. Rev. Lett. **42**, 1270 (1979); Errata ibid., p. 1720.

[4]M.A. Hedemann, Ph.D. thesis, *Measurements of Magnetic Field Fluctuations in the Caltech Research Tokamak*, UCLA, (1982).

[5]F. Ryter, A. Pochelon, and F. Hofmann, in *Proceedings of the Fourteenth European Conference on Controlled Fusion and Plasma Physics, Madrid, 1987*, edited by S. Methfessel (EPS, Petit-Lancy, 1987).

[6]K.W. Gentle, Y.J. Kim, Ch.P. Ritz, and T.L. Rhodes, in *Proceedings of the Fourteenth European Conference on Controlled Fusion and Plasma Physics, Madrid, 1987*, edited by S. Methfessel (EPS, Petit-Lancy, 1987).

[7]S.J. Zweben and R.J. Taylor, Nucl. Fusion **21**, 193 (1981).

[8]M.A. Lapointe, R.N. Dexter, E.J. Haines, and S.C. Prager, Bull. Am. Phys. Soc. **33**, 2020 (1988).

[9]J.M. Beall, Y.C. Kim, and E.J. Powers, J. Appl. Phys. **53**, 3933 (1982).

[10]B. Widrow, J.R. Glover,Jr., J.M. McCool, J. Kaunitz, C.S. Williams, R.H. Hearn, J.R. Zeidler, E. Dong, Jr., and R.C. Goodlin, Proc. IEEE, **63**, 1692 (1975).

[11]S.J. Levinson, B. Rogers, E.J. Powers, R.D. Bengtson, Bull. Am. Phys. **30**, 1441 (1985).

[12]I.H. Hutchinson, M. Malacarne, P. Noonan, and D. Brotherton-Ratcliffe, Nucl. Fusion **24**, 59 (1984).

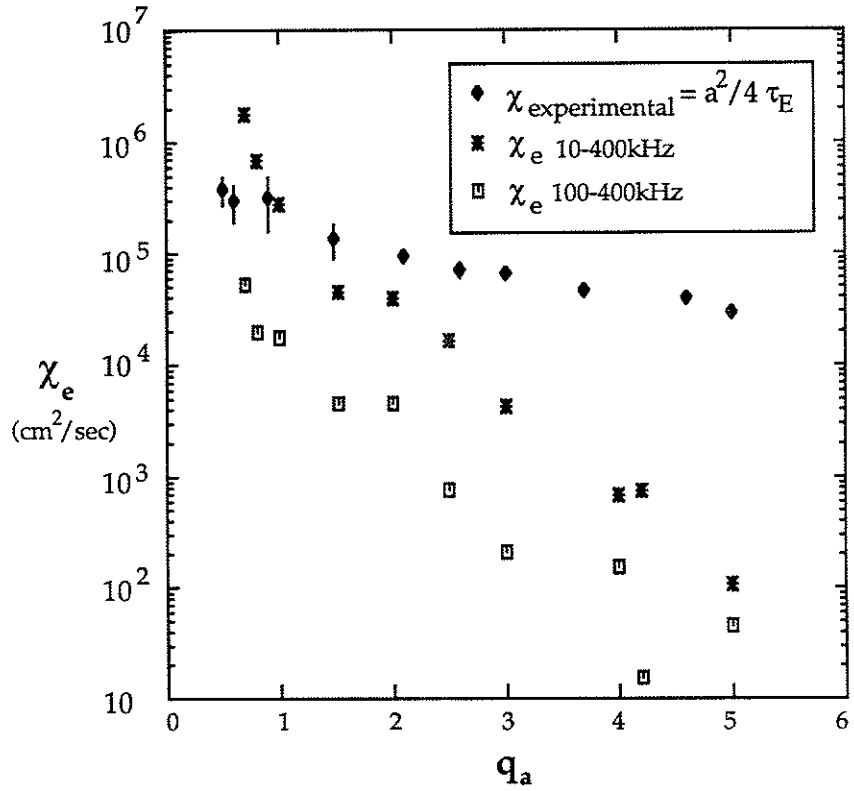

FIG. 5.1. A comparison of the thermal diffusivity required to explain experimental confinement, $\chi = a^2/4\tau$, and the electron thermal diffusivity calculated from the formula of Rechester and Rosenbluth, $\chi_e = v_{th} L_0 (\tilde{B}_r/B)^2$. The magnetic turbulence levels are taken from $r = 8$cm.